Stability of Electrode-Electrolyte Interfaces during Charging in Lithium Batteries

Thesis by

Panagiotis Philippos Natsiavas

In Partial Fulfillment of the Requirements

for the Degree of

Doctor of Philosophy

California Institute of Technology

Pasadena, California

2016

(Defended October 21, 2015)

To my Mom Anatoli,

it is her to whom I owe simply everything.

Acknowledgements

I would like to take this opportunity to sincerely thank my advisor, Professor Michael Ortiz, for his guidance and encouragement during my studies here at Caltech. His continual tutelage and support helped me deepen my academic skills and shaped my approach to challenges that are both professional and personal. He has been a true mentor and I greatly appreciate it.

My deep appreciation goes to the members of my thesis committee: Professor Guruswami Ravichandran, Professor Dennis Kochmann, and Professor Kerstin Weinberg (University of Siegen). Professor Ravichandran's support and friendship since my first time here at the institute is especially acknowledged. Moreover, I thank Professor Dennis Kochmann for his guidance and for sharing with me his optimistic way of thinking, and also Professor Kerstin Weinberg for her valuable help, especially with the computational issues of this work. Finally, I thank Professors Ares and Phoebus Rosakis, whose friendship I shared at Caltech.

The support of Robert Bosch GmbH through the BERN (Palo Alto) and PIRE (Stuttgart) program is gratefully acknowledged.

The financial support, education, and help provided by the Caltech community throughout my graduate studies are much appreciated. I would especially like to

acknowledge Lydia Suarez and Marta Kahl for the technical support and for settling administrative things for me. In addition, I am thankful to Dr. Rosato Daniele, Dr. Ulrich Sauter, and Dr. Thomas Eckl for the support and hospitality they provided during my summer internship at Robert Bosch GmbH, Applied Research (CR/ARM1), in Stuttgart, Germany. I would like also to thank the research group of Professor William A. Goddard, III and especially Dr. Boris Merinov for the fruitful conversations during my first years. Also the support and help from Dr. Boris Kozinsky is greatly appreciated.

Lastly, but not least, I must express my gratitude to my family who has always been on my side and especially to my dad, Sotirios, for showing me the way to go.

Abstract

In this thesis we study the growth of a Li electrode-electrolyte interface in the presence of an elastic prestress. In particular, we focus our interest on Li-air batteries with a solid electrolyte, LIPON, which is a new type of secondary or rechargeable battery. Theoretical studies and experimental evidence show that during the process of charging the battery the replated lithium adds unevenly to the electrode surface. This phenomenon eventually leads to dendrite formation as the battery is charged and discharged numerous times. In order to suppress or alleviate this deleterious effect of dendrite growth, we put forth a study based on a linear stability analysis. Taking into account all the mechanisms of mass transport and interfacial kinetics, we model the evolution of the interface. We find that, in the absence of stress, the stability of a planar interface depends on interfacial diffusion properties and interfacial energy. Specifically, if Herring-Mullins capillarity-driven interfacial diffusion is accounted for, interfaces are unstable against all perturbations of wavenumber larger than a critical value. We find that the effect of an elastic prestress is always to stabilize planar interfacial growth by increasing the critical wavenumber for instability. A parametric study results in quantifying the extent of the prestress stabilization in a manner that can potentially be used in the design of Li-air batteries. Moreover, employing

the theory of finite differences we numerically solve the equation that describes the evolution of the surface profile and present visualization results of the surface evolution by time. Lastly, numerical simulations performed in a commercial finite element software validate the theoretical formulation of the interfacial elastic energy change with respect to the planar interface.

Contents

List of Figures

List of Tables

Chapter 1

Introduction

1.1 General Overview

1.1.1 Battery: Description, Operation, and Types

A battery is an electrical device that converts chemical energy into electrical energy. As in all electrochemical systems, a battery consists of two electrodes separated by an electrolyte. An external, electronic conductor wire connects the two electrodes and is used as a pathway for electrons to flow and create the electric current. Batteries are essential parts of mechanical structures because, when connected to an external circuit, the chemical reactions that take place on the electrolyte-electrode interface produce energy that is delivered to the structure in order to perform mechanical work. Due to their high gravimetric energy (energy per unit mass), batteries have received extensive interest in the recent past decades. This fact makes their study and development important in order to fulfill the needs of a demanding society.

Some objects found by archaeologists are speculated to have been used in the early 6^{th} century for production of electric energy; one such object is known as the

"Baghdad Battery". However, it was not until the year 1800 that the first electrochemical battery was built. It was the Italian physicist and chemist Alessandro Volta who invented the "Voltaic pile", a stack consisting of layers of zinc and copper separated by paper soaked in salt water. Volta proved that electricity could be generated chemically, and his invention triggered other scientists' interest in the development of the field of electrochemisty. In 1836, J.F. Daniel invented the first trustworthy, in terms of constant voltage and sufficient electric current, battery system, which was named after himself and called the "Daniel cell". His invention has been widely used in the industry, especially in the electrical telegraph network of that age. Since then, battery cells have been thoroughly developed but they still remain a source of great interest today.

The operation of the battery is based on the flow of electrons and ions, which are products of the chemical reactions that take place in the battery [75]. As mentioned before, a typical battery consists of a positive terminal, or cathode, a negative terminal, or anode, and an electrolyte. More specifically, the two electrodes are electronic conductors in which the mobile species are electrons and are usually made of metal. The electrolyte, which separates the two electrodes, is an ionic conductor -electronic insulator-, in which ions are the mobile species, and is formed when salt is placed into a solvent, such as water. The electrodes' ability to conduct the flow of electrons is measured by the electrical conductivity in $S(Siemens)/cm$ and is of order of 10^2 to 10^4 $[S/cm]$, while ionic conductivity measures the ionic flow in the electrolyte and is of order of 10^{-4} to 10^{-1} $[S/cm]$.

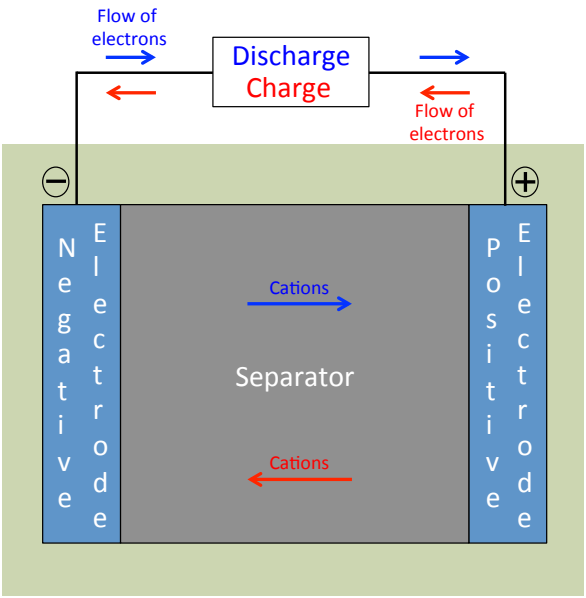

Figure 1.1: Battery operation, flow of electrons, and cations during the process of discharge (blue vectors) and charge (red vectors).

In a discharging battery the anode is the negative terminal. Electrons are moving outward through the electrical circuit to the positive terminal, the cathode, as shown in Fig. 1.1. In contrast, cations are moving through the electrolyte from the negative electrode to the positive one. In a recharging battery things are reversed: the anode is the positive terminal, it receives current from an external generator, and the electrode, which was the anode during battery discharge, becomes the cathode. Likewise, cations are now moving from the positive electrode to the negative one. In order to avoid confusion, the electrode on the left in Fig. 1.1 is often referred to as the negative electrode and the one on the right as the positive electrode, since this description is correct in both charging and discharging cycles.

In electrochemisty, a reduction reaction occurs when the electrode receives elec-

trons while an oxidation reaction occurs when the electrode loses electrons. Thus, during discharge oxidation occurs in the anode and reduction in the cathode. This is the main difference between a chemical and an electrochemical reaction. Specifically, in a chemical reaction, reduction and oxidation happen in the same place, while in an electrochemical reaction, reduction takes place at one electrode and oxidation takes place at the other.

The electrical driving force across the two electrodes is known as the "Voltage" of the cell and is measured in $V(Volts)$. The voltage of a cell when disconnected from any circuit, when no external electric current flows between the terminals, is called "Open-circuit voltage" (OCV). In electric circuits the flow of the electrons that travel through the external wire is called the electric current and is measured in $A(Ampere)$. One Ampere is defined as the current that flows with an electric charge of one Coulomb per second $[1A = C(Coulomb)/sec]$.

Batteries play an important role in the worldwide market and have found numerous applications in electronic appliances, energy storage systems, and transportation. More specifically, batteries can be found in power tools and portable electronic devices, e.g., laptops, cell phones, and cameras. In addition, military and aerospace industry use batteries in satellites, robots, communication devices, and air-structures. However, the most appealing application of batteries is for transportation. Electric vehicles that operate solely with an electric engine are already on the market and, as soon as researchers manage to provide adequate driving range in combination with reduced cost, the consumer demand is expected to rise significantly.

Batteries are classified into two main groups, see Fig. 1.2: primary, or non-rechargeable, batteries and secondary, or rechargeable, batteries. Primary cells, such as alkaline batteries, are used only once since the electrode is irreversibly changed during discharge and cannot be restored. Secondary cells can be discharged and recharged multiple times since all the chemical reactions can be approximately reversed and the original composition of electrodes can be restored almost completely. Common examples of secondary cells are lithium-ion batteries and most recently lithium-air batteries. The last type is going to be of interest in this work.

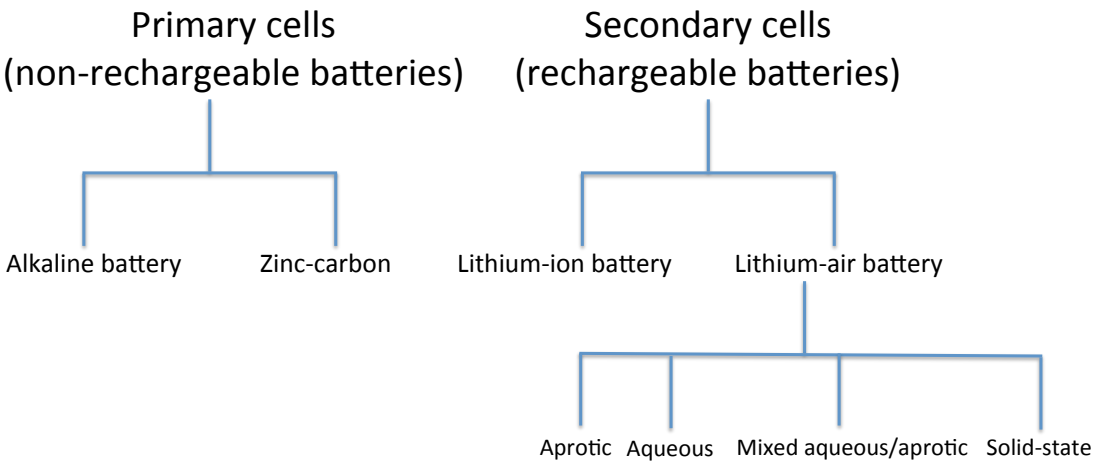

Figure 1.2: Types of batteries.

1.1.2 Li-Air Battery: Description, Limitations, and Promises

Metal-air batteries [15, 43, 88] are promising candidates for next generation power sources due to their low cost, long shelf life, environmental friendliness, and high theoretical gravimetric and volumetric energy density, c.f., Table 1.1. Furthermore, materials used in metal-air batteries are inexpensive, abundant, and environmentally

benign. Metal-air batteries are unique because unlike other types of batteries, they do not store one of the electroactive materials (oxygen). As a result, they can store the same, or even a greater, amount of energy when compared with other types of batteries, but they weigh much less. From all the metal-air batteries, see Table 1.1, the most promising category is the Li-air battery technology due to its having the highest theoretical gravimetric energy density and one of the highest open-circuit voltage.

Metal-Air Battery	**Calculated Open Circuit Voltage [V]**	**Theoretical Gravimetric Energy [Wh/kg] (including O_2)**
Li-O_2	2.91	5200
Al-O_2	2.73	4300
Na-O_2	3.2	2174
Ca-O_2	3.12	2990
Mg-O_2	2.93	2789
Zn-O_2	1.65	1090
Fe-O_2	1.28	750

Table 1.1: Open circuit voltage and theoretical gravimetric energy for various types of metal-air betteries [3].

A typical Li-air battery consists of a lithium metal anode and a carbon porous cathode with metal catalysts. The type of electrolyte that is used in between the electrodes can vary and thus the battery can be categorized into four main types [63]:

- Aprotic
- Aqueous
- Hybrid aqueous/aprotic
- Solid-state

In this work, we plan to focus only on one type of metal-air batteries, namely solid-state Li-air (oxygen) batteries. An up-to-date, state-of-the-art, critical review of Li battery technology may be found in the article of Christensen et al. 2011 [21] and in [42, 52, 56, 57, 65, 77]. Note here that while in the literature, as well as in this work, the batteries are widely referred to as Li-air batteries, the actual work has been on Li-oxygen (Li/O_2) batteries, since the air is composed of other elements as well, e.g., NO_2 or CO_2, that can have an undesired electrochemical interference with Li. A typical non-aqueous Li/O_2 battery is composed of a Li-metal foil (negative electrode), a thin solid Li-ion conducting electrolyte membrane, and a high surface area positive carbon electrode that is loaded with a catalyst (for example, Mn, Ni, Co) for the Li/O_2 reduction reaction at the positive electrode. The cell is exposed to the atmosphere at the carbon positive electrode, but is otherwise enclosed in a metallized case that is isolated from the environment. Oxygen from the environment is adsorbed onto the carbon electrode and reduced in the presence of Li during battery discharge. Non-aqueous Li-air batteries are controlled by the following overall reaction: $2Li^+ + O_2 + 2e^- \rightarrow Li_2O_2$. This reaction corresponds to a calculated open circuit voltage of approximately 3 $[V]$. Based on the mass and density of Li_2O_2, Li-air batteries have maximum theoretical gravimetric and volumetric energy densities of approximately 5,200 $[Wh/kg]$ and 8,000 $[Wh/l]$, respectively.

Lithium compounds are widely used as an electrode material for rechargeable batteries, due to the high electropositivity and low weight of lithium metal. During battery operation, lithium at the negative electrode gives up electrons to become Li^+,

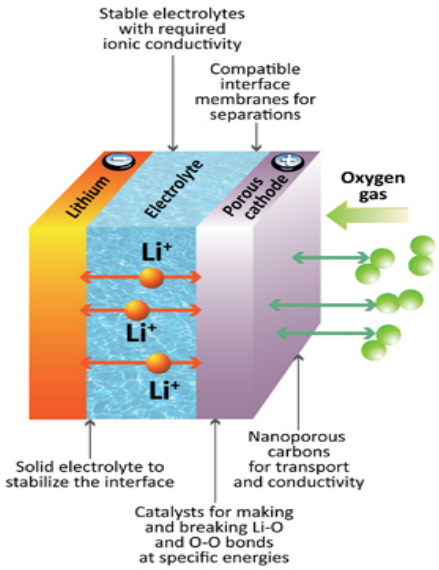

Figure 1.3: Li-air battery cell. Taken from [1].

which dissolves into the electrolyte, c.f., Fig. 1.3. This process is reversed during the recharge cycle, but the replated lithium adds unevenly to the electrode surface. As the battery is charged and discharged, dendrites have been observed to grow from one electrode to the other through the electrolyte [4, 8, 23, 71, 80, 107]. One of the mechanisms that trigger dendrite formation is thought to be the localized higher current density at the dendrite tip rather than its base [21]. Dendrite formation can cause a short-circuit (electrons find an easier path to move through the electrolyte and the voltage difference diminishes to zero) and make the battery useless. The size of dendrites ranges between hundreds to thousands of micrometers 200-3000 [μm] depending on the material system. In some cases, dendrite can be seen by naked eye, c.f., Fig. 1.4.

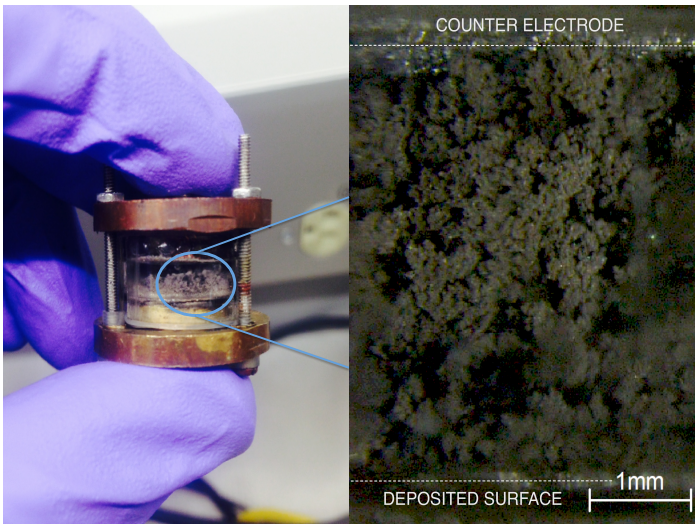

Figure 1.4: Dendrites in real battery cell. Taken from [9].

As of now, Li-air batteries are not for use outside of laboratory environments since they are still far from practical application due to challenges and limitations that need to be tackled. Apart from the morphology changes that the negative electrode undergoes, there are several other issues that need to be addressed. In particular, Li-air batteries are secondary type batteries and this requires that all chemical reactions that take place in them are reversible. However, experimental evidence [39,66,105,108] has shown that carbonate solvents react with the reactions products, e.g., CO_2 instead of O_2 is evolved during charging, and as a consequence the chemical composition of the system in not the same as it was originally. Other noncarbonate solvents have been under investigation, with the intent to increase the cyclability of the battery, given the fact that those solvents are stable against the electrode material. In addition, it appears that the capacity of the positive electrode can be severely reduced by three main mechanisms [5,6,89,90]: i) passivation of the electrode surface, ii) pore blocking, and iii) poor oxygen transportation. Enhancing the solubility of the discharging

products in combination with the use of gas channels to accelerate the kinetics of the oxygen could be a possible solution to this issue. Another challenge that needs to be addressed is the accommodation of significant volume changes that occur during the battery operation due to accumulation and release of mass (oxygen). Some solutions to this problem may be the application of pressure, which will help to obtain good contact between the different layers of the cell, and the use of flexible seals and electrolyte reservoirs [85]. Lastly, the challenge of providing pure oxygen to the cell still remains alluring. Air contains contaminants that are chemically active to react with the reaction products resulting in poor cyclability of tankless cells. On the other hand, the use of oxygen tanks inside the cell increases the weight and tarnishes one of the big advantages of Li-air batteries, which is the high specific energy. As a possible avenue, lightweight membranes [112, 113], in which only oxygen will be allowed to move in and out, could be used to protect the cell from other contaminants.

These critical issues make the commercialization of Li-air batteries daunting. The understanding of the fundamental aspects of these challenges would highly accelerate the process of searching and designing efficient and safe batteries. By the time these challenges are met, we can reap the benefits of this promising technology. Li-air batteries have the potential for having five times the specific energy of current lithium-ion batteries. This can be applied to the manufacturing of electric cars that have comparable driving range with current gas powered automobiles.

This work focuses only on the deleterious effect of dendrite growth. As mentioned before, the surface of the negative electrode tends to roughen and develop dendrites

with cycling. An effort to suppress or alleviate the dendrite propagation will be comprehensively discussed in the next chapters.

1.2 Previous Work

Dendritic lithium deposits on the battery electrode, after being subjected to multiple charges and recharges, were first observed in the work of Epelboin et al. 1980 [35] and later on by Yoshimatsu et al. 1988 [110]. Dolle et al. 2002 [28] reported dendritic growth of the interface on lithium polymer batteries and confirmed direct correlation between current density and dendrite formation. A statistical approach was taken by Deutscher and Fletcher [24–26] in order to describe dendrite initiation. Many other authors (Peled 1979 [83], Chazalviel 1990 [20], Sundstrom and Bark 1995 [99], Kanamura et al. 1996 [53], and Yamaki et al. 1998 [109]) studied the deposition mechanisms of metals in non-aqueous battery systems. In particular, Barton and Bockris 1962 [11] and Diggle et al. 1969 [27] put forth the first comprehensive model of dendrite growth. More recent studies can be found in the work of Ely and Garcia 2013 [34], Nishida et al. 2013 [76], and Monroe and Newman 2005 [72]. The latter ones conclude from their analysis that interfacial roughening is mechanically suppressed when the separator shear modulus is about twice that of lithium.

Improvement in lithium cycling efficiency by using additives in lithium metal is discussed in the work of Saito et al. 1997 [94], Eweka et al. 1997 [36], and Richarsdon and Chen 2007 [92]. Mikhaylik et al. 2010 [67] experimentally proved that application of pressure between the electrodes lowers the dendritic growth rate, which is an

approach that was first introduced by Hirai et al. 1994 [49]. A similar effect, i.e., application of elastic prestress that substantially reduces the morphology changes of the negative electrode, will be thoroughly discussed later in this thesis.

Previous work has also focused on characterizing Green's function within the context of the theory of linear elasticity. More specifically, Kelvin 1848 [54] first determined the Green's function for the problem of a point force applied to the full-space isotropic solid. Later, Boussinesq 1885 [17] derived a surface Green's function for a force normal to the free surface in isotropic solids. Finally, Mindlin 1936 [68] developed the half-space Green's function by superposing a complementary part of the solution to the Kelvin's full-space function. The Green's function corresponding to a point force applied to a bimaterial isotropic solid was solved by Dundurs and Hetenyi 1965 [33] and Fares and Li 1988 [37]. In addition, expressions for Green's function obtained for problems with anisotropic material properties can be found in the work of Barnett and Lothe 1975 [10], Mura 1987 [74], Ting [102, 103], and Tonon et al. 2001 [104]. Recently, the work of Pan [81, 82] provided us with the bimaterial Green's function and with relationships for the displacement and the stress fields in the transformed domain in anisotropic bimaterials.

1.3 Motivation - Objectives

The objective of the present study is to ascertain the effect of elastic prestress on the stability of interfacial growth in Li-air batteries. As noted before, dendrite growth is the most common failure mode for cells with Li metal anodes. Indeed, dendrites can

grow from the negative electrode surface through the electrolyte during the charging of the cell, resulting in an internal short-circuit. There is, therefore, a need for new designs that suppress or alleviate the deleterious effect of dendrite growth, assuring an improved reliability and a longer lifetime of the cell. A possible avenue to that effect is suggested by recent experimental work by Mikhaylik et al. [67], who report that the application of modest pressures in the range of 10 $[kg/cm^2]$ ($\sim$ 1 $[MPa]$) results in a substantial reduction in the roughening of the Li surface during cycling. However, a fundamental understanding of the effect of pressure and, more generally, prestressing on the stability of lithium-electrolyte interfaces appears to be lacking at present, which hampers the practical exploitation of prestress in battery design.

The principal aim of the present study is to ascertain conditions under which an electrode-electrolyte interface grows in a planar geometry and how such conditions are influenced by the elastic field of built-in prestress. Of particular interest is to ascertain how elastic prestress can be utilized in the design of Li-air batteries in order to eliminate dendrite formation and its pernicious effects in the lifetime of the cell. We base our analysis on a model of an interfacial growth that accounts for the kinetics of Li^+ transport through the solid electrolyte (e.g., LIPON) and within the interface, the kinetics of Li^+ adsorption by the anode, electrostatics, and the elastic field. In principle, these fields are coupled due to pressure-assisted diffusion, swelling of the intercalated electrolyte, and the Maxwell stress of the electrostatic field and contribute jointly to the chemical potential driving the motion of interface. In particular, the elastic field is sensitive to the shape of the interface, with the result

that its roughening may be self-sustaining and eventually lead to the formation of dendrites.

In this work, we account for this feedback effect through an asymptotic analysis of the elastic field of a nearly flat interface between two semi-infinite elastic bodies. Similar asymptotic analyses have been applied to nearly flat surfaces and interfaces between elastic bodies in the work of Srolovitz and Gao [40, 41, 96]. The present analysis results in explicit analytical expressions for the dependence of the critical unstable wavelength of the interfacial roughness, and growth rates thereof, on the state of prestress and on fundamental parameters such as surface diffusivities, surface energy, deposition kinetics, and elastic moduli.

1.4 Outline of the Thesis

This thesis is organized in six chapters. The layout is as follows:

In the present chapter, Chapter 1, the scientific context for this work, such as fundamental electrochemical aspects behind battery technology, is presented together with reviews of previous work. In addition, limitations and in particular advantages of Li-air batteries are critically evaluated. Lastly, we state clearly and comprehensively the objectives of this work.

In Chapter 2, we formulate the mathematical model and derive the governing equations of lithium transport through the solid electrolyte based on the bulk free-energy in it. The equation that describes the evolution of the surface is also derived using interfacial energy and kinetics. Furthermore, an asymptotic analysis on the

nearly flat electrode-electrolyte interface is performed, in order to find the dependence of the elastic energy on the surface profile. Finally, the surface Green's function is numerically obtained and expressions for the displacement and the stress fields on two semi-infinite linear-elastic solids, corresponding to the electrode-electrolyte domain, are derived and verified with similar work in the literature.

In Chapter 3, results are presented on the surface evolution with and without the effect of elastic prestress. In particular, a numerical code is built based on a suitable finite difference scheme that enables the visualization of the surface evolution by time.

In Chapter 4, we develop a theoretical framework using the properties of Fourier series to obtain a simplified version for the analytical expression of the elastic energy change derived in Chapter 2. This analytical expression is verified with numerical simulations performed in a finite element software, Abaqus FEA [2]. Results are presented and demonstrate the validity of the theory.

In Chapter 5, we perform a stability analysis on the surface evolution equation that was derived in Chapter 2, so as to examine the conditions that initiate dendrite formation. We find the dependence of the critical wavenumber of the interface on various parameters, such as surface diffusivities, interfacial energy, and the state of prestress. The effects of these parameters are then quantified for a specific, lithium-LIPON, material system by performing a parametric study, and a selected set of numerical results is presented.

Finally, in Chapter 6, the conclusions of this thesis are outlined together with possible directions for future work in the area.

Chapter 2

Formulation of the Model - Equation of Surface Evolution

In this chapter, we wish to formulate the governing equations of lithium transport in the electrolyte region. The stress field and the effective chemical potential of the electrolyte follow from the bulk free-energy density while conservation of mass, conservation of linear momentum, and charge balance provide us with the constitutive equations for ion flux and electric current. Finally, the governing equations are reduced for the case of solid electrolyte, i.e., LIPON.

In parallel, we seek a continuum equation of motion for the evolution of an electrode-electrolyte interface profile

$$x_3 = h(x_1, x_2, t) \tag{2.1}$$

during the early stages of charge. In this representation, we assume the interface to be shallow, thus representable as a graph, and we describe its profile by means of a height function h. In so doing, we choose Cartesian axes such that (x_1, x_2) span the interface and x_3 is transverse to it. The physical processes which are assumed to contribute

to the growth are i) surface diffusion, capillarity-driven by particle exchange between the anode and the electrolyte; ii) electrochemical deposition; and iii) energetic forces associated with the elastic and electrostatic fields of the anode/substrate. We proceed to formulate models for each of these processes in turn. Taking into account all these mechanisms, conservation of mass will provide us with the equation of evolution of the surface profile. An explicit expression for the dependence of the elastic energy on this surface profile is derived by recourse to an asymptotic analysis.

As part of the stability analysis, we also compute the surface Green's function, which allows the evaluation of the displacements that express the deviation from flatness. Lastly, we present results that verify the displacement and the stress fields of this electrode-electrolyte bimaterial domain.

2.1 Bulk Free-Energy and Lithium Transport through Electrolyte

For definiteness, we take lithium phosphorus oxynitride (Li_3PO_4N) [12,13,32,106,111], a solid-state electrolyte which is far safer against other conventional liquid flammable electrolytes that were being widely used in the past in lithium ion batteries. LIPON is considered to be one of the most promising electrolyte enhanced materials (demonstrated thousands of cycles) due to its stability when attached to lithium surfaces and sufficient ionic conductivity ($\sim 2 \cdot 10^{-6}$ $[S/cm]$ at room temperature). Amorphous LIPON films are being composed by sputtering LIPO (Li_3PO_4) in pure nitrogen (N_2)

and its mechanical characterization is reported in the work of [47] using nanoindentation techniques.

We then consider the following bulk free-energy per unit volume in the electrolyte:

$$\begin{aligned} A(\boldsymbol{\epsilon}, T, c, \varphi) = & \frac{1}{2} c_{ijkl}(\epsilon_{ij} - \epsilon^*_{ij} - \frac{\Omega c}{3}\delta_{ij})(\epsilon_{kl} - \epsilon^*_{kl} - \frac{\Omega c}{3}\delta_{kl}) \\ & + \frac{\varepsilon}{2}|\nabla\varphi|^2 + z_+ F\varphi\nu_+ c + z_- F\varphi\nu_- c + \varepsilon(\varphi_{,i}\,\varphi_{,j} - \frac{|\nabla\varphi|^2}{2}\delta_{ij})\epsilon_{ij} \\ & + \mu_0^E c + \nu RT\big(\log(f_\pm \frac{c}{c_0}) - 1\big)c, \end{aligned} \tag{2.2}$$

where c_{ijkl} are the elastic moduli, ϵ^*_{ij} is prescribed pre-strain, Ω is the partial molar volume of ion dissolved in the solid electrolyte $[m^3/mol]$, c is the salt concentration given by $c = \frac{1}{\nu}(c_+ + c_-)$, where $c_+ = \nu_+ c$ and $c_- = \nu_- c$ are the concentration of the positive/negative ions (in our case, negatively charged immobile vacancies) and $\nu_\pm (\nu = \nu_+ + \nu_-)$ are the numbers of cations/ions into which a mole of electrolyte dissociates, c_0 is a reference ion concentration $[mol/m^3]$, ε is the electric permittivity $[F/m, F = J/V^2 = C^2/J = Farad]$, φ is the local electrostatic potential $[V]$, $z_\pm$ is the charge number per ion (dimensionless), F is Faraday's constant $[F = 96487\ [C/mol], C = Coulomb]$, μ_0^E is the ideal chemical potential per mole of salt in the electrolyte $[J/mol]$, $R = 8.314462175\ [J/(molK)]$ is the ideal gas constant, T the absolute temperature $[K]$, and $f_\pm^\nu$ $(f_\pm^\nu = f_+^{\nu_+} f_-^{\nu_-})$ is the activity coefficient (dimensionless). The bulk free-energy density (2.2) accounts for the elastic field, including the effect of swelling due to an ion concentration and a pre-strain; the electrostatic field, including coupling to the charged lithium ions and the coupling between the electrostatic and the elastic fields; and the entropy of mixing of the intercalated lithium

ions. Note here that the bulk free-energy can be simplified, without any significant loss of accuracy, if the terms that are being multiplied by the electric permittivity ε of LIPON ($\varepsilon \sim 10^{-7}$ $[F/m]$) [62] are considered to be negligible compared to the rest.

In addition, the total concentration of the electrolyte is given by

$$c_T = \sum_{i=1}^{3} c_i, \tag{2.3}$$

where the sum is over all species i in solution. In the case of a binary salt in a single solvent, i takes values from 1 to 3 (or o, +, -), since the mixture consists of one solvent (o) and two ions (+, -).

The stress follows from the free-energy density (2.2) as

$$\sigma_{ij} = \frac{\partial A}{\partial \epsilon_{ij}} = c_{ijkl}(\epsilon_{kl} - \epsilon^*_{kl} - \frac{\Omega c}{3}\delta_{kl}) + \varepsilon(\varphi_{,i}\,\varphi_{,j} - \frac{|\nabla\varphi|^2}{2}\delta_{ij}). \tag{2.4}$$

This expression accounts for the swelling due to the intercalating lithium ions and the coupling between the elastic and the electrostatic field through the Maxwell stress.

The effective chemical potential $[J/mol]$ of the electrolyte follows as

$$\mu^E = \frac{\partial A}{\partial c} = \nu_+\mu_+ + \nu_-\mu_- = \mu_0^E + \nu RT\log(f_\pm \frac{c}{c_0}) - \Omega p, \tag{2.5}$$

where

$$\mu_0^E = \nu_+\mu_{0,+} + \nu_-\mu_{0,-} + RT\log\left((\nu_+)^{\nu_+}(\nu_-)^{\nu_-}\right) \tag{2.6}$$

is the ideal chemical potential,

$$p = \frac{1}{3}\sigma_{kk} \tag{2.7}$$

is the hydrostatic stress, and μ_+, μ_- are chemical potentials of the ions defined as follows:

$$\mu_+ = \mu_{0,+} + RT\log(f_+\frac{c_+}{c_0}) - \Omega_+ p + Fz_+\varphi \tag{2.8}$$

$$\mu_- = \mu_{0,-} + RT\log(f_-\frac{c_-}{c_0}) - \Omega_- p + Fz_-\varphi. \tag{2.9}$$

Note here that while the individual chemical potentials of the cations and anions, respectively, account for the electrostatic field, this effect is absent in the consideration of the effective chemical potential due to the charge neutrality of the salt, i.e.,

$$\nu_+ z_+ + \nu_- z_- = 0. \tag{2.10}$$

We also note that the chemical potential (2.5) accounts for the coupling of the elastic field through the pressure.

We progress by setting up the general governing equations of lithium transport in the electrolyte region. A similar analysis can be found in the work of [14, 29–31, 59–61, 86, 87, 93]. Finally, we solve for the concentration and potential profile specifically for the case of a solid electrolyte, LIPON.

Initially, conservation of mass demands that

$$\frac{\partial c_+}{\partial t} + \nabla \cdot \boldsymbol{J}_+ = 0, \tag{2.11}$$

where c_+ is the concentration of Li^+ $[mol/m^3]$ and $\boldsymbol{J}_+$ the vector flux of Li^+, in moles per unit time per unit area, through the electrolyte.

As a second governing equation, charge balance is considered in the following form:

$$\frac{\partial \varrho_e}{\partial t} + \nabla \cdot \boldsymbol{i} = 0, \tag{2.12}$$

where $\boldsymbol{i}$ is the total current density $[A/m^2]$ and ϱ_e is the charge density $[C/m^3]$. Due to charge neutrality in the salt, the charge density always sums up to zero, i.e.,

$$\varrho_e = z_+ c_+ + z_- c_- = 0. \tag{2.13}$$

In order to complete the formulation, conservation of linear momentum requires that

$$\nabla \cdot \boldsymbol{\sigma} = \underline{0}. \tag{2.14}$$

The constitutive relations for the fluxes are derived from the governing equations in the electrolyte, that have been formulated earlier. More specifically, we start with the constitutive equation for the ion flux. This equation appears in the following form:

$$\boldsymbol{J}_+ = -c_+ M(c_+) \nabla \mu^E + \frac{t_+}{z_+ F} \boldsymbol{i}, \tag{2.15}$$

where

$$M(c_+) = \frac{D}{RT} f(c_+) = M_0 f(c_+) \tag{2.16}$$

is the mobility coefficient $[m^2 mol/(sJ)]$, concentration dependent, of lithium through the lattice, D is the diffusion coefficient $[m^2/s]$, and finally the function f is defined as follows:

$$f(c_+) = \begin{cases} 1 - \frac{c_+}{c_{+,max}} & \text{, for solid electrolyte} \\ \\ \frac{c_T}{\nu c_o} & \text{, for aqueous electrolyte.} \end{cases}$$

This implies that in the case that all the solid electrolyte lattice sites are occupied by lithium ions, i.e., $c_+ = c_{+,max}$, the mobility coefficient drops down to zero. As noted in the literature [16], it never takes the value zero but in such case it is a couple of orders of magnitude less than its original value.

Completing the formulation, we finally consider the constitutive equation for the electric current to follow as

$$\boldsymbol{i} = -\kappa \nabla \varphi + \frac{\kappa t_-}{z_+ F} \nabla \mu^E, \tag{2.17}$$

where κ is the conductance $[A/(Vm)]$ and t_+, t_- are transference number of ions $(t_+ + t_- = 1)$.

So far, the formulation of transport in the electrolyte is general and valid for all models of electrolyte material. In case of a solid electrolyte, e.g., LIPON, the concentration gradients are negligible in the bulk of the material since the concentration of

the Li^+ remains constant through the electrolyte. Therefore, mass and charge balance (2.11) and (2.12) reduces to

$$\Delta\varphi = 0, \tag{2.18}$$

that is, the potential satisfies Laplace's equation in a region of uniform composition. This result is consistent with the literature [75].

Applying the following boundary conditions for the electrostatic potential φ,

- at $x_3 = 0 \Rightarrow \varphi(0) = 0(V)$
- at $x_3 = L \Rightarrow \varphi(L) = 2(V)$,

we obtain a linear response of the potential as a function of the x_3 variable from equation (2.18).

2.2 Electrode-Electrolyte Interface Energy and Kinetics

Next we consider the kinetics of the electrode-electrolyte interface growth resulting from interfacial mass transport. We suppose that the kinetics of the interface is governed by three main mechanisms: i) interfacial diffusion; ii) electrochemical deposition; and iii) the chemical potential resulting from interfacial and bulk free-energies, including the coupling to the elastic field. We proceed to consider these contributions in turn.

We assume the interfacial mass flux $\boldsymbol{j}_p$ of Li^+ to be of the form

$$\boldsymbol{j}_p = -\nabla(D_1 h + D_2 \nabla^2 h), \tag{2.19}$$

where ∇ denotes the in-plane gradient and D_1 $[m^2/s]$ and D_2 $[m^4/s]$ are surface diffusivities. The first term in (2.19) accounts for Mullins diffusion by particle exchange between the electrode and the electrolyte, whereas the second term models Herring-Mullins capillarity-driven interfacial diffusion [7, 48, 58, 73].

We additionally assume the mass flux j_m of Li^+ from the electrolyte to the electrode, in units of moles per unit time per unit area, to be governed by diffusion controlled adsorption and by a linear kinetic equation of the form

$$j_m = \frac{Kd}{\Omega}\frac{\mu^E - \mu_0^{\mathrm{S}}}{RT}, \tag{2.20}$$

where μ^E is given by (2.5), μ_0^S is the ideal chemical potential per mole $[J/mol]$ of Li in the solid electrode, d is the atomic interplanar distance in the solid electrode, and K $[1/s]$ is an equilibrium exchange rate coefficient for mass transfer between the electrolyte and the electrode.

The above equation (2.20) is the linearized version of the Butler-Volmer (B-V) equation, which is usually used in the literature [60] to describe the transport of ions across the interface. The ionic current density follows from the Butler-Volmer approach as

$$i_{ion} = i_0 \left\{ exp\Big(\frac{\alpha_a F}{RT}\eta_s\Big) - exp\Big(-\frac{\alpha_c F}{RT}\eta_s\Big) \right\}, \tag{2.21}$$

where i_0 is the concentration of Li^+ dependent exchange current density $[A/m^2]$ which is an interfacial property and should not be confused with the charging current density, α_a and α_c are the anodic and cathodic transfer coefficients, respectively (dimensionless, $\alpha_a + \alpha_c = 1$), and η_s is the surface overpotential $[V]$ given by

$$\eta_s = \varphi^S - \varphi^E - \frac{\mu^E - \mu^S}{z_+ F}, \tag{2.22}$$

where the label E refers to the electrolyte and the label S refers to the solid electrode. Finally, for small values of ratio i_{ion}/i_0 (≤ 0.4) the B-V equation can be linearized, without any significant loss of accuracy, as follows from (2.20) where

$$\frac{Kd}{\Omega} = \frac{i_0}{F}. \tag{2.23}$$

Lastly, we account for deposition driven by the energetics of the interface and the electrode-electrolyte system. In order to identify the corresponding driving force, we begin by noting that the free-energy $E[h]$ of the system per unit area of the interface at equilibrium depends, parametrically, on the interface profile function $h(x_1, x_2, t)$. The corresponding chemical potential density $[J/m^3]$ is given by the functional derivative

$$\mu_h = \frac{\delta E}{\delta h}. \tag{2.24}$$

Assuming linear kinetics, the corresponding mass deposition rate j_h, in units of moles per unit time per unit area, is proportional to μ_h, i.e.,

$$j_h = -\frac{Kd}{RT}\mu_h = -\frac{Kd}{RT}\frac{\delta E}{\delta h}. \tag{2.25}$$

Taking into account all the mechanisms of mass transport just described gives the equation of evolution for the surface profile

$$\frac{\partial h}{\partial t} + \nabla \cdot \boldsymbol{j}_p = \Omega(j_m + j_h), \tag{2.26}$$

or

$$\frac{\partial h}{\partial t} = \nabla^2(D_1 h + D_2 \nabla^2 h) + \frac{Kd}{RT}(\mu^E - \mu_0^S) - \frac{\Omega Kd}{RT}\frac{\delta E}{\delta h}. \tag{2.27}$$

This equation describes the evolution of the surface profile function. In order to complete the definition of the governing equations, an explicit expression for the dependence of E on h is required. This dependence is derived later, section 2.4, by recourse to an asymptotic analysis [40, 41, 96].

2.3 List of Key Assumptions

The mathematical model developed so far is based on some key assumptions. All these assumptions are listed below:

- The terms in the equation of bulk free-energy, equation (2.2), that account for the electrostatic field and the coupling between the electrostatic and the elastic

fields, can be neglected. This assumption is valid in the case that the electric permittivity ε of the electrolyte takes really small values compared to the rest quantities.

- Charge neutrality of the salt is assumed
- The concentration of the Li^+ remains constant in the case of a solid electrolyte, e.g., LIPON
- The Butler-Volmer (B-V) equation can be linearized and take the form of equation (2.20) for small values of ratio i_{ion}/i_0.
- The dependence of E on h is found by assuming an interface that is shallow and nearly flat

2.4 The Nearly Flat Electrode-Electrolyte Interface

We wish to estimate the dependence of the free-energy of an idealized electrode-electrolyte system on a possibly non-planar profile $\{x_3 = h(x_1, x_2, t)\}$ of the interface. We derive this estimate asymptotically in the limit of a shallow, or nearly flat interface. Conveniently, this asymptotic limit suffices to establish the linear stability properties of a planar interface, which is the main focus of the present work.

Since we are only interested in the local behavior of the interface, we may idealize the domain of the electrolyte as being $\{h(x_1, x_2, t) < x_3 < +\infty\}$, and the domain of

the Li electrode as being $\{-\infty < x_3 < h(x_1, x_2, t)\}$, c.f., Fig. 2.1.

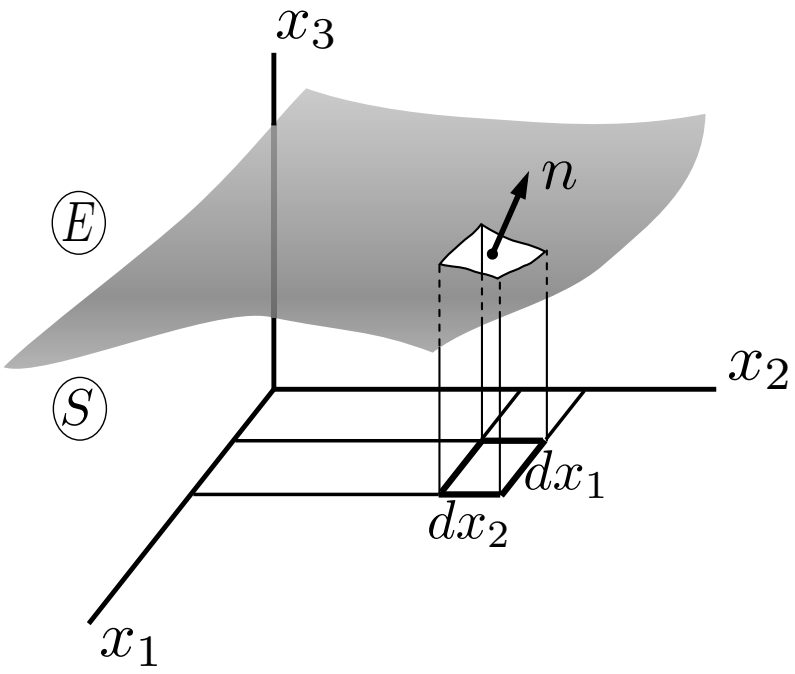

Figure 2.1: Electrolyte (E)-electode (S) domain and area projection on the plane.

Next let us consider the function, g, as follows:

$$g(x_1, x_2, x_3, t) = x_3 - h(x_1, x_2, t). \tag{2.28}$$

Then, to leading order in $|\nabla h|$, the corresponding unit normal to the interface is given by

$$\boldsymbol{n} = \nabla g = \frac{\partial g}{\partial x_1}\boldsymbol{e}_1 + \frac{\partial g}{\partial x_2}\boldsymbol{e}_2 + \frac{\partial g}{\partial x_3}\boldsymbol{e}_3 = (-h_{,1}\,, -h_{,2}\,, 1), \tag{2.29}$$

where e_i is the standard basis.

Whereas the element of area is

$$dA \sim (1 + \frac{1}{2}|\nabla h|^2)\, dx_1 dx_2. \tag{2.30}$$

From this latter identity, the interfacial energy differential with respect to the planar interface follows to leading order as

$$E^{\text{int}}[h] = \int \frac{\gamma}{2}|\nabla h|^2\, dx_1 dx_2, \tag{2.31}$$

where γ is the interfacial energy per unit area.

In addition to the concentration and electrostatic fields, that were defined previously in section 2.1, the planar interface carries along an elastic field. We specifically assume a piecewise uniform and equilibrated prestrain field $\epsilon^*_{ij}(\boldsymbol{x}, t)$ and residual stress field $\sigma^*_{ij}(\boldsymbol{x}, t)$ at zero Li^+ concentration. As a result, in the planar frame, we have

$$\epsilon^*_{ij} = \epsilon^{*E}_{ij}, \qquad x_3 > 0 \tag{2.32a}$$

$$\epsilon^*_{ij} = \epsilon^{*S}_{ij}, \qquad x_3 < 0 \tag{2.32b}$$

$$\sigma^*_{ij} = -c^E_{ijkl}\epsilon^{*E}_{kl} \equiv \sigma^{*E}_{ij}, \qquad x_3 > 0 \tag{2.32c}$$

$$\sigma^*_{ij} = -c^S_{ijkl}\epsilon^{*S}_{kl} \equiv \sigma^{*S}_{ij}, \qquad x_3 < 0 \tag{2.32d}$$

$$\sigma^{*E}_{i3} - \sigma^{*S}_{i3} = 0, \qquad x_3 = 0. \tag{2.32e}$$

Thus, for the planar interface the elastic field consists of equilibrated constant residual stresses σ^{*E}_{ij} and σ^{*S}_{ij} in the electrolyte and the solid electrode, respectively.

However, the deviation from the planar profile modifies the planar elastic field (2.32) to leading order in $|\nabla h|$. The corresponding correction displacement field $\boldsymbol{u}$ satisfies the problem,

$$\sigma^S_{ij,j}(u) = 0, \qquad x_3 < h(x_1, x_2, t), \tag{2.33a}$$

$$\sigma^E_{ij,j}(u) = 0, \qquad x_3 > h(x_1, x_2, t), \tag{2.33b}$$

$$\begin{aligned} &\sigma^E_{i3}(u) - \big(\sigma^{*E}_{i\beta} + \sigma^E_{i\beta}(u)\big)h_{,\beta} = \\ &\sigma^S_{i3}(u) - \big(\sigma^{*S}_{i\beta} + \sigma^S_{i\beta}(u)\big)h_{,\beta}\,, \end{aligned} \qquad x_3 = h(x_1, x_2, t), \tag{2.33c}$$

$$u_i \to 0, \qquad x_3 \to \pm\infty, \tag{2.33d}$$

where, here and subsequently, Greek indices take values in $\{1, 2\}$, and we write

$$\sigma^S_{ij}(u) = c^S_{ijkl}\epsilon^S_{kl}(u) \tag{2.34a}$$

$$\sigma^E_{ij}(u) = c^E_{ijkl}\epsilon^E_{kl}(u). \tag{2.34b}$$

In order to fix the geometry, we introduce the change of variables

$$u_i(x_1, x_2, x_3, t) = v_i\big(x_1, x_2, x_3 - h(x_1, x_2, t), t\big). \tag{2.35}$$

We have

$$u_{i,\alpha} = v_{i,\alpha} - v_{i,3}h_{,\alpha}\,, \tag{2.36a}$$

$$u_{i,3} = v_{i,3}, \tag{2.36b}$$

or

$$u_{i,j} = v_{i,j} - v_{i,3} h_{,\beta}\, \delta_{j\beta}, \tag{2.37}$$

whence

$$\epsilon_{ij}(u) = \epsilon_{ij}(v) - \frac{1}{2}(v_{i,3}\delta_{\beta j} + v_{j,3}\delta_{\beta i}) h_{,\beta} \tag{2.38}$$

and

$$\sigma_{ij}(u) = \sigma_{ij}(v) - c_{ijk\delta} v_{k,3} h_{,\delta}\,. \tag{2.39}$$

In this representation, the equilibrium problem becomes, to first order,

$$\sigma^S_{ij,j}(v) = 0, \qquad x_3 < 0, \tag{2.40a}$$

$$\sigma^E_{ij,j}(v) = 0, \qquad x_3 > 0, \tag{2.40b}$$

$$\sigma^E_{i3}(v) - \sigma^{*E}_{i\beta} h_{,\beta} = \sigma^S_{i3}(v) - \sigma^{*S}_{i\beta} h_{,\beta}\,, \qquad x_3 = 0, \tag{2.40c}$$

$$v_i \to 0, \qquad x_3 \to \pm\infty. \tag{2.40d}$$

The attendant change in elastic energy is (c.f., section 2.5 for a derivation based on the Fourier transform)

$$E^{\text{ela}} = \int_{\mathbb{R}^2}\int_{\mathbb{R}^2} \frac{1}{2} G_{ik}(\boldsymbol{x} - \boldsymbol{x}') [\![\sigma^*_{i\beta}]\!] [\![\sigma^*_{k\delta}]\!] h_{,\beta}\,(\boldsymbol{x}) h_{,\delta}\,(\boldsymbol{x}')\, d\boldsymbol{x}\, d\boldsymbol{x}', \tag{2.41}$$

where

$$[\![\sigma^*_{ij}]\!] = \sigma^{*E}_{ij} - \sigma^{*S}_{ij}, \tag{2.42}$$

is the jump in the residual stress tensor at the interface, and $\boldsymbol{G}(\boldsymbol{x}, \boldsymbol{x}')$ is the interfacial

Green's function (c.f., section 2.6).

The total elastic energy differential with respect to the planar interface is

$$E[h] = E^{\text{int}}[h] + E^{\text{ela}}[h] = \int_{\mathbb{R}^2} \frac{\gamma}{2} |\nabla h|^2 \, d\boldsymbol{x} + \int_{\mathbb{R}^2} \int_{\mathbb{R}^2} \frac{1}{2} G_{ik}(\boldsymbol{x} - \boldsymbol{x}') [\![\sigma^*_{i\beta}]\!] [\![\sigma^*_{k\delta}]\!] h_{,\beta}(\boldsymbol{x}) h_{,\delta}(\boldsymbol{x}') \, d\boldsymbol{x} \, d\boldsymbol{x}'. \tag{2.43}$$

Note here that the total elastic energy change vanishes for the case of planar interface, i.e., $h_{,\alpha} = 0$.

The corresponding functional derivative in the equation of evolution (2.27) may now be written explicitly as

$$\frac{\delta E}{\delta h}(\boldsymbol{x}) = -\gamma \nabla^2 h(\boldsymbol{x}) - \int_{\mathbb{R}^2} G_{ik,\beta}(\boldsymbol{x} - \boldsymbol{x}') [\![\sigma^*_{i\beta}]\!] [\![\sigma^*_{k\delta}]\!] h_{,\delta}(\boldsymbol{x}') \, d\boldsymbol{x}'. \tag{2.44}$$

2.5 Elastic Energy of a Planar Interface

We wish to compute the energy of a planar interface $\{x_3 = 0\}$ separating two semi-infinite linear-elastic solids and subject to prescribed tractions $\boldsymbol{t}$, c.f., Fig. 2.2. This derivation is based on the properties of the Fourier transform and the surface Green's function, which is also numerically obtained in the later section. The relationship between the displacement field of the electrode-electrolyte interface, which expresses the deviation from flatness, and the surface Green's function is finally also developed.

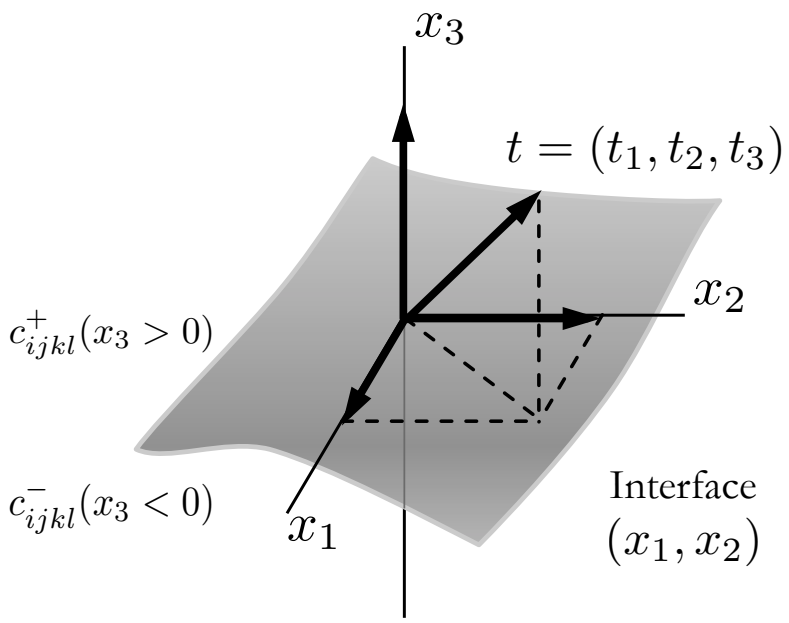

Figure 2.2: An anisotropic bimaterial full-space subject to prescribed tractions $\boldsymbol{t}$ [82].

We begin by setting the governing equations as follows:

$$\sigma^{\pm}_{ij,j} = 0, \qquad \pm x_3 > 0, \tag{2.45a}$$

$$\sigma^{\pm}_{ij} = c^{\pm}_{ijkl}\epsilon^{\pm}_{kl}, \qquad \pm x_3 > 0, \tag{2.45b}$$

$$\epsilon^{\pm}_{ij} = \frac{1}{2}(u^{\pm}_{i,j} + u^{\pm}_{j,i}), \qquad \pm x_3 > 0, \tag{2.45c}$$

$$u^{+}_{i} = u^{-}_{i}, \qquad x_3 = 0, \tag{2.45d}$$

$$\sigma^{+}_{i3} - \sigma^{-}_{i3} = t_i, \qquad x_3 = 0, \tag{2.45e}$$

$$u^{\pm}_{i} \to 0, \qquad x_3 \to \pm\infty, \tag{2.45f}$$

where the labels $(+)$ and $(-)$ refer to the regions $\{x_3 > 0\}$ and $\{x_3 < 0\}$, respectively.

We characterize the solution by means of the in-plane Fourier transform

$$\hat{f}(k_1, k_2, x_3) \equiv \int_{-\infty}^{\infty}\int_{-\infty}^{\infty} f(x_1, x_2, x_3)\mathrm{e}^{-i(k_1x_1+k_2x_2)}\, dx_1dx_2. \tag{2.46}$$

Applying this transform to the governing equations, we obtain

$$i\hat{\sigma}^{\pm}_{i\beta}k_\beta + \hat{\sigma}^{\pm}_{i3,3} = 0, \qquad \pm x_3 > 0, \tag{2.47a}$$

$$\hat{\sigma}^{\pm}_{ij} = c^{\pm}_{ijkl}\hat{\epsilon}^{\pm}_{kl}, \qquad \pm x_3 > 0, \tag{2.47b}$$

$$\hat{\epsilon}^{\pm}_{\alpha\beta} = \frac{1}{2}(i\hat{u}^{\pm}_\alpha k_\beta + i\hat{u}^{\pm}_\beta k_\alpha), \qquad \pm x_3 > 0, \tag{2.47c}$$

$$\hat{\epsilon}^{\pm}_{\alpha 3} = \frac{1}{2}(\hat{u}^{\pm}_{\alpha,3} + i\hat{u}^{\pm}_3 k_\alpha), \qquad \pm x_3 > 0, \tag{2.47d}$$

$$\hat{\epsilon}^{\pm}_{33} = \hat{u}^{\pm}_{3,3}, \qquad \pm x_3 > 0, \tag{2.47e}$$

$$\hat{u}^{+}_i = \hat{u}^{-}_i, \qquad x_3 = 0, \tag{2.47f}$$

$$\hat{\sigma}^{+}_{i3} - \hat{\sigma}^{-}_{i3} = \hat{t}_i, \qquad x_3 = 0, \tag{2.47g}$$

$$\hat{u}^{\pm}_i \to 0, \qquad x_3 \to \pm\infty, \tag{2.47h}$$

where, here and subsequently, Greek indices take the values $\{1, 2\}$. Combining the above equations yields the second-order ODE problem

$$A^{\pm}_{ik}(\boldsymbol{k})\hat{u}^{\pm}_{k,33} + iB^{\pm}_{ik}(\boldsymbol{k})\hat{u}^{\pm}_{k,3} + C^{\pm}_{ik}(\boldsymbol{k})\hat{u}^{\pm}_k = 0, \tag{2.48a}$$

$$\hat{u}^{+}_i(\boldsymbol{k}, 0) = \hat{u}^{-}_i(\boldsymbol{k}, 0), \tag{2.48b}$$

$$\hat{\sigma}^{+}_{i3}(\boldsymbol{k}, 0) - \hat{\sigma}^{-}_{i3}(\boldsymbol{k}, 0) = \hat{t}_i(\boldsymbol{k}), \tag{2.48c}$$

$$\hat{u}^{\pm}_i(\boldsymbol{k}, x_3) \to 0, \quad x_3 \to \pm\infty, \tag{2.48d}$$

where

$$A_{ik}^{\pm}(\boldsymbol{k}) = c_{i3k3}^{\pm}, \tag{2.49a}$$

$$B_{ik}^{\pm}(\boldsymbol{k}) = c_{i\beta k3}^{\pm} k_{\beta} + k_{\delta} c_{i3k\delta}^{\pm}, \tag{2.49b}$$

$$C_{ik}^{\pm}(\boldsymbol{k}) = -c_{i\beta k\delta}^{\pm} k_{\beta} k_{\delta}. \tag{2.49c}$$

Inserting trial solutions of the form

$$\hat{u}_i^{\pm}(\boldsymbol{k}, x_3) = U_i^{\pm}(\boldsymbol{k}) \mathrm{e}^{\lambda(\boldsymbol{k}) x_3}, \tag{2.50}$$

we obtain the characteristic equation

$$\det\left(\boldsymbol{A}^{\pm}\lambda^2 + i\boldsymbol{B}^{\pm}\lambda + \boldsymbol{C}^{\pm}\right) = 0. \tag{2.51}$$

The (+) equation has three roots with negative real part $\{\lambda_1^+(\boldsymbol{k}), \lambda_2^+(\boldsymbol{k}), \lambda_3^+(\boldsymbol{k})\}$ and three corresponding unit eigenvectors $\{\boldsymbol{U}_1^+(\boldsymbol{k}), \boldsymbol{U}_2^+(\boldsymbol{k}), \boldsymbol{U}_3^+(\boldsymbol{k})\}$, whereas the $(-)$ equation has three roots with positive real part $\{\lambda_1^-(\boldsymbol{k}), \lambda_2^-(\boldsymbol{k}), \lambda_3^-(\boldsymbol{k})\}$ and three corresponding unit eigenvectors $\{\boldsymbol{U}_1^-(\boldsymbol{k}), \boldsymbol{U}_2^-(\boldsymbol{k}), \boldsymbol{U}_3^-(\boldsymbol{k})\}$. By superposition,

$$\hat{u}_i^{\pm}(\boldsymbol{k}, x_3) = \sum_{p=1}^{3} V_p^{\pm}(\boldsymbol{k}) U_{pi}^{\pm}(\boldsymbol{k}) \mathrm{e}^{\lambda_p^{\pm}(\boldsymbol{k}) x_3}, \tag{2.52}$$

where the six scalar amplitudes $\{V_1^{\pm}(\boldsymbol{k}), V_2^{\pm}(\boldsymbol{k}), V_3^{\pm}(\boldsymbol{k})\}$ follow from the system defined by the six equations (2.48b) and (2.48c).

In addition, we have

$$u_i(x_1, x_2, 0) = \int_{-\infty}^{+\infty} \int_{-\infty}^{+\infty} G_{ik}(x_1 - x_1', x_2 - x_2') t_k(x_1', x_2') dx_1' dx_2', \tag{2.53}$$

or

$$u_i(\boldsymbol{x}) = \int_{\mathbb{R}^2} G_{ik}(\boldsymbol{x} - \boldsymbol{x}') t_k(\boldsymbol{x}') d\boldsymbol{x}', \tag{2.54}$$

which can be written in the convolution form

$$u_i(\boldsymbol{x}) = G_{ik}(\boldsymbol{x}) * t_k(\boldsymbol{x}), \tag{2.55}$$

where the Green's function, $G_{ik}(\boldsymbol{x} - \boldsymbol{x}')$, is the displacement component in the x_i-direction at point $\boldsymbol{x}$ when a unit body force in the x_k-direction is applied at point $\boldsymbol{x}'$ in the infinitely extended material, as noted in [74].

Applying the Fourier transform in equation (2.55) we get

$$\begin{aligned}
\int_{\mathbb{R}^2} u_i(\boldsymbol{x}) e^{-i\boldsymbol{k}\cdot\boldsymbol{x}} d\boldsymbol{x} &= \int_{\mathbb{R}^2} \int_{\mathbb{R}^2} G_{ik}(\boldsymbol{x} - \boldsymbol{x}') t_k(\boldsymbol{x}') e^{-i\boldsymbol{k}\cdot\boldsymbol{x}} d\boldsymbol{x}' d\boldsymbol{x} \Rightarrow \\
\hat{u}_i(\boldsymbol{k}, 0) &= \int_{\mathbb{R}^2} \int_{\mathbb{R}^2} G_{ik}(\boldsymbol{y}) t_k(\boldsymbol{x}') e^{-i\boldsymbol{k}\cdot(\boldsymbol{y}+\boldsymbol{x}')} d\boldsymbol{x}' d\boldsymbol{y} \Rightarrow \\
\hat{u}_i(\boldsymbol{k}, 0) &= \left(\int_{\mathbb{R}^2} G_{ik}(\boldsymbol{y}) e^{-i\boldsymbol{k}\cdot\boldsymbol{y}} d\boldsymbol{y} \right) \left(\int_{\mathbb{R}^2} t_k(\boldsymbol{x}') e^{-i\boldsymbol{k}\cdot\boldsymbol{x}'} d\boldsymbol{x}' \right) \Rightarrow \\
\hat{u}_i(\boldsymbol{k}, 0) &= \hat{G}_{ik}(\boldsymbol{k}) \hat{t}_k(\boldsymbol{k}).
\end{aligned} \tag{2.56}$$

By the work-energy theorem, the energy of the interface follows as

$$E^{\text{ela}} = \int_{-\infty}^{\infty} \int_{-\infty}^{\infty} \frac{1}{2} \hat{t}_i(k_1, k_2) \hat{u}_i^*(k_1, k_2, 0)\, dk_1 dk_2, \tag{2.57}$$

or

$$E^{\text{ela}} = \int_{-\infty}^{\infty}\int_{-\infty}^{\infty} \frac{1}{2}\hat{G}_{ik}(k_1,k_2)\hat{t}_i(k_1,k_2)\hat{t}_k^*(k_1,k_2)\, dk_1 dk_2. \tag{2.58}$$

Alternatively, an application of the inverse Fourier transform gives

$$E^{\text{ela}} = \int_{\mathbb{R}^2}\int_{\mathbb{R}^2} \frac{1}{2}G_{ik}(\boldsymbol{x}-\boldsymbol{x}')t_i(\boldsymbol{x})t_k(\boldsymbol{x}')\, d\boldsymbol{x}\, d\boldsymbol{x}', \tag{2.59}$$

which corresponds to the change in elastic energy with respect to the planar interface.

2.6 Evaluation of Green's Function

The evaluation of the Green's function is important for the stability analysis since it is utilized in the dependence of the critical unstable wavenumber, k_c, on the elastic prestress. Therefore, a MATLAB [44] code has been built which accounts for the computation of the 3x3 matrix $\hat{G}_{ik}(\boldsymbol{k})$, c.f., Appendix B. This code requires as input data the stiffness matrices, with elements $c^{\pm}_{ijkl}$, for each material region and the wavenumbers, k_α, in the two in-plane directions. Specifying these data, the code calculates the Green's function matrix and determines the displacements and the stresses in the transformed domain subject to prescribed tractions $\boldsymbol{t}$.

We begin by specifying the material parameters of the electrolyte, LIPON. In particular, in the (+) region $\{x_3 > 0\}$, LIPON is considered an isotropic material, since it is amorphous. This means that the constitutive law can be parameterized by only two independent material constants. Thus, given its Poisson ratio and Young's modulus, which were taken from the work of [47, 78, 79], we can first find the Lamé

constants λ and μ and then compute the elements of the stiffness matrix as follows:

$$c^{+}_{ijkl} = \lambda^{+}\delta_{ij}\delta_{kl} + \mu^{+}(\delta_{ik}\delta_{jl} + \delta_{il}\delta_{jk}). \tag{2.60}$$

On the contrary, in the $(-)$ region $\{x_3 < 0\}$, lithium is a cubic material. In such case, we have to determine only three independent elements of the corresponding stiffness matrix, c^{-}_{ijkl}, which were found in literature [18]. In Voigt notation we have the stiffness matrix for cubic materials as follows:

$$c^{-} = \begin{pmatrix} c_{11} & c_{12} & c_{12} & 0 & 0 & 0 \\ c_{12} & c_{11} & c_{12} & 0 & 0 & 0 \\ c_{12} & c_{12} & c_{11} & 0 & 0 & 0 \\ 0 & 0 & 0 & c_{44} & 0 & 0 \\ 0 & 0 & 0 & 0 & c_{44} & 0 \\ 0 & 0 & 0 & 0 & 0 & c_{44} \end{pmatrix}. \tag{2.61}$$

Finally, regarding the wavenumbers, k_α, typical values have been selected, suggested by experimentalists (Robert Bosch GmbH, Stuttgart Germany) who measured the roughness of a lithium-LIPON interface.

	Lithium $(x_3 < 0)$	**LIPON** $(x_3 > 0)$
Elastic properties $[GPa]$	$c^{-}_{11} = 13.5$	$c^{+}_{11} = 103.6$
	$c^{-}_{12} = 11.44$	$c^{+}_{12} = 44.42$
	$c^{-}_{44} = 8.78$	$c^{+}_{44} = \frac{c^{+}_{11} - c^{+}_{12}}{2} = 29.61$
Wavenumbers $[\mu m^{-1}]$	$k_1 = k_2 = 2\pi$	

Table 2.1: Material parameters used in the computation of the Green's function matrix.

All the values of the material properties of a lithium-LIPON system required for this computation are summarized in Table 2.1.

Having determined the input data, we proceed to evaluate the Green's function matrix, $\hat{G}_{ik}(\boldsymbol{k})$. The steps of the algorithm used in this calculation are stated below:

- Fill-in the elasticity matrix $c^{\pm}_{ijkl}$ in both of the two regions
- Fill-in the symetric matrices $A^{\pm}$, $B^{\pm}$ and $C^{\pm}$ as defined by equations (2.49a-2.49c)
- Solve the quadratic eigenvalue problem equation (2.51)
- Choose the preferred eigenvectors/eigenvalues to form a base
- Apply interfacial conditions equations (2.48b) and (2.48c) and determine the displacement field from equation (2.52)
- Obtain $\hat{G}_{ik}(\boldsymbol{k})$ from equation (2.56) by choosing a unit load traction in each of the three directions.

Note here that since we are solving a three dimensional quadratic eigenvalue problem we expect to get six eigenvalues and six corresponding unit eigenvectors for each of the two regions. However, we want to get zero deviation from flatness far away from the interface, according to the restrictions of the problem, equation (2.48d). Since we assume solutions of exponential form ($e^{\lambda(\boldsymbol{k})x_3}$), equation (2.50), we keep only the ones that stabilize our solution according to the region we belong, i.e., sign of the x_3 coordinate. In particular, we choose for the solid electrolyte region $\{x_3 > 0\}$ the

Lithium	LIPON
-6.485029045942089 - 7.550186008034304 i	-8.885765892494279 + 1.033720047320573•10^{-7} i
-6.485029045942084 + 7.550186008034278 i	-8.885765860139180 - 1.033720059318343•10^{-7} i
6.485029045942115 - 7.550186008034348 i	8.885766004789142 - 9.689351381924029•10^{-8} i
6.485029045942116 + 7.550186008034339 i	8.885765747844310 + 9.689350985677532•10^{-8} i
-3.043450345808273 + 1.111050361295736•10^{-16} i	8.885765876316745 + 0.000000000000000 i
3.043450345808274 + 2.467869767995515•10^{-16} i	-8.885765876316732 + 0.000000000000000 i

Figure 2.3: Numerical values of the eigenvalues for each of the two regions. In the region of lithium we choose the three with positive real part (shown in green) and in the region of LIPON we choose the three with negative real part (shown in blue).

three eigenvalues with negative real part (so as $e^{(-)(+\infty)} \to 0$) and for the Li electrode region $\{x_3 < 0\}$ the three eigenvalues with positive real part (so as $e^{(+)(-\infty)} \to 0$). The actual numerical values for these eigenvalues and eigenvectors can be found in Figures 2.3 and 2.4.

Finally, we can numerically obtain the 3x3 Green's function matrix, $\hat{G}_{ik}(\boldsymbol{k})$, in the transformed domain, which will help us estimate the effect of the elastic prestress on the critical wavenumber of the perturbation. The Green's function matrix is Hermitian and positive definite, c.f., Fig. 2.5.

2.7 Result Verification

In the previous section, a three-dimensional Green's function for bimaterials was obtained within the context of the theory of linear elasticity. In particular, we solved an eigenvalue problem and computed the Green's function matrix, which allows eval-

Lithium	LIPON
-1.129941681081025•10^{-1} - 4.571641629722253•10^{-1} i	**5.000000010295000•10^{-1} - 2.276009602763592•10^{-5} i**
-1.129941681080993•10^{-1} - 4.571641629722247•10^{-1} i	**4.999999995734324•10^{-1} - 2.275078921116378•10^{-5} i**
1.766438888350875•10^{-2} - 7.457576426026746•10^{-1} i	**3.216624851582928•10^{-5} + 7.071067792962954•10^{-1} i**
4.621950652705032•10^{-1} + 9.023566685148678•10^{-2} i	**-7.728572808664340•10^{-2} - 4.939908042530704•10^{-1} i**
4.621950652705027•10^{-1} + 9.023566685148368•10^{-2} i	**-7.728573750667377•10^{-2} - 4.939908042534993•10^{-1} i**
-7.439701866149503•10^{-1} + 5.454221817127056•10^{-2} i	**6.986084950632698•10^{-1} - 1.092985464861540•10^{-1} i**
-1.098646255691343•10^{-1} + 4.579263237477074•10^{-1} i	3.373841462258488•10^{-5} - 5.000000111512124•10^{-1} i
-1.098646255691366•10^{-1} + 4.579263237477088•10^{-1} i	3.374713732277032•10^{-5} - 4.999999995840410•10^{-1} i
2.276478922055191•10^{-2} + 7.456193777703671•10^{-1} i	-7.071067703742639•10^{-1} - 4.773336914377410•10^{-5} i
-1.308238078364517•10^{-1} - 4.523846651199700•10^{-1} i	3.992146635473141•10^{-1} + 3.010442494373765•10^{-1} i
-1.308238078364541•10^{-1} - 4.523846651199714•10^{-1} i	3.992146780347184•10^{-1} + 3.010442494363978•10^{-1} i
1.157572160954692•10^{-2} + 7.458769971008250•10^{-1} i	4.257408604265189•10^{-1} - 5.645748247802864•10^{-1} i
-7.039921737611822•10^{-1} - 6.629494160948837•10^{-2} i	2.271767207848611•10^{-1} + 4.824587525597706•10^{-1} i
7.039921737611822•10^{-1} + 6.629494160948794•10^{-2} i	-8.473883635866555•10^{-2} + 4.824587525597677•10^{-1} i
-9.318463873737249•10^{-16} - 1.345050586521661•10^{-15} i	6.822997111556286•10^{-1} - 1.007187939756282•10^{-1} i
-1.164277806906109•10^{-3} + 7.071058226723839•10^{-1} i	**-1.875289917383101•10^{-1} - 3.923661425297861•10^{-1} i**
1.164277806906603•10^{-3} - 7.071058226723832•10^{-1} i	**-1.875289917383102•10^{-1} - 5.295461786158656•10^{-1} i**
1.185096272701747•10^{-15} - 2.850400910564731•10^{-1} i	**6.518904539415198•10^{-1} - 2.652060434544700•10^{-1} i**

Figure 2.4: Numerical values of the eigenvectors for each of the two regions. In the region of lithium we choose the three eigenvectors (shown in green) that correspond to the three eigenvalues with positive real part and in the region of LIPON we choose the three eigenvectors (shown in blue) that correspond to the three eigenvalues with negative real part.

$$\hat{G}_{ik} = \begin{pmatrix} 2.8050 + 7.0716\cdot10^{-10}\mathrm{i} & -6.4476\cdot10^{-1} + 5.5349\cdot10^{-9}\mathrm{i} & 5.5045\cdot10^{-9} + 3.2652\cdot10^{-1}\mathrm{i} \\ -6.4476\cdot10^{-1} - 3.7598\cdot10^{-10}\mathrm{i} & 2.8050 + 4.4518\cdot10^{-9}\mathrm{i} & 7.0772\cdot10^{-9} + 3.2652\cdot10^{-1}\mathrm{i} \\ -1.4595\cdot10^{-8} - 3.2652\cdot10^{-1}\mathrm{i} & -2.8774\cdot10^{-8} - 3.2652\cdot10^{-1}\mathrm{i} & 2.2303 - 3.2032\cdot10^{-8}\mathrm{i} \end{pmatrix}$$

Figure 2.5: Green's function matrix, $\hat{G}_{ik}(\boldsymbol{k})$, in the transformed domain. The parts of the values marked in blue can be assumed zero.

uation of the displacements, $\hat{u}_i$. Having obtained the displacements, which express the deviation from flatness, we can then determine the stresses, using the equations (2.47a-2.47e), all in the transformed domain.

In order to examine the validity of our computations, a theoretical verification has been conducted by comparing results of our model with similar results presented in the work of Pan and Yuan [82]. In particular, they solved a similar eigenvalue problem and obtained analytic expressions for the displacements and the stresses also in the transformed domain. However, in their analysis they used a different normalization relation and focused only on the elastic problem without considering any electrochemical coupling effects. As can be seen from the following set of figures, the results are found to be in perfect agreement.

Specifically, Figures 2.6-2.8 show the real and the imaginary part of the displacements as a function of the x_3 variable, in the transformed domain, in the case of a unit load applied in the three principal directions. It is important to note here that exactly at the interface ($x_3 = 0$), all the displacements are continuous, i.e., equation (2.47f), while away from the interface the deviation from flatness does become zero in agreement with equation (2.47h).

In addition, Figures 2.9-2.14 show the corresponding components of stresses in the transformed domain. Note that there is a jump in the appropriate stresses equal to the applied traction in accordance with equation (2.47g).

The material parameters used to produce the above plots are the same as before, c.f., Table 2.1, with one exception. Since the theory of PAN and YUAN works for

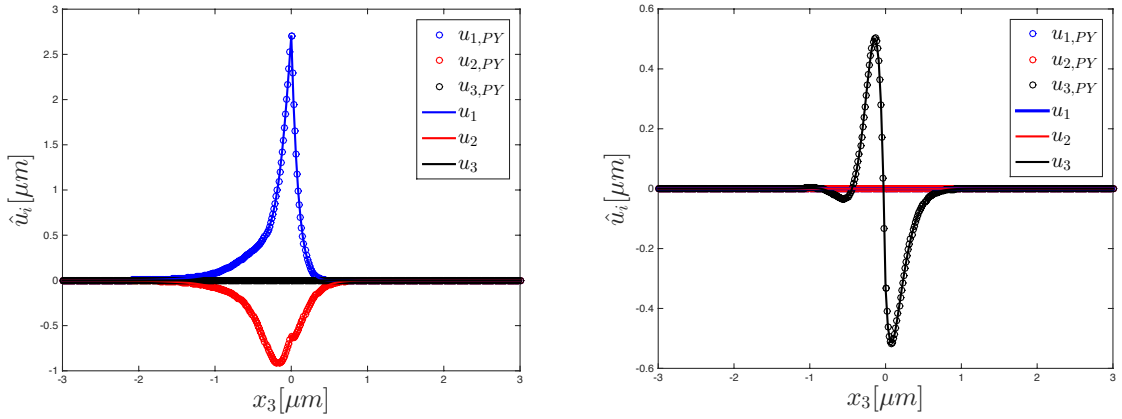

Figure 2.6: Real (left) and imaginary (right) parts of the three components of the displacements, in the transformed domain, as a function of x_3 for applied traction $\hat{t}_1 = [1, 0, 0]$. Comparison between the displacements of our model (solid lines) and the model of PAN and YUAN (circular points).

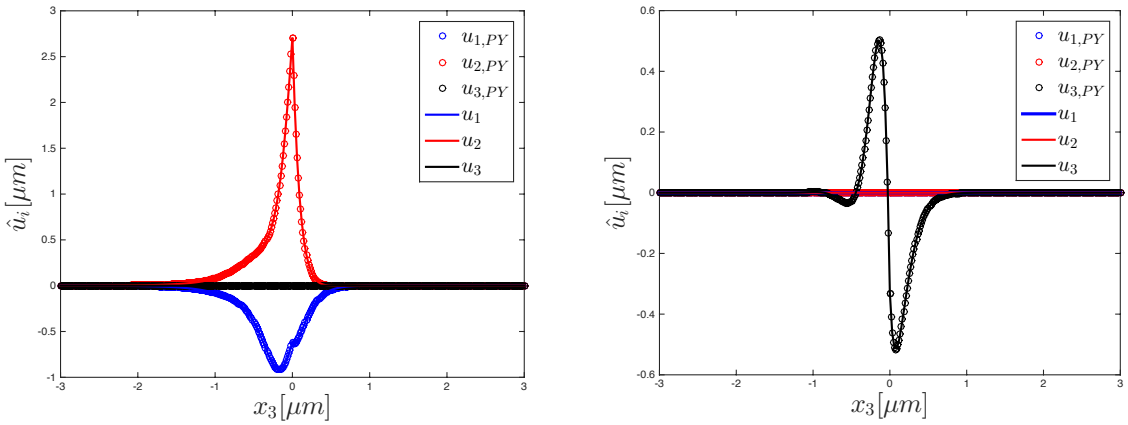

Figure 2.7: Real (left) and imaginary (right) parts of the three components of the displacements, in the transformed domain, as a function of x_3 for applied traction $\hat{t}_2 = [0, 1, 0]$. Comparison between the displacements of our model (solid lines) and the model of PAN and YUAN (circular points).

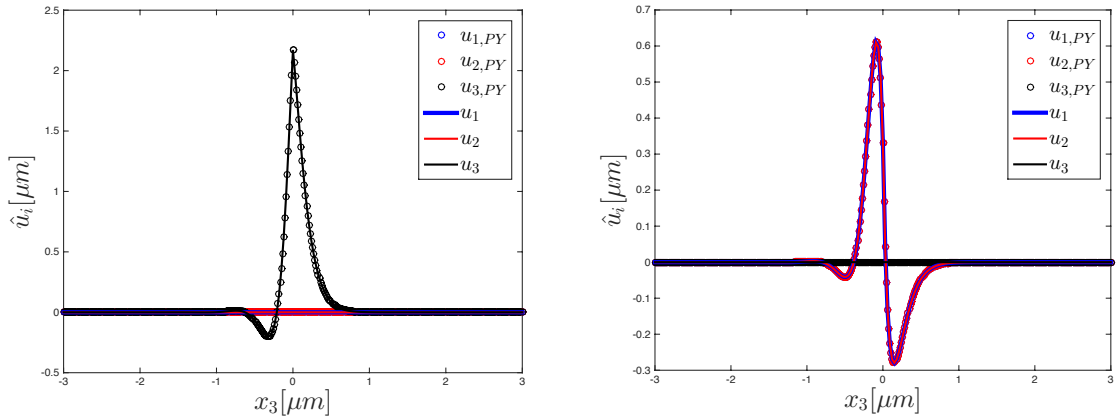

Figure 2.8: Real (left) and imaginary (right) parts of the three components of the displacements, in the transformed domain, as a function of x_3 for applied traction $\hat{t}_3 = [0, 0, 1]$. Comparison between the displacements of our model (solid lines) and the model of PAN and YUAN (circular points).

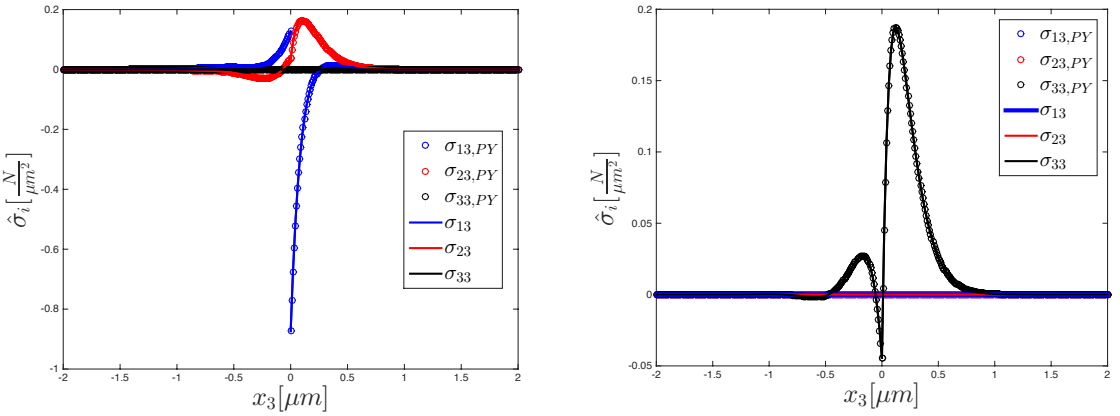

Figure 2.9: Real (left) and imaginary (right) parts of the three out-of-plane components of the stresses, in the transformed domain, as a function of x_3 for applied traction $\hat{t}_1 = [1, 0, 0]$. Comparison between the stresses of our model (solid lines) and the model of PAN and YUAN (circular points).

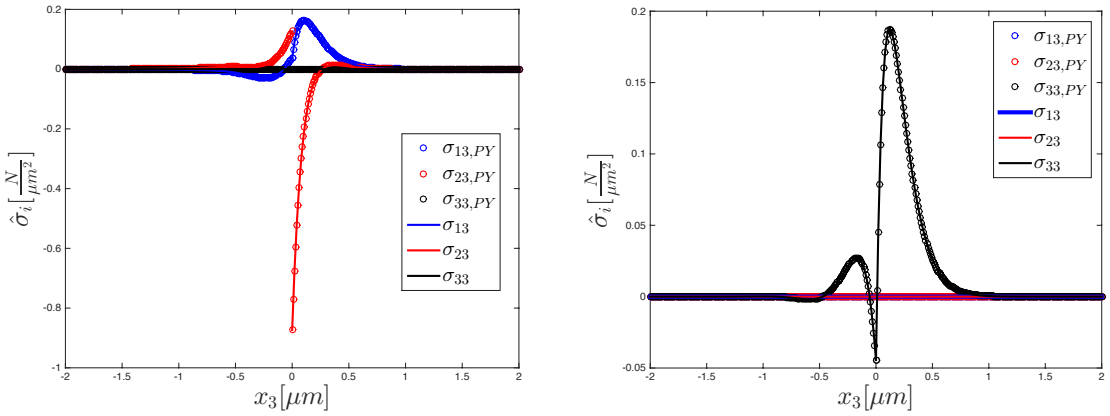

Figure 2.10: Real (left) and imaginary (right) parts of the three out-of-plane components of the stresses, in the transformed domain, as a function of x_3 for applied traction $\hat{t}_2 = [0, 1, 0]$. Comparison between the stresses of our model (solid lines) and the model of PAN and YUAN (circular points).

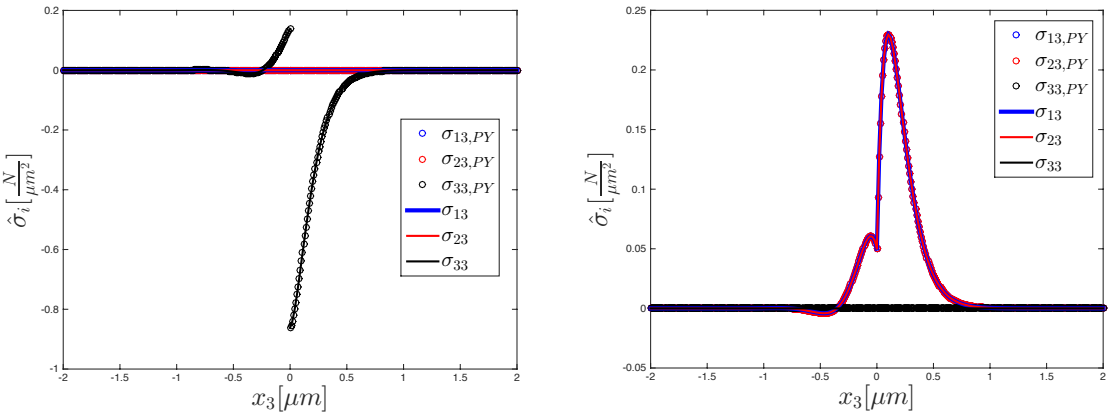

Figure 2.11: Real (left) and imaginary (right) parts of the three out-of-plane components of the stresses, in the transformed domain, as a function of x_3 for applied traction $\hat{t}_3 = [0, 0, 1]$. Comparison between the stresses of our model (solid lines) and the model of PAN and YUAN (circular points).

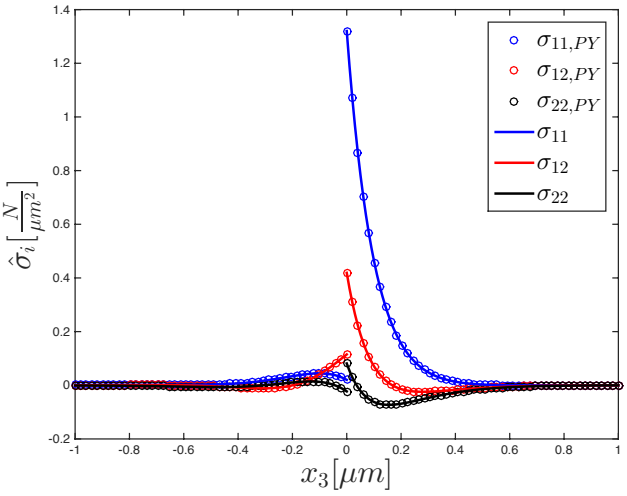

Figure 2.12: Imaginary parts (real parts are zero) of the three in-plane components of the stresses, in the transformed domain, as a function of x_3 for applied traction $\hat{t}_1 = [1, 0, 0]$. Comparison between the stresses of our model (solid lines) and the model of PAN and YUAN (circular points).

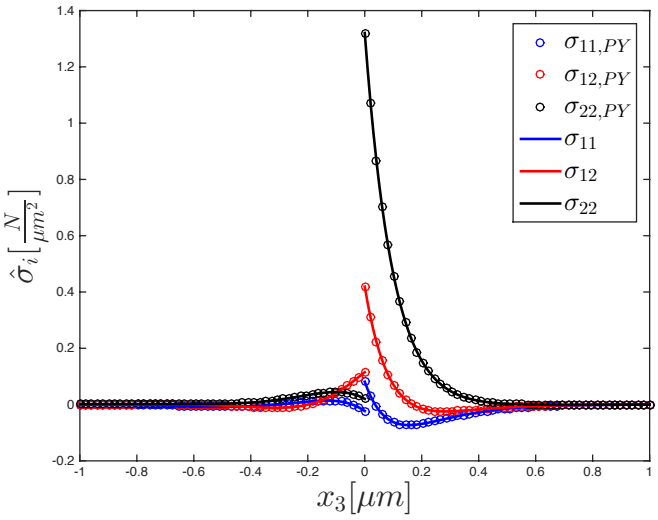

Figure 2.13: Imaginary parts (real parts are zero) of the three in-plane components of the stresses, in the transformed domain, as a function of x_3 for applied traction $\hat{t}_2 = [0, 1, 0]$. Comparison between the stresses of our model (solid lines) and the model of PAN and YUAN (circular points).

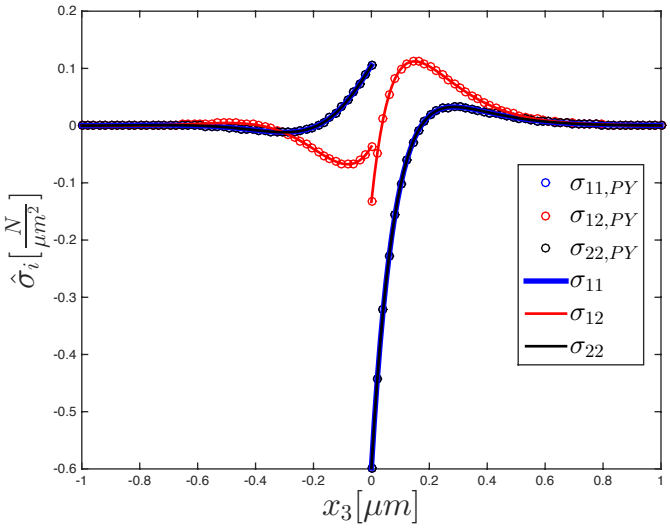

Figure 2.14: Real parts (imaginary parts are zero) of the three in-plane components of the stresses, in the transformed domain, as a function of x_3 for applied traction $\hat{t}_3 = [0, 0, 1]$. Comparison between the stresses of our model (solid lines) and the model of PAN and YUAN (circular points).

anisotropic materials (the eigenvalues need to be distinct) we had to modify LIPON from isotropic material to be cubic as in the case of lithium. Thus, in the LIPON region, the component $c_{44}^{+} = 32\ [GPa]$ of the stiffness matrix was used, instead of $c_{44}^{+} = \frac{c_{11}^{+} - c_{12}^{+}}{2} = 29.61\ [GPa]$ that was used before. All the rest of the values remain the same.

2.8 Summary

In this chapter, we derived the governing equations of lithium transport through the electrolyte. In particular, we solved for the concentration and electrostatic fields in the case of a solid electrolyte, LIPON. The mathematical framework was based on the consideration of the bulk free-energy density, which accounts for the coupling between

the electrostatic and elastic fields. Moreover, an asymptotic analysis was performed on a nearly flat interface and the elastic field was defined in this representation, along with the residual stresses from the planar interface. Lastly, taking into account the various transport mechanisms between the electrode-electrolyte surface, we developed the equation of evolution for the surface profile. This last equation is used to perform a stability analysis as a way to understand dendrite formation, an issue which continues to be the main focus of this work.

In addition, it was found that the total elastic energy differential with respect to the planar interface consists of two parts: i) the interfacial energy difference and ii) the elastic energy difference, which was derived based on the properties of Fourier transform and the interfacial Green's function. The surface Green's function matrix was also numerically obtained for the specific, lithium-LIPON, material system. Finally, we solved for the displacement and stress fields in the transformed, electrode-electrolyte domain, and the results presented were found to be in complete agreement with a similar study found in the literature.

Chapter 3

Surface Evolution - Visualization

The stability analysis that is performed in Chapter 5 enables us to tune fundamental parameters in order to have a stabilizing effect on the electrode-electrolyte interface. However, this method lacks the ability to provide us with the notion of surface evolution as a function of time. In this chapter, using the theory of finite differences, we present results on the surface evolution and its dependence on time. In particular, a numerical code is built based on a suitable finite difference scheme that applies to the simplified version of the equation that describes the evolution of the surface profile, which is a partial differential equation that enables the visualization of the surface evolution. The in-plane domain is discretized in both time and space and periodic boundary conditions are applied. As a first step, the effect of the elastic prestress is disregarded and the surface evolution depends only on surface diffusion and surface energetic deposition. Numerical results are presented for the case that the related parameters, the values of which are found in Chapter 5, result in a stable perturbation. Lastly, the effect of elastic prestress is added and numerical results are presented and compared with the previous case.

3.1 Finite Difference Method

A finite difference method (FDM) is a numerical method to approximate derivatives of functions using, for instance, the Taylor series expansion in an effort to solve differential equations, [45, 64, 69, 98]. The principal aim of this section is to apply a finite difference method to the simplified equation of surface evolution (2.27) on a periodic domain and examine the behavior of the interface. This partial differential equation includes the Laplacian, as well as the bi-Laplacian of the profile function, $h(x, y, t)$, and also another function of $h(x, y, t)$ in an integral form. Initially, we disregard the bi-Laplacian and the integral term and we only focus on an approximation of the Laplacian operator with a differentiation matrix. Once this differentiation matrix is defined, higher derivative operators, such as the bi-Laplacian operator, can be approximated by raising to powers the already determined matrix. Finally, the integral term will be handled in the last section by a recourse to the Fourier space.

We put forth a study of an initial value problem on the time interval [0,T] and on periodic domain Ω=[0,L]x[0,L] that is defined mathematically as follows.

A function h : [0,T]x[0,L]x[0,L]: $\rightarrow \mathbb{R}$ with the governing equation

$$h_t = D\nabla^2 h = D(h_{xx} + h_{yy}), \tag{3.1}$$

and the initial and periodic boundary conditions in $\Omega = [0, L]^2$

$$h(0, x, y) = h_0(x, y), \qquad h(t, x, y) = h(t, x + L, y) = h(t, x, y + L). \tag{3.2}$$

This formulation is based on the work of [55]. Note here and thereafter that we assume the surface diffusivities D_1, D_2 do not depend on the spatial coordinates. Also, for notational convenience, the two in-plane coordinates x_1 and x_2 are named x and y instead.

Next, we discretize the domain in both spatial directions in order to approximately compute the derivatives of the function. Thus we write

$$0 = x_1 < x_2 < ... < x_n = L, \tag{3.3}$$

where an equidistant discretization, $dx = x_{i+1} - x_i$, is used in both directions. The function h takes the values $H_{i,j} = h(x_i, x_j)$ on each grid point with coordinates x_i and x_j, where $i, j = 1, ..., n$. Using Taylor series expansion in both directions we can then approximate the Laplace operator at the (x_i, x_j) point as

$$\nabla^2 h_{|(x_i,x_j)} = \frac{H_{i,j-1} - 2H_{i,j} + H_{i,j+1}}{dx^2} + \frac{H_{i-1,j} - 2H_{i,j} + H_{i+1,j}}{dx^2} + O(dx^2), \tag{3.4}$$

which corresponds to a second order central difference approximation.

Finally, based on the differentiation scheme (3.4) we can write

$$\nabla^2 h \approx A_2 H, \tag{3.5}$$

where $A_2 \in \mathbb{R}^{N \times N}$ is a differentiation matrix that approximates the Laplace operator and H is a vector of size $N = n^2$ that stores all the n^2 function values in the following

form:

$$H = (H_{1,1}, H_{2,1}, ..., H_{n,1}, H_{1,2}, H_{2,2}, ..., H_{n,2}, H_{1,3}, ...)^T. \tag{3.6}$$

Notice that the differentiation scheme (3.4) takes into account only four neighboring points, i.e., $H_{i+1,j}$, $H_{i-1,j}$, $H_{i,j-1}$, and $H_{i,j+1}$, at a given point. Thus, the differentiation matrix A_2 has only five non-zero values in each row and in particular the value -4, which corresponds to the $H_{i,j}$ point, is positioned on the main diagonal, while values of ones are placed in the sub- and super-diagonals, as well as, n entries away on the left and on the right from the diagonal. In general, one typical row of the differentiation matrix A_2 is

$$row = \frac{1}{dx^2}(0, ..., 0, 1, 0, ..., 0, 1, -4, 1, 0, ..., 0, 1, 0, ...0). \tag{3.7}$$

In order to account for the periodic boundary conditions, equation (3.2), every time that the index in the scheme is bigger than N or less than 1 we account for the fact that

$$H_{i,j} = H_{i+n,j}, \qquad H_{i,j} = H_{i,j+n}. \tag{3.8}$$

Note here that the number of non-zero values depends linearly on N, while the total number of matrix entries grows quadratically with N. Thus, as we consider larger matrices, i.e., $N \to \infty$, the number of the non-zero values compared to the total matrix entries is diminished to zero. Based on this fact, we store the matrix A_2 in MATLAB [44] as a sparse matrix, keeping only the non-zero values and their positions. The resulting sparsity structure of the differentiation matrix A_2 is shown in Fig. 3.1.

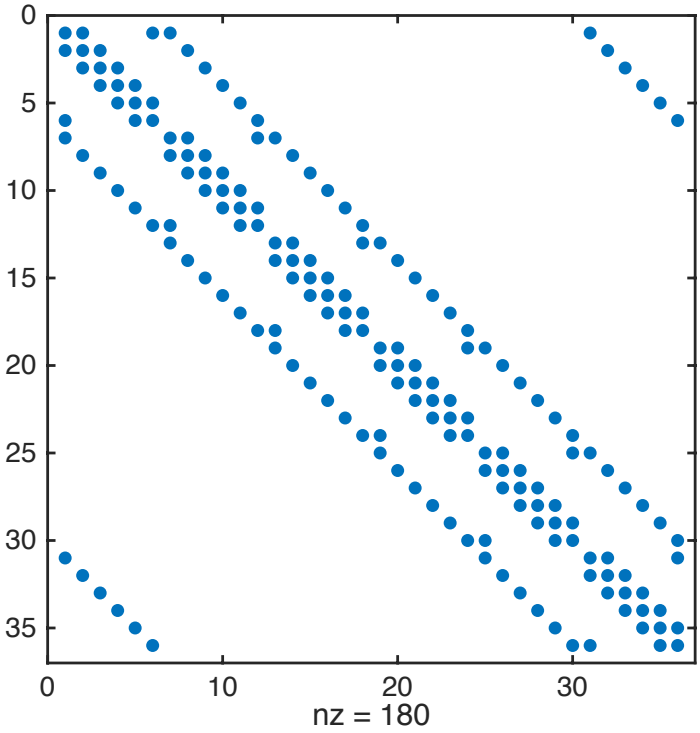

Figure 3.1: Sparsity pattern for the Laplace operator with a central difference scheme in both directions, with $N = 36$. The number of non-zero entries is $5N = 180$, while the number of the total matrix entries is $N \times N = 1296$.

Finally, the initial problem (3.1) can be solved using an implicit method. In particular, using an equidistant discretization with time step dt on the time interval [0,T] and a backward difference in time leads to the following linear system, which is necessary to solve in each iteration in MATLAB.

$$\frac{H^+ - H}{dt} = DA_2H^+ \Leftrightarrow SH^+ = H, \tag{3.9}$$

where $S = (I_N - dtDA_2)$, I_N is an $N \times N$ identity matrix and H^+ the updated solution in the new time step.

This scheme is always numerically stable and convergent -it does not require sat-

isfaction of the Courant-Friedrichs-Lewy (CFL) condition- with the order of error to be linear regarding the time step and quadratic with respect to the space step, [98]. Thus, we write

$$Error = O(dt) + O(dx^2). \tag{3.10}$$

3.2 Surface Evolution without Prestress

We wish to apply the finite difference method, developed previously, on the simplified partial differential equation (2.27), disregarding the term that accounts for the chemical potential and the effect of elastic prestress.

3.2.1 Formulation of the Model

Taking into account all the modifications that are suggested in section 5.2, about the coefficients D_1, D_2, D_3, the equation of surface evolution can be written in the following simpler form:

$$\frac{\partial h}{\partial t} = D_3 \nabla^2 h(\boldsymbol{x}) + D_2 \nabla^2 \nabla^2 h(\boldsymbol{x}), \tag{3.11}$$

where

$$D_3 = \frac{\Omega K d}{RT} \gamma. \tag{3.12}$$

Once the differentiation matrix A_2, which approximates the Laplace operator, is defined, the differentiation matrix A_4 for the bi-Laplacian operator can be defined as

$A_4 = A_2^2$, where its sparsity structure is shown in Fig. 3.2.

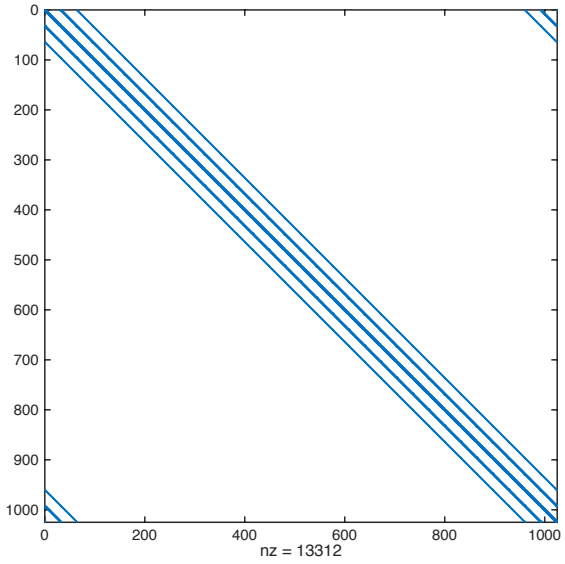

Figure 3.2: Sparsity pattern for the bi-Laplacian operator with a central difference scheme in both directions, with $N = 1024$. The number of non-zero entries is 13312, while the number of the total matrix entries is $N \times N = 1048576$.

Hence, we can consider the equation (3.11) in terms of the differentiation matrices A_2 and A_4 as follows:

$$H_t = D_3 A_2 H + D_2 A_4 H. \tag{3.13}$$

This can be transformed into a linear system, likewise as (3.9),

$$\frac{H^+ - H}{dt} = D_3 A_2 H^+ + D_2 A_4 H^+ \Leftrightarrow S H^+ = H, \tag{3.14}$$

with the only difference being that new matrix $S = (I_N - dt D_3 A_2 - dt D_2 A_4)$.

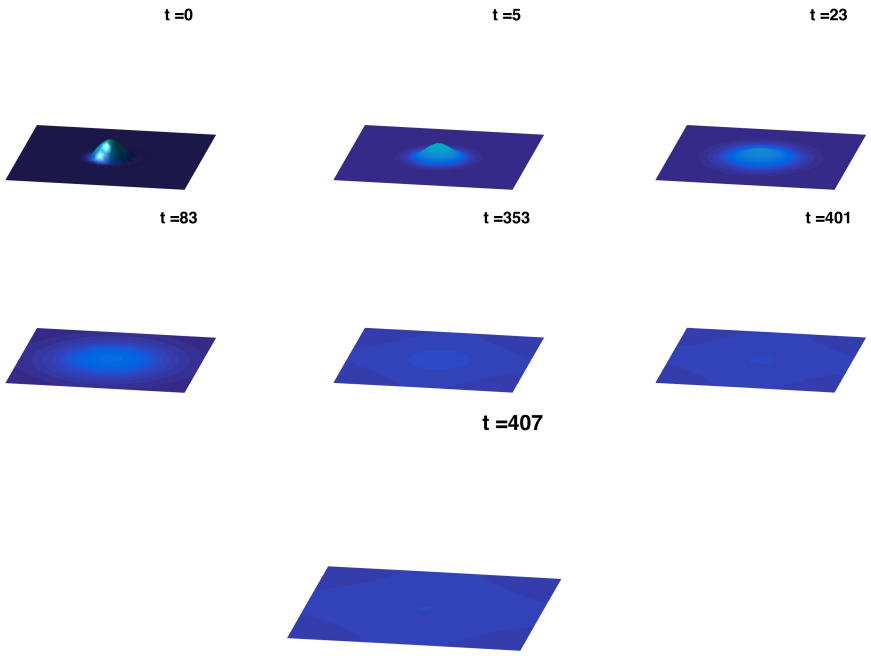

Figure 3.3: Evolution of the surface without the effect of elastic prestress.

3.2.2 Numerical Results - Visualization

Solving the above linear system (3.14) in MATLAB, by considering parameters that correspond to stable region as found in section 5.2, we observe the evolution of the surface, c.f., Fig. 3.3.

The initial condition was assumed to be in the following form:

$$h_0(x,y) = A\Big(cos(\frac{2\pi}{L}x) + cos(\frac{2\pi}{L}y)\Big), \tag{3.15}$$

where L is the space domain and A is the initial amplitude of the bump positioned only at the center of the domain. In addition, the input data that were used in the numerical code are summarized in the following table, Table 3.1.

Parameter, [unit]	**Value**
D_3 coefficient, $[m^2/sec]$	$D_3 = 2.4874 \cdot 10^{-14}$
D_2 coefficient, $[m^2/sec]$	$D_2 = \frac{D_3}{100}$
Time step, $[sec]$	$dt = 5$
Total time, $[sec]$	$T = 500$
Number of grid points, $(N = n^2)$	$n = 32$
Space domain, $[m]$	$L = 2\pi \cdot 10^{-6}$

Table 3.1: Input data that have been used in the numerical code to implement the finite difference method.

As it can be seen from Fig. 3.3, the surface tends to be completely planar after the time of $t^* = 407$ $[sec]$.

3.3 Surface Evolution with Prestress

We proceed by adding the effect of elastic prestress, i.e., uniaxial prestress $[\![\sigma^*_{11}]\!]$, to the equation of surface evolution.

3.3.1 Formulation of the Model

Taking into account the effect of elastic prestress, equation (2.27) becomes

$$\begin{aligned}\frac{\partial h}{\partial t} &= D_3\nabla^2 h(\boldsymbol{x}) + D_2\nabla^2\nabla^2 h(\boldsymbol{x}) \\ &\quad + \frac{\Omega K d}{RT}\int_{\mathbb{R}^2} G_{ik,\beta}(\boldsymbol{x}-\boldsymbol{x}')[\![\sigma^*_{i\beta}]\!][\![\sigma^*_{k\delta}]\!]h_{,\delta}\,(\boldsymbol{x}')\,d\boldsymbol{x}',\end{aligned} \tag{3.16}$$

or generally,

$$\frac{\partial h}{\partial t} = D_3\nabla^2 h(\boldsymbol{x}) + D_2\nabla^2\nabla^2 h(\boldsymbol{x}) + f(h). \tag{3.17}$$

Unfortunately, in this case we cannot directly apply the FDM as in previous cases, due to the integral term $f(h)$. Therefore, a recourse to the Fourier space is required.

More specifically, we have found that

$$\mathcal{F}[f(h)] = -\frac{\Omega K d}{RT}\hat{G}_{ik}(\boldsymbol{k})[\![\sigma^*_{i\beta}]\!]k_\beta[\![\sigma^*_{k\delta}]\!]k_\delta\hat{h}(\boldsymbol{k}), \tag{3.18}$$

where $\mathcal{F}$ denotes the Fourier transform.

The Green's function matrix, $\hat{G}_{ik}(\boldsymbol{k})$, has been numerically calculated, section 2.6, for a specific material system. Using the differentiation matrices defined before and taking the function f back in the physical domain by applying the inverse Fourier transform $\mathcal{F}^{-1}$ and considering only the real part of it, we can write

$$H_t = D_3A_2H + D_2A_4H - \frac{\Omega K d}{RT}\Re\big(\mathcal{F}^{-1}[\mathcal{F}[f(\hat{H})]]\big). \tag{3.19}$$

Finally we get the linear system

$$SH^+ = \Big(H - dt\frac{\Omega K d}{RT}\Re\big(\mathcal{F}^{-1}[\hat{G}_{ik}(\boldsymbol{k})[\![\sigma^*_{i\beta}]\!]k_\beta[\![\sigma^*_{k\delta}]\!]k_\delta\hat{H}(\boldsymbol{k})]\big)\Big), \tag{3.20}$$

with $S = (I_N - dtD_3A_2 - dtD_2A_4)$ as before, which we solve numerically. Note here that at each iteration the function f is defined in the previous time step.

3.3.2 Numerical Results - Visualization

Solving the linear system with exactly the same initial condition and numerical values for the parameters involved as before, section 3.2.2, we observe the evolution of the surface, including the effect of the elastic prestress, c.f., Fig. 3.4. The calculation

of the surface Green's function is based on the lithium-LIPON material system for initial wavenumber, $k = 2\pi$, in both in-plane directions, c.f., section 2.6.

For uniaxial prestress $[\![\sigma^*_{11}]\!] = 100\ [MPa]$ the surface tends to be completely planar after about $t^* = 87\ [sec]$. The larger the value of the applied prestress is, the less time it takes for the surface to become planar. Comparing this time with the one obtained in the absence of prestress ($t^* = 407\ [sec]$) we verify the fact that elastic prestress helps stabilizing the Li electrode-electrolyte interface in a manner that tends to keep it planar.

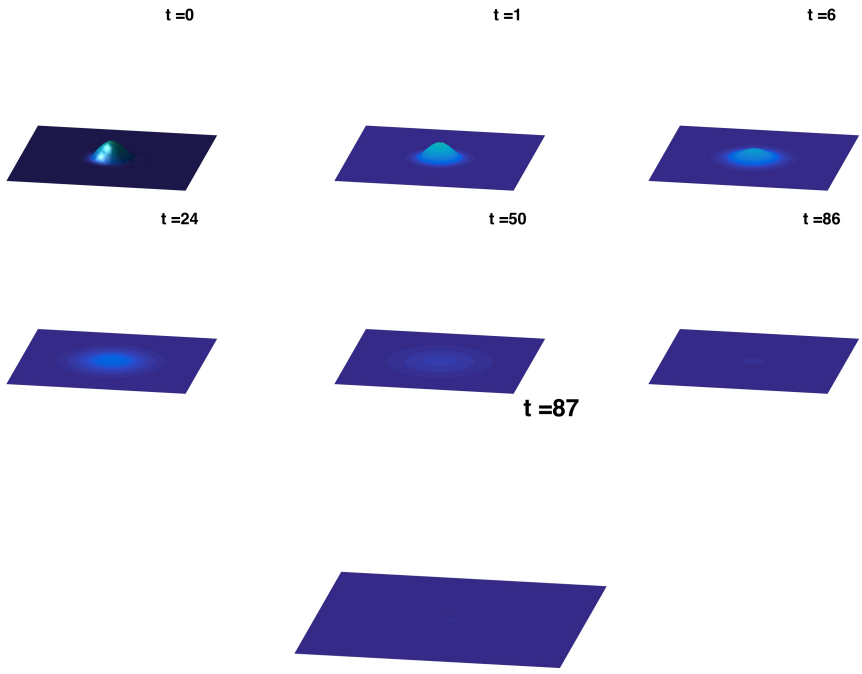

Figure 3.4: Evolution of the surface with the effect of elastic prestress, i.e., $[\![\sigma^*_{11}]\!] = 100$ $[MPa]$.

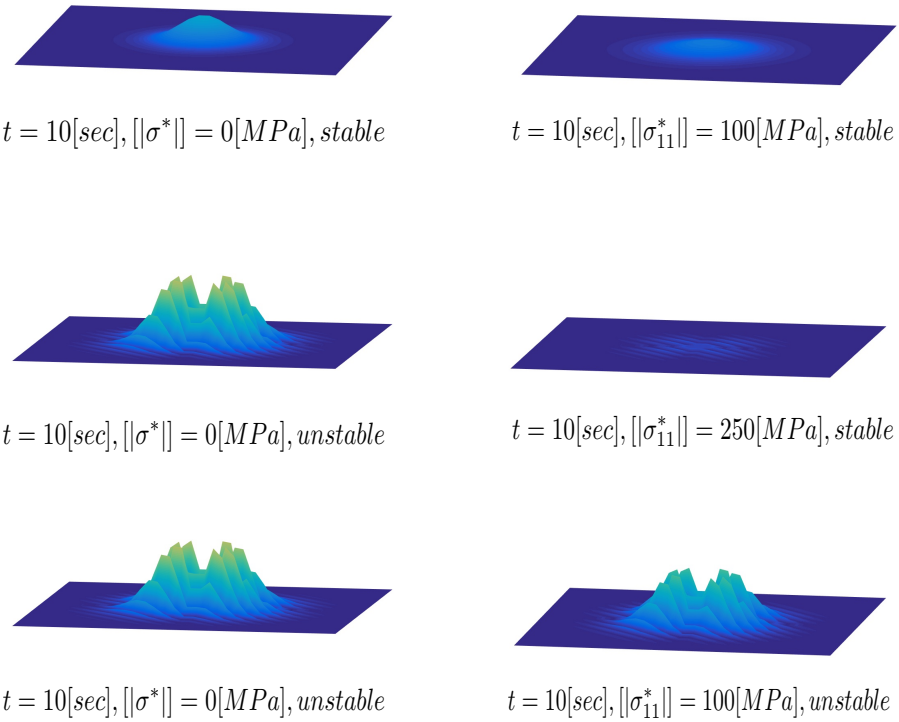

Figure 3.5: Surface profile at time $t = 10$ $[sec]$ for stable and unstable regime: stable without prestress (top left), stable with prestress ($[\![\sigma^*_{11}]\!] = 100$ $[MPa]$, top right), unstable without prestress (middle left), stable with prestress ($[\![\sigma^*_{11}]\!] = 250$ $[MPa]$, middle right), unstable without prestress (bottom left) and unstable with prestress ($[\![\sigma^*_{11}]\!] = 100$ $[MPa]$, bottom right).

3.4 Surface Evolution in Different Cases

So far, we studied the surface evolution for values of parameters that give stable perturbation i.e., the surface tends to become planar. In this section, we consider also parameters that result to instability and growth of the electrode-electrolyte interface (the only change in the input data is: $D_2 = D_3/30$). More specifically, we present the surface profile, c.f., Fig. 3.5, at the same time, $t = 10$ $[sec]$, for different cases: i) top: stable regime without the effect of prestress and with the effect of prestress ($[\![\sigma^*_{11}]\!] = 100$ $[MPa]$), ii) middle: unstable regime without the effect of prestress and

stable regime with the effect of prestress ($[\![\sigma_{11}^*]\!] = 250\ [MPa]$), iii) bottom: unstable regime without the effect of prestress and unstable regime with the effect of prestress ($[\![\sigma_{11}^*]\!] = 100\ [MPa]$). As depicted in the figure, for stable regime the surface with applied prestress tends to become planar sooner compared with the case where no prestress is applied. Also, depending on the value of the applied prestress the surface can grow and give unstable evolution or decay to a stable and planar condition.

3.5 Summary

Employing the theory of finite differences, we examined the surface evolution as a function of time. In particular, a backward time, central space finite difference scheme was used on the simplified equation that describes the evolution of the surface profile on a domain with periodic boundary conditions. The foundation of the theoretical work presented in this chapter lies in approximating derivatives, and more specifically the Laplace operator, with differentiation matrices and converting partial differential equations into a system of linear algebraic equations. Finally, numerical implementation of this theoretical formulation in MATLAB resulted in visualization of the surface for the cases of both zero and non-zero elastic prestress. The presence of elastic prestress was found to facilitate the stabilization of the Li electrode-electrolyte interface by keeping it planar. This finding is consistent with the results of Chapter 5.

Chapter 4

Elastic Energy Difference - Theoretical and Computational Study

The elastic energy difference with respect to the planar interface was obtained in Chapter 2. This derivation was based on the properties of the Fourier transform and the Green's function matrix, on a wavy profile in the two in-plane directions (k_1, k_2 the wavenumbers of the interfacial roughness). In this chapter, we specialize this analysis in a profile that is periodic in one direction, x_1, and constant in the other direction, x_2. In particular, we mathematically formulate an analytical expression for the dependence of the elastic energy difference per unit length on the surface Green's function and the stress jump created in the interface using the properties of Fourier series. Exploiting the periodicity of the domain, we focus our analysis on a single strip of one period of the waviness of the interface. We seek to validate this result by employing numerical simulations using a commercial finite element analysis software, Abaqus FEA [2]. Lastly, we present comparison results for the two approaches.

4.1 Mathematical Preliminaries

In this section, we present some basic concepts of the relation between Fourier series and integrals that are applicable to later sections, [19, 22, 84, 97].

We begin by defining the Fourier transform of a function $f : \mathbb{R}^n \to \mathbb{R}$ as follows:

$$\hat{f}(\boldsymbol{k}) = \int f(\boldsymbol{x}) \mathrm{e}^{-i\boldsymbol{k}\cdot\boldsymbol{x}}\, d\boldsymbol{x}, \tag{4.1}$$

with the inverse to be

$$f(\boldsymbol{x}) = \frac{1}{(2\pi)^n} \int \hat{f}(\boldsymbol{k}) \mathrm{e}^{i\boldsymbol{k}\cdot\boldsymbol{x}}\, d\boldsymbol{k}. \tag{4.2}$$

Suppose that $f(\boldsymbol{x})$ is periodic in the sense that

$$f(\boldsymbol{x} + \boldsymbol{x}(\boldsymbol{l})) = f(\boldsymbol{x}), \tag{4.3}$$

where $\boldsymbol{l} \in \mathbb{Z}^n$ and

$$\boldsymbol{x}(\boldsymbol{l}) = l^i \boldsymbol{c}_i \tag{4.4}$$

for vectors $(\boldsymbol{c}_i)_{i=1}^n$.

Taking advantage of the periodicity we can write,

$$\begin{aligned} \hat{f}(\boldsymbol{k}) &= \int_D f(\boldsymbol{x}) \left(\sum_{\boldsymbol{l}\in\mathbb{Z}^n} \mathrm{e}^{-i\boldsymbol{k}\cdot(\boldsymbol{x}+\boldsymbol{x}(\boldsymbol{l}))} \right) d\boldsymbol{x} \\ &= \left(\int_D f(\boldsymbol{x}) \mathrm{e}^{-i\boldsymbol{k}\cdot\boldsymbol{x}}\, d\boldsymbol{x} \right) \left(\sum_{\boldsymbol{l}\in\mathbb{Z}^n} \mathrm{e}^{-i\boldsymbol{k}\cdot\boldsymbol{x}(\boldsymbol{l})} \right) \\ &= \left(\int_D f(\boldsymbol{x}) \mathrm{e}^{-i\boldsymbol{k}\cdot\boldsymbol{x}}\, d\boldsymbol{x} \right) \left(\frac{(2\pi)^n}{|D|} \sum_{\boldsymbol{m}\in\mathbb{Z}^n} \delta(\boldsymbol{k} - \boldsymbol{k}(\boldsymbol{m})) \right), \end{aligned} \tag{4.5}$$

where D is some convenient periodic cell, e.g., $D = \{\boldsymbol{x} = x^i c_i,\ 0 \leq x^i \leq 1,\ i = 1, \ldots, n\}$ or the Wigner-Seitz cell of the lattice spanned by $(\boldsymbol{e}_i)_{i=1}^n$, $\boldsymbol{m} \in \mathbb{Z}^n$,

$$\boldsymbol{k}(\boldsymbol{m}) = m_i \boldsymbol{c}^i \tag{4.6}$$

and $\boldsymbol{c}^i \cdot \boldsymbol{c}_i = 2\pi$ is the reciprocal basis.

We note that

$$\hat{f}(\boldsymbol{k} + \boldsymbol{k}(\boldsymbol{m})) = \hat{f}(\boldsymbol{k}) \tag{4.7}$$

for every $\boldsymbol{m} \in \mathbb{Z}^n$, i.e., $\hat{f}(\boldsymbol{k})$ is periodic with periodicity defined by the reciprocal basis. Therefore, it suffices to define $\hat{f}(\boldsymbol{k})$ over the unit cell of the reciprocal lattice.

The inverse Fourier transform follows as

$$\begin{aligned} f(\boldsymbol{x}) &= \frac{1}{(2\pi)^n} \int \left(\int_D f(\boldsymbol{x}) \mathrm{e}^{-i\boldsymbol{k}\cdot\boldsymbol{x}}\, d\boldsymbol{x} \right) \left(\frac{(2\pi)^n}{|D|} \sum_{\boldsymbol{m}\in\mathbb{Z}^n} \delta(\boldsymbol{k} - \boldsymbol{k}(\boldsymbol{m})) \right) \mathrm{e}^{i\boldsymbol{k}\cdot\boldsymbol{x}}\, d\boldsymbol{k} \\ &= \sum_{\boldsymbol{m}\in\mathbb{Z}^n} \left(\frac{1}{|D|} \int_D f(\boldsymbol{x}) \mathrm{e}^{-i\boldsymbol{k}(\boldsymbol{m})\cdot\boldsymbol{x}}\, d\boldsymbol{x} \right) \mathrm{e}^{i\boldsymbol{k}(\boldsymbol{m})\cdot\boldsymbol{x}}, \end{aligned} \tag{4.8}$$

or

$$f(\boldsymbol{x}) = \sum_{\boldsymbol{m}\in\mathbb{Z}^n} f_{\boldsymbol{m}} \mathrm{e}^{i\boldsymbol{k}(\boldsymbol{m})\cdot\boldsymbol{x}}, \tag{4.9}$$

where

$$f_{\boldsymbol{m}} = \frac{1}{|D|} \int_D f(\boldsymbol{x}) \mathrm{e}^{-i\boldsymbol{k}(\boldsymbol{m})\cdot\boldsymbol{x}}\, d\boldsymbol{x} \tag{4.10}$$

are Fourier series coefficients. We see that $f(\boldsymbol{x})$ admits an equivalent representation as a Fourier series. In particular, in order to reconstruct $f(\boldsymbol{x})$ it suffices to know its Fourier series coefficients for all $\boldsymbol{m} \in \mathbb{Z}^n$.

For computational convenience, we can also use angle variables in place of wave numbers. To this end, we write

$$\theta^i = \boldsymbol{x} \cdot c^i, \tag{4.11}$$

with inverse

$$\boldsymbol{x} = \theta^i c_i, \tag{4.12}$$

so that

$$\boldsymbol{k}(\boldsymbol{m}) \cdot \boldsymbol{x} = \theta^i m_i. \tag{4.13}$$

In these variables,

$$f_{\boldsymbol{m}} = \int_{[-\pi,\pi]^n} f(\boldsymbol{\theta}) \mathrm{e}^{-i\boldsymbol{\theta}\cdot\boldsymbol{m}}\, d\boldsymbol{\theta}. \tag{4.14}$$

The advantage of this representation is that it standardizes the domain of integration for the computation of the Fourier series coefficients.

Let f and g be two D-periodic functions. Then,

$$\begin{aligned}
\int_D f(\boldsymbol{x}) g^*(\boldsymbol{x})\, d\boldsymbol{x} &= \int_D \left(\sum_{\boldsymbol{m}\in\mathbb{Z}^n} f_{\boldsymbol{m}} \mathrm{e}^{i\boldsymbol{k}(\boldsymbol{m})\cdot\boldsymbol{x}} \right) \left(\sum_{\boldsymbol{n}\in\mathbb{Z}^n} g^*_{\boldsymbol{n}} \mathrm{e}^{-i\boldsymbol{k}(\boldsymbol{n})\cdot\boldsymbol{x}} \right) d\boldsymbol{x} \\
&= \sum_{\boldsymbol{m}\in\mathbb{Z}^n} \sum_{\boldsymbol{n}\in\mathbb{Z}^n} f_{\boldsymbol{m}} g^*_{\boldsymbol{n}} \int_D \mathrm{e}^{i\boldsymbol{k}(\boldsymbol{m})\cdot\boldsymbol{x}} \mathrm{e}^{-i\boldsymbol{k}(\boldsymbol{n})\cdot\boldsymbol{x}}\, d\boldsymbol{x} \\
&= |D| \sum_{\boldsymbol{m}\in\mathbb{Z}^n} f_{\boldsymbol{m}} g^*_{\boldsymbol{m}}.
\end{aligned} \tag{4.15}$$

This identity specializes Parseval's theorem to the periodic case. Note that the asterisk " $*$ " as a superscript on the function, denotes its complex transpose.

Let f be D-periodic and g be a function over $\mathbb{R}^n$. Then

$$\begin{aligned}(f*g)(\boldsymbol{x}+\boldsymbol{x}(l)) &= \int g(\boldsymbol{x}+\boldsymbol{x}(\boldsymbol{l})-\boldsymbol{y})f(\boldsymbol{y})\,d\boldsymbol{y} = \int g(\boldsymbol{x}-\boldsymbol{z})f(\boldsymbol{z}+\boldsymbol{x}(\boldsymbol{l}))\,d\boldsymbol{z} \\ &= \int g(\boldsymbol{x}-\boldsymbol{z})f(\boldsymbol{z})\,d\boldsymbol{z} = (f*g)(\boldsymbol{x}),\end{aligned} \tag{4.16}$$

which shows that $f*g$ is also D-periodic.

Then, the corresponding Fourier series coefficients are

$$\begin{aligned}(f*g)_{\boldsymbol{m}} &= \frac{1}{|D|}\int_D (f*g)(\boldsymbol{x})\mathrm{e}^{-i\boldsymbol{x}\cdot\boldsymbol{k}(\boldsymbol{m})}\,d\boldsymbol{x} \\ &= \frac{1}{|D|}\int_D \left(\int g(\boldsymbol{x}-\boldsymbol{y})f(\boldsymbol{y})\,dy\right)\mathrm{e}^{-i\boldsymbol{k}(\boldsymbol{m})\cdot\boldsymbol{x}}\,d\boldsymbol{x} \\ &= \frac{1}{|D|}\int_D\int f(\boldsymbol{y})g(\boldsymbol{z})\mathrm{e}^{-i\boldsymbol{k}(\boldsymbol{m})\cdot(\boldsymbol{y}+\boldsymbol{z})}\,d\boldsymbol{y}\,d\boldsymbol{z} \\ &= \left(\frac{1}{|D|}\int_D f(\boldsymbol{y})\mathrm{e}^{-i\boldsymbol{k}(\boldsymbol{m})\cdot\boldsymbol{y}}\,d\boldsymbol{y}\right)\left(\int g(\boldsymbol{z})\mathrm{e}^{-i\boldsymbol{k}(\boldsymbol{m})\cdot\boldsymbol{z}}\,d\boldsymbol{z}\right) \\ &= f_{\boldsymbol{m}}\hat{g}(\boldsymbol{k}(\boldsymbol{m})),\end{aligned} \tag{4.17}$$

which specializes the convolution theorem to the periodic case.

4.2 Application to Interfacial Energies - Theoretical Study

We wish to derive an analytical expression of the elastic energy difference of the interface based on the properties of the Fourier series presented before. In doing so,

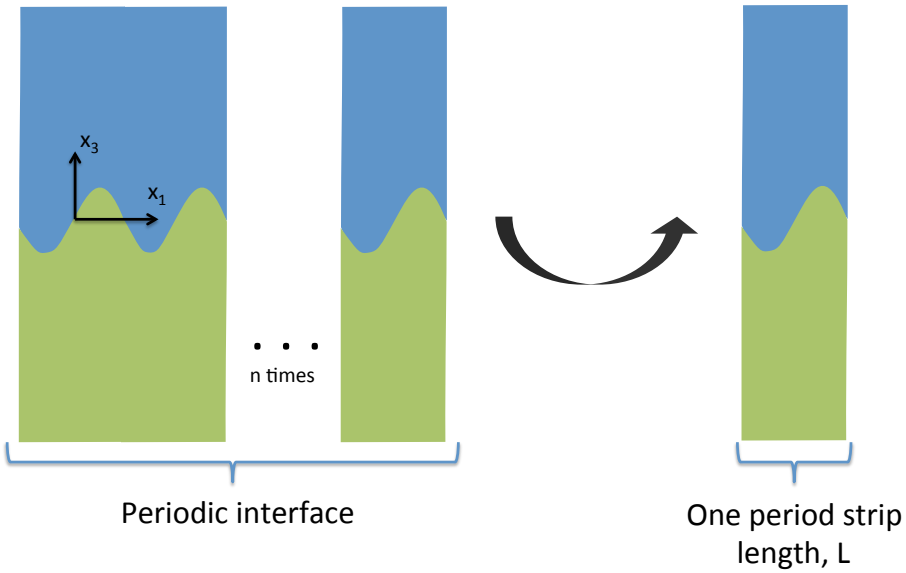

Figure 4.1: Periodic profile of the interface (left) and one period strip (right).

we consider a sinusoidal profile

$$x_3 = h(x_1) = A \sin\left(\frac{2\pi}{L} x_1\right) \tag{4.18}$$

that is periodic in the x_1-direction, with period L and amplitude A, and constant in the x_2-direction. In order to increase the computational efficiency we focus our study on an single strip of the whole geometry, with length L, i.e., one period of the waviness of the interface, c.f., Fig. 4.1.

By Clapeyron's theorem, the energy per unit length in the x_2-direction of one period in the x_1-direction is

$$E = \int_{-L/2}^{+L/2} \frac{1}{2} t_i(x_1) u_i(x_1, 0)\, dx_1. \tag{4.19}$$

In addition, we recall the relationship for the displacement from before

$$\begin{aligned} u_i(x_1,0) &= \int_{-\infty}^{+\infty}\int_{-\infty}^{+\infty} G_{ik}(x_1-x_1',x_2')t_k(x_1')dx_1'dx_2' \\ &= \int_{-\infty}^{+\infty} g_{ik}(x_1-x_1')t_k(x_1')dx_1' \\ &= (g_{ik}*t_k)(x_1) \end{aligned} \tag{4.20}$$

where

$$g_{ik}(x_1;x_1') = \int_{-\infty}^{+\infty} G_{ik}(x_1-x_1',x_2')dx_2' \tag{4.21}$$

and G_{ik} is the Green's function matrix.

Substituting this result back into equation (4.19), we get

$$E = \int_{-L/2}^{+L/2}\left(t_i(x_1)\int_{-\infty}^{+\infty}\frac{1}{2}g_{ik}(x_1-x_1')t_k(x_1')\,dx_1'\right)dx_1. \tag{4.22}$$

We can write equivalently in Fourier representation, as in equation (4.15), since both the traction and the displacement functions are periodic with period L,

$$E = L\sum_{m=-\infty}^{m=+\infty}\frac{1}{2}\hat{t}_i(m)\hat{u}_i^*(m), \tag{4.23}$$

where

$$\begin{aligned} \hat{t}_i(m) &= \frac{1}{L}\int_{-L/2}^{+L/2} t_i(x_1)\mathrm{e}^{-i(2\pi m/L)x_1}\,dx_1, \\ \hat{u}_i(m) &= \frac{1}{L}\int_{-L/2}^{+L/2} u_i(x_1)\mathrm{e}^{-i(2\pi m/L)x_1}\,dx_1 \end{aligned} \tag{4.24}$$

are Fourier series coefficients, accordingly to equation (4.10), for the traction and the

displacement, respectively.

In addition, taking advantage of the periodicity of the traction function, as in equation (4.17), we have

$$(g_{ik} * t_k)(m) = \hat{g}_{ik}(\frac{2\pi m}{L})\hat{t}_k(m). \tag{4.25}$$

Thus, equation (4.23) can be written as follows:

$$E = L\sum_{m=-\infty}^{m=+\infty} \frac{1}{2}\hat{g}_{ik}(\frac{2\pi m}{L})\hat{t}_i(m)\hat{t}_k^*(m). \tag{4.26}$$

Moreover, we know that

$$\hat{g}_{ik}(k_1) = \int_{-\infty}^{+\infty} g_{ik}(x_1)e^{-ik_1x_1}dx_1 = \int_{-\infty}^{+\infty}\int_{-\infty}^{+\infty} G_{ik}(x_1 - x_1', x_2)e^{-ik_1x_1}dx_1dx_2. \tag{4.27}$$

Since the profile is wavy in the x_1-direction and constant in the x_2-direction, we can write

$$\hat{G}_{ik}(k_1, k_2) = \int_{-\infty}^{+\infty}\int_{-\infty}^{+\infty} G_{ik}(x_1, x_2)e^{-i(k_1x_1+k_2x_2)}dx_1dx_2, \tag{4.28}$$

or,

$$\hat{G}_{ik}(k_1, 0) = \int_{-\infty}^{+\infty}\int_{-\infty}^{+\infty} G_{ik}(x_1, x_2)e^{-ik_1x_1}dx_1dx_2. \tag{4.29}$$

Finally, from equations (4.27) and (4.28) we can conclude that

$$\hat{g}_{ik}(k_1) = \hat{G}_{ik}(k_1, 0). \tag{4.30}$$

For a sinusoidal profile of amplitude A we have

$$t_i = [\![\sigma_{ij}]\!] n_j = [\![\sigma_{i1}]\!] h_{,1} + [\![\sigma_{i3}]\!] = [\![\sigma_{i1}]\!] A \frac{2\pi}{L} \cos \frac{2\pi x_1}{L} + [\![\sigma_{i3}]\!], \tag{4.31}$$

and finally, explicitly,

$$E = \frac{A^2 L}{8} \left(\frac{2\pi}{L} \right)^2 \hat{G}_{ik}(\frac{2\pi}{L}, 0) [\![\sigma_{i1}]\!] [\![\sigma_{k1}]\!]. \tag{4.32}$$

Note here that

$$\begin{aligned} &\int_{-L/2}^{+L/2} cos(2\pi x_1/L) \mathrm{e}^{-i(2\pi x_1/L)} \, dx_1 = \frac{L}{2}, \\ &\int_{-L/2}^{+L/2} \mathrm{e}^{-i(2\pi x_1/L)} \, dx_1 = 0. \end{aligned} \tag{4.33}$$

Equation (4.32) can be further simplified in our case, in the final form

$$E = \frac{A^2 L}{8} \left(\frac{2\pi}{L} \right)^2 \hat{G}_{11}(\frac{2\pi}{L}, 0) [\![\sigma_{11}]\!]^2, \tag{4.34}$$

which results to the dependence of the excess of the elastic strain energy per unit length in the x_2-direction on geometrical parameters, on the surface Green's function and lastly, on the interfacial jump stress. Note here that the stress jump is the one defined for the planar interface, and it is independent of position since the analytical result is a linear perturbation result, so the stress jump is defined on the unperturbed configuration.

The corresponding geometrical and material parameters of the single strip are

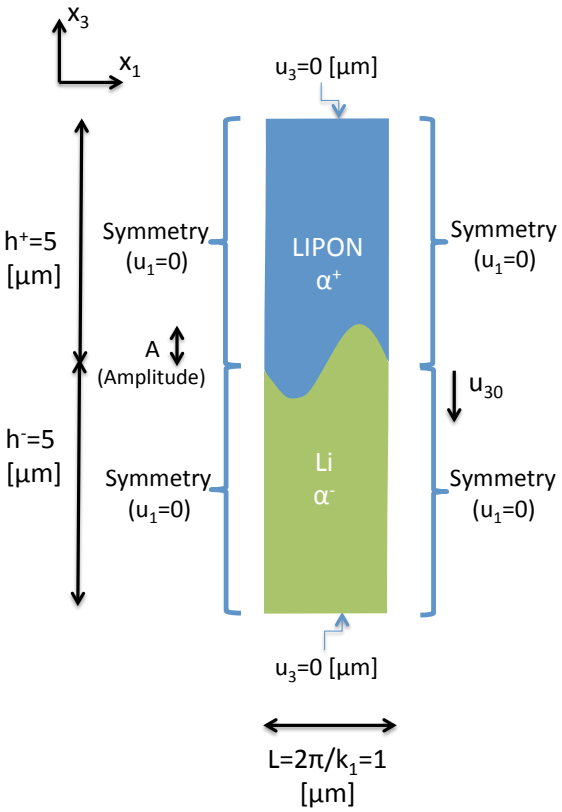

- Li: Cubic (bcc) ; LIPON: Isotropic
- Thermal Expansion Coefficients (α^+, α^-)

	Li	LIPON
Elastic properties [GPa]	$c_{11}^- = 13.5$ $c_{12}^- = 11.44$ $c_{44}^- = 8.78$	$c_{11}^+ = 103.6$ $c_{12}^+ = 44.42$ $c_{44}^+ = 29.61$
Wavenummbers [μm^{-1}]	$k_1 = 2\pi$	$k_2 = 0$
Thermal expansion Coefficient [θ^{-1}]	$\alpha^- = 4.6 \cdot 10^{-5}$	$\alpha^+ = 7 \cdot 10^{-5}$

Figure 4.2: Geometrical and material parameters of the single strip.

summarized in Figure 4.2. The interfacial jump in the stress component is created through thermal expansion. In particular, the two materials have different thermal expansion coefficients and this results in different stress fields. In addition, we constrain the vertical motion on the top and on the bottom surfaces, while in the lateral ones in both material regions we apply periodic boundary conditions and we constrain the horizontal motion. This thermal linear-elastic problem will be solved analytically for the case of a planar interface later in section 4.4.1.

4.3 Computational Study

We seek to validate this analytical formulation with a computational approach employing the finite element method.

4.3.1 General Concepts on FEM

From a mathematical perspective, a finite element method (FEM) is a numerical method to solve boundary value problems which consist of partial differential equations with an appropriate set of boundary conditions equations. The general concept is to divide the whole geometry of the body into simpler parts called finite elements, and then formulate and solve the discrete problem that comes from the weak form of the differential equations and which is equivalent to the governing equation and the boundary conditions. As proved in the literature [38,51,91], in linear-elastic problems the strong form and the weak form are identical.

To define the weak form we need to characterize two classes of functions: i) the trial solution $\boldsymbol{u}$, which satisfies the displacement boundary conditions, and ii) the weight function $\boldsymbol{w}$, which vanishes on the displacement boundary conditions.

In general, the mathematical formulation starts by forming the nodal displacement vector, $\boldsymbol{d}$, that consists of the components of the global displacements of the nodes. For instance in a 2D problem with n nodes we have

$$\boldsymbol{d} = [u_{x1} \quad u_{y1} \quad u_{x2} \quad u_{y2} \quad ... \quad u_{xn} \quad u_{yn}]^T. \tag{4.35}$$

The element nodal displacements, $\boldsymbol{d}^e$ and the element nodal values of the weight functions, $\boldsymbol{w}^e$, are given by

$$\begin{aligned} \boldsymbol{d}^e &= \boldsymbol{L}^e \boldsymbol{d}, \\ \boldsymbol{w}^{eT} &= \boldsymbol{w}^T \boldsymbol{L}^{eT}, \end{aligned} \tag{4.36}$$

where $\boldsymbol{L}^e$ are called the gather matrices, since they gather the nodal displacements of each element from the global matrix, relating element quantities to global matrices. They consist of ones and zeros.

The approximation of the trial solution and the weight function on each element are then as follows:

$$\begin{aligned} \boldsymbol{u}(x,y) &\approx \boldsymbol{u}^e(x,y) = \boldsymbol{N}^e(x,y)\boldsymbol{d}^e, \\ \boldsymbol{w}(x,y)^T &\approx \boldsymbol{w}^e(x,y)^T = \boldsymbol{w}^{eT}\boldsymbol{N}^e(x,y)^T, \end{aligned} \tag{4.37}$$

where $\boldsymbol{N}^e$ are the element shape function matrix. The shape functions interpolate the solution between the discrete values that were found at the nodes. Usually, they are low order polynomials (linear, quadratic, cubic) and depend on the type of element used and the number of nodes.

Having obtained the displacement field we can compute the strains from the strain displacement relationships in the form

$$\boldsymbol{\epsilon}^e = \boldsymbol{B}^e \boldsymbol{d}^e, \tag{4.38}$$

where $\boldsymbol{B}^e$ is the strain-displacement matrix, computed by taking the gradient of the shape function matrix. The stress field then follows from the constitutive law

$$\boldsymbol{\sigma}^e = \boldsymbol{D}^e \boldsymbol{\epsilon}^e, \tag{4.39}$$

where $\boldsymbol{D}^e$ is the material stiffness tensor.

Finally, through application of the principle of virtual work, in a domain Ω with boundary Γ, the weak form of the differential equations can be written as

$$\boldsymbol{w}^T \left[\left(\sum_{e=1}^{n_{el}} \boldsymbol{L}^{eT} \boldsymbol{K}^e \boldsymbol{L}^e \right) \boldsymbol{d} - \left(\sum_{e=1}^{n_{el}} \boldsymbol{L}^{eT} \boldsymbol{f}^e \right) \right] = 0 \quad \forall \boldsymbol{w}, \tag{4.40}$$

where n_{el} is the total number of elements of the problem and $\boldsymbol{K}^e$ and $\boldsymbol{f}^e$ are the element stiffness matrix and element external force matrix, respectively, defined as follows:

$$\begin{aligned} \boldsymbol{K}^e &= \int_{\Omega^e} \boldsymbol{B}^{eT} \boldsymbol{D}^e \boldsymbol{B}^e d\Omega, \\ \boldsymbol{f}^e &= \int_{\Omega^e} \boldsymbol{N}^{eT} \boldsymbol{b} d\Omega + \int_{\Gamma_t^e} \boldsymbol{N}^{eT} \boldsymbol{t} d\Gamma, \end{aligned} \tag{4.41}$$

where Γ_t is the boundary on which traction $\boldsymbol{t}$ is applied and the vector $\boldsymbol{b}$ is the body forces.

4.3.2 Model Formulation

In order to validate the analytical formula obtained for the elastic energy difference of the single strip, equation (4.34), we performed numerical simulations using a finite

element software, [2]. In particular, a static linear-elastic analysis under plane strain conditions is used to solve this mechanical 2D FEM problem, which is valid for small deformations and linear relationships between the stress and strain components [100, 101]. This analysis also includes temperature effects, inducing thermal expansion of the two materials and build-in the stress field.

We start by defining the geometry of the model and progress by assigning material properties and thermal expansion coefficients for both regions (lithium-LIPON). For simplicity, isotropic thermal expansion is assumed, and thus one thermal expansion coefficient per region is defined. The interface between the two materials is created using "partition" of the geometry and, in the case of the wavy interface, nodal points that approximate a sinusoidal profile are defined. All the geometrical and material parameters are shown in Figure 4.2. The boundary conditions are applied, c.f., Fig. 4.3, exactly as explained in the analytical formulation, section 4.2. Finally, the mesh and the element type are specified and the problem is fully defined and ready to be solved.

A list that describes the steps followed to define the FEM problem is as follows:

- Construct the geometry of the model (part)
- Assign material properties and select the constitutive law
- Apply boundary conditions (displacement, tractions)
- Discretize the domain (mesh the geometry)
- Solve the FEM problem and present the results

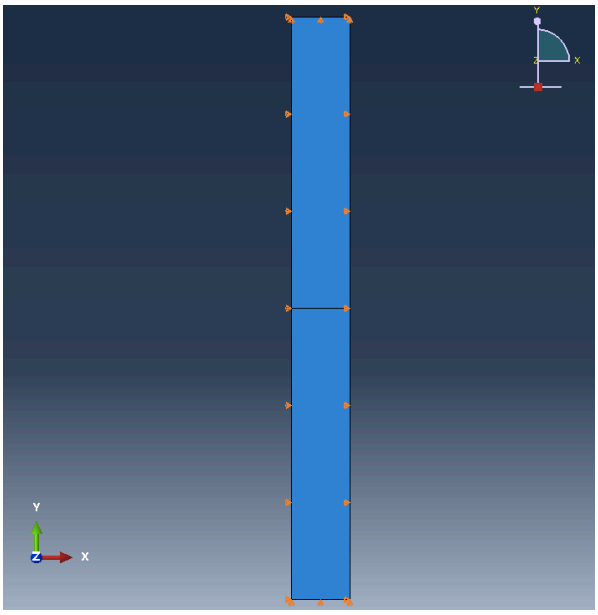

Figure 4.3: Geometry of the model and the boundary conditions applied in Abaqus FEA for the case of a planar interface.

The structure is modeled using a mix of an 8-node biquadratic plane strain quadrilateral (CPE8) and a 6-node quadratic plane strain triangle (CPE6) elements. This mixed choice of elements is used only in discretizing the geometry in proximity to the wavy interface and found not to affect the numerical convergence of the results. In addition, quadratic elements provide better numerical accuracy, reducing the computational error compared to linear elements [38, 51]. Numerical convergence of the results is achieved on the first trial by the original mesh of the software, since the computational cost of these simulations is low (0.4 CPU [*sec*]). However, once a convergence is assured, the mesh is optimized by lowering the mesh density in areas away from the interface where the values of stress are low. The level of accuracy in the calculations remained the same, while the computational time is reduced in the case of the optimized mesh. In Fig. 4.4 details on the number of nodes and elements are

presented for both the original and optimized mesh in the exemplary case of a wavy interface with amplitude $A = 0.05$ $[\mu m]$.

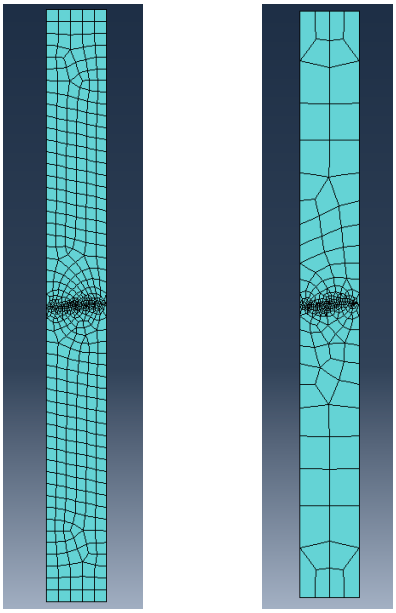

Figure 4.4: Exemplary mesh grid for the case of a wavy interface with amplitude $A = 0.05$ $[\mu m]$. The original mesh (left) consists of 1784 nodes and 563 elements and the optimized mesh (right) consists of 1011 nodes and 326 elements.

Abaqus FEA uses Newton's method to solve for the displacement field by obtaining the nodal displacement vector $\boldsymbol{d}$ from equation (4.40) after the stiffness and external force matrices are defined in equation (4.41). Then the strain and the stress fields are computed from the displacement field through the strain-displacement matrix $\boldsymbol{B}$ and the constitutive law (stiffness tensor $\boldsymbol{D}$). Finally, the elastic strain energy is computed as

$$E = \int_V \frac{1}{2}\sigma_{ij}\epsilon_{ij}dV. \tag{4.42}$$

To compute numerically the excess of the energy between the planar and the wavy interface, we subtract the amount of the energy for the model with the wavy interface

from the energy of the one with the planar interface and then we compare this result with the analytical formula in section 4.4.2.

4.4 Comparison Results

The analytical and numerical formulations of the model were established in the previous sections. Comparison results between the two approaches are presented and critically evaluated in this section. Firstly, the thermal linear-elastic problem is solved analytically in the case of a planar interface and the displacement, strain, and stress fields are determined and also verified numerically in Abaqus FEA in section 4.4.1. In addition, comparison results on the excess of the elastic energy as a function of the amplitude of the surface waviness are presented in section 4.4.2.

4.4.1 Analytical Solution for the Planar Interface

In the case of an unperturbed interface, the thermal linear-elastic problem can be solved analytically. In what follows, we denote with (+) the region of LIPON material and with (-) the lithium one.

In general, from Hooke's constitutive law, assuming isotropic thermal expansion, we have

$$\sigma_{ij}^{\pm} = c_{ijkl}^{\pm}(\epsilon_{kl}^{\pm} - \alpha^{\pm}\Delta T\delta_{kl}). \tag{4.43}$$

In this plane strain problem the only non-zero strain component is in the x_3-

direction, i.e., ϵ_{33}. Thus we write for the two regions,

$$\epsilon_{33}^{+} = \frac{u_{30}}{h^{+}}, \qquad \epsilon_{33}^{-} = \frac{-u_{30}}{h^{-}}, \tag{4.44}$$

where $h^{+} = h^{-} = h = H/2 = 5\ [\mu m]$ is the height of each region and u_{30} is the displacement of the planar interface. We expect the LIPON material with bigger thermal expansion coefficient ($\alpha^{+} = 7 \cdot 10^{-5}\ [\theta^{-1}]$) to expand more compared to lithium ($\alpha^{-} = 4.6 \cdot 10^{-5}\ [\theta^{-1}]$) and therefore we assign, from the beginning, the direction of u_{30} to pointing downwards, c.f., Fig. 4.2.

In addition, the matching condition for the traction across the interface requires that

$$\sigma_{33}^{+} = \sigma_{33}^{-} \tag{4.45}$$

or,

$$c_{11}^{+}\epsilon_{33}^{+} - \big(c_{11}^{+} + 2c_{12}^{+}\big)\alpha^{+}\Delta T = c_{11}^{-}\epsilon_{33}^{-} - \big(c_{11}^{-} + 2c_{12}^{-}\big)\alpha^{-}\Delta T. \tag{4.46}$$

From equations (4.44) and (4.46) we can solve for the displacement in the interface

$$u_{30} = h\Delta T \frac{\big(c_{11}^{+} + 2c_{12}^{+}\big)\alpha^{+} - \big(c_{11}^{-} + 2c_{12}^{-}\big)\alpha^{-}}{c_{11}^{+} + c_{11}^{-}} \tag{4.47}$$

and then define the strain field from equation (4.44). Regarding the stress components, in the x_1-direction we have

$$\sigma_{11}^{\pm} = c_{12}^{\pm}\epsilon_{33}^{\pm} - \big(c_{11}^{\pm} + 2c_{12}^{\pm}\big)\alpha^{\pm}\Delta T. \tag{4.48}$$

Using the material parameters mentioned before, c.f., Fig. 4.2 and applied change in temperature, $\Delta T = 100\ [\theta]$, we can solve analytically for the displacement, strain and stress fields. All these calculations are also verified numerically, in Abaqus FEA. The displacement and strain fields are shown in Figure 4.5 while the stress component in the x_1-direction is shown in Figure 4.6. For the analytical solution we have

$$u_{30} = 5.037284 \cdot 10^{-2}[\mu m], \tag{4.49}$$

$$\epsilon_{33}^{+} = 1.077456 \cdot 10^{-2}, \qquad \epsilon_{33}^{-} = -1.077456 \cdot 10^{-2}, \tag{4.50}$$

$$\sigma_{11}^{+} = -8.995676 \cdot 10^{-4}[N/\mu m^2], \qquad \sigma_{11}^{-} = -2.82601 \cdot 10^{-4}[N/\mu m^2]. \tag{4.51}$$

Thus, the jump in the stress that is used in the analytical formula for the excess of the energy defined before, c.f., equation (4.34), can be calculated as

$$[\![\sigma_{11}]\!] = \sigma_{11}^{+} - \sigma_{11}^{-} = -6.169665 \cdot 10^{-4}[N/\mu m^2]. \tag{4.52}$$

The elastic strain energy for the case of a planar interface is given by

$$\int_V \frac{1}{2}\sigma_{ij}\epsilon_{ij}dV = \frac{V}{2}\Big(\sigma_{33}^{+}\epsilon_{33}^{+} - \alpha^{+}\Delta T\big(\sigma_{11}^{+} + \sigma_{22}^{+} + \sigma_{33}^{+}\big) + \sigma_{33}^{-}\epsilon_{33}^{-} - \alpha^{-}\Delta T\big(\sigma_{11}^{-} + \sigma_{22}^{-} + \sigma_{33}^{-}\big)\Big), \tag{4.53}$$

where $V = h * L * w$ is the volume of each region and w the thickness of the strip and finally the strain energy per unit length, in the x_2 direction, is calculated as

$$E = 4.678197 \cdot 10^{-5}[J/\mu m]. \tag{4.54}$$

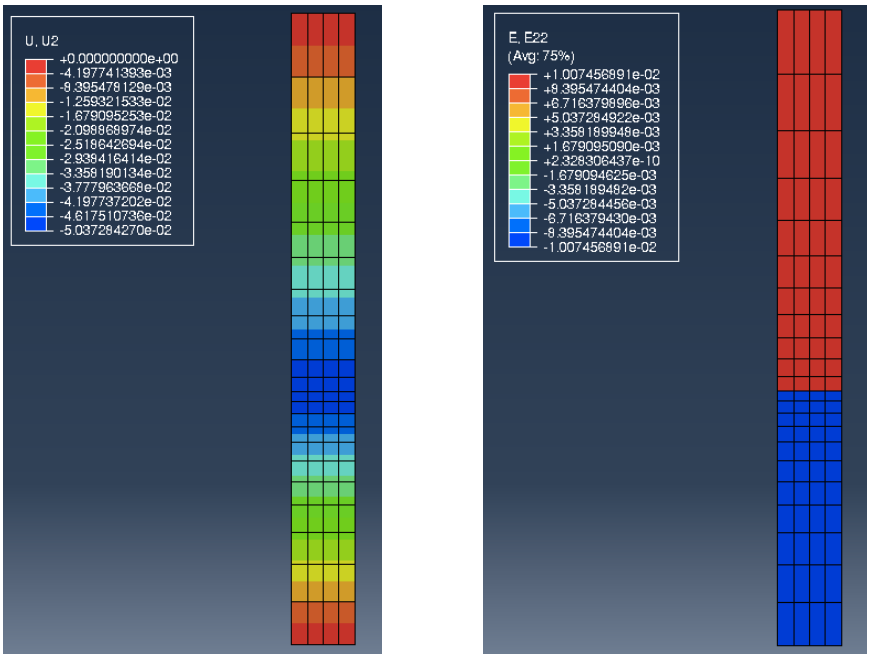

Figure 4.5: Abaqus FEA results on the displacement component, u_3 (left) and the strain component, ϵ_{33} (right), in the case of a planar interface. Mesh consists of 317 nodes and 88 quadrilateral elements of type CPE8. Note here that the x_2-direction in Abaqus FEA corresponds to the x_3-direction in the analytical solution developed previously.

4.4.2 Comparison Results on the Elastic Energy

The analytical elastic strain energy per unit length, in the x_2-direction, is calculated from equation (4.34). This expression shows quadratic dependence of the energy on the amplitude, A, of the perturbation. In the numerical simulations, using Abaqus FEA, we subtract the wavy energy from the energy of the planar interface to compute the excess of the energy for some exemplary values of the amplitude, ranging from $A = 0.0001 \sim 0.05$ $[\mu m]$. Note that the analytical results are based on linear perturbation analysis, so they should match the numerical results for very small amplitudes, i.e., $A/L \sim 0.01$.

The excess of the energy, calculated both analytically and numerically, is then

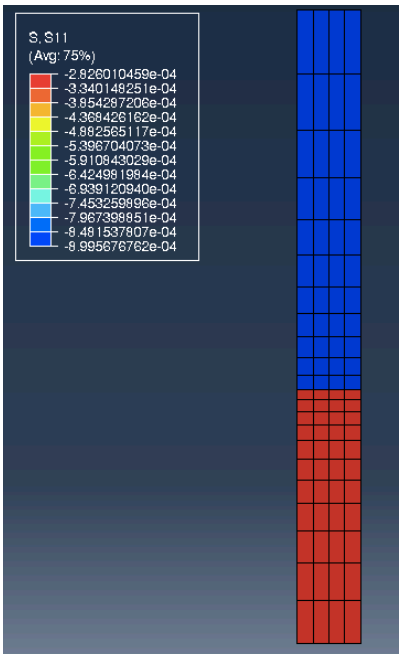

Figure 4.6: Abaqus FEA results on the stress component, σ_{11}, in the case of a planar interface. Mesh consists of 317 nodes and 88 quadrilateral elements of type CPE8.

plotted as a function of the amplitude times the wavenumber of the perturbation (to make it dimensionless), c.f., Fig. 4.7. In addition, the actual values of the energy for these specific values of the amplitude are presented in Figure 4.8. As shown from these results, the analytical formula of the elastic energy is in complete agreement with the numerical simulations. Therefore, we can safely conclude that it can be utilized in the stability analysis performed to examine dendrite formation on the lithium-LIPON interface.

4.5 Summary

The elastic energy difference with respect to the planar interface was derived analytically and validated using numerical simulations performed in a commercial finite

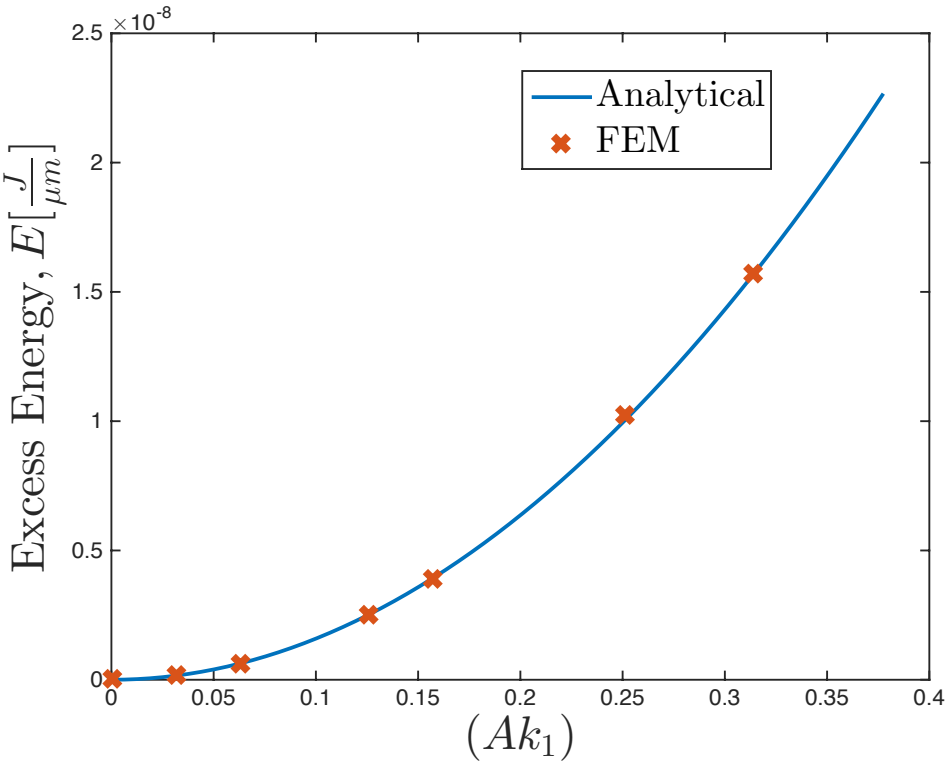

Figure 4.7: Comparison plot of the excess of the elastic energy, calculated analytically and numerically (FEM), as a function of the normalized amplitude of the perturbation.

Amplitude [μm]	Energy Analytical [J/μm]	Energy Planar [J/μm]	Energy Wavy [J/μm]	Energy Abaqus FEA [J/μm]	Ratio
0.0001	6.27962516171833•10^-14	4.67819781643044•10^-5	4.67819781018174•10^-5	6.2487002876720•10^-14	0.995
0.005	1.56990629042958•10^-10		4.67818217189386•10^-5	1.5644536580377•10^-10	0.997
0.01	6.27962516171833•10^-10		4.67813533816094•10^-5	6.2478269500149•10^-10	0.995
0.02	2.51185006468733•10^-9		4.67794943377705•10^-5	2.4838265339018•10^-9	0.989
0.025	3.92476572607395•10^-9		4.67781148785562•10^-5	3.8632857482052•10^-9	0.984
0.04	1.00474002587493•10^-8		4.67717197818177•10^-5	1.0258382486700•10^-8	1.021
0.05	1.56990629042958•10^-8		4.6766243291254•10^-5	1.5734873050500•10^-8	1.002

Figure 4.8: Numerical comparison results on the excess of the elastic strain energy between the analytical and the numerical simulations. **Amplitude**: amplitude of the perturbation on the wavy interface; **Energy Analytical**: analytical excess of the energy calculated from equation (4.34); **Energy Planar**: energy of the planar interface; **Energy Wavy**: energy of the wavy interface (Abaqus FEA); **Energy Abaqus FEA**: numerical excess of the energy (Energy Planar-Energy Wavy); **Ratio**: ratio of the numerical over the analytical energy.

element software, Abaqus FEA. Based on Fourier series properties and their relations with integrals, we formulated an analytical expression for the elastic energy. Moreover, it was found that the change of the elastic energy with respect to the planar interface depends on the amplitude and wavenumber of the perturbation, the surface Green's function and the interfacial stress jump. A finite element analysis was performed in order to support the analytical results. This specific, thermal linear-elastic 2D problem was modeled in Abaqus FEA under plane strain conditions. The analytical and numerical results are found to be in excellent agreement. Therefore, we can safely draw the conclusion that this analytical theory, predicting the change of the elastic energy, can be utilized in the stability analysis, which is performed in Chapter 5 as an avenue to understand dendrite formation.

Chapter 5

Stability Analysis - Parametric Study

In this chapter, we examine the conditions which affect the growth of an initially planar lithium-electrode interface. We base our study on a stability analysis that is performed in the adapted equation of surface evolution, obtained in the Chapter 2. This analysis results in explicit analytical expressions for the dependence of the critical unstable wavelength of the interfacial roughness on elastic prestress and on other fundamental parameters. Then, a parametric study is performed for a specific material system, in order to elucidate the importance of such parameters, and more specifically to quantify the effect of elastic prestress on interfacial growth.

5.1 Stability Analysis

Within the framework developed in the preceding sections, the formation of dendrites may be understood as the result of a loss of stability of flat interface. This instability is amenable to a simple linear analysis.

We proceed by considering a planar interface, c.f., Fig. 5.1, moving at constant

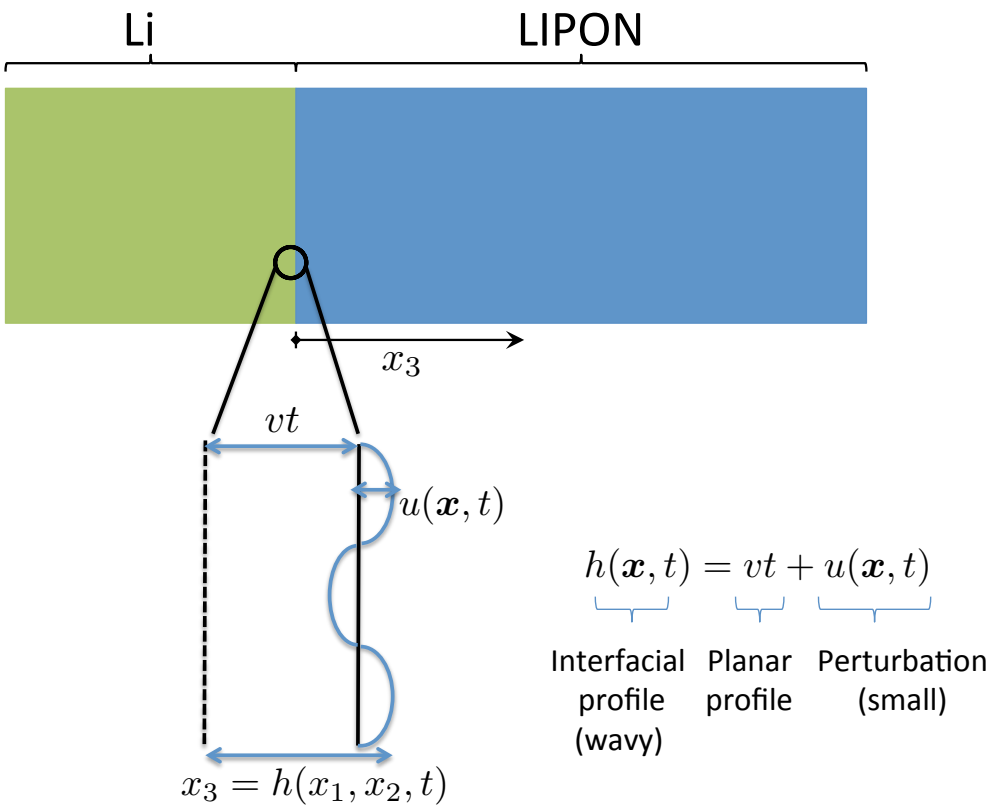

Figure 5.1: Small perturbation on the planar moving interface. Representation of the initial planar interface (black dashed line), the moving planar interface (black solid line) and the wavy interface (blue solid line).

speed v, i.e.,

$$h(x_1, x_2, t) = vt. \tag{5.1}$$

We change to a moving reference frame attached to the interface. For simplicity, we begin by neglecting the coupling to the electrostatic field, swelling, pressure-assisted diffusion and the Maxwell stress. Under these assumptions, we identify the reference interfacial profile with the planar profile (5.1) and write

$$h(\boldsymbol{x}, t) = vt + u(\boldsymbol{x}, t), \tag{5.2}$$

where the deviation u from flatness is presumed to be small, c.f., Fig. 5.1. Inserting this representation into (2.27) gives

$$\begin{aligned}\frac{\partial u}{\partial t} &= \nabla^2(D_1 u(\boldsymbol{x}) + D_2 \nabla^2 u(\boldsymbol{x})) \\ &\quad + \frac{\Omega K d}{RT}\left(\gamma \nabla^2 u(\boldsymbol{x}) + \int_{\mathbb{R}^2} G_{ik,\beta}(\boldsymbol{x}-\boldsymbol{x}')[\![\sigma^*_{i\beta}]\!][\![\sigma^*_{k\delta}]\!] u_{,\delta}\,(\boldsymbol{x}')\,d\boldsymbol{x}'\right).\end{aligned} \tag{5.3}$$

Inserting the *ansatz*

$$u(\boldsymbol{x},t) = A\mathrm{e}^{-\lambda t}\mathrm{e}^{-i\boldsymbol{k}\cdot\boldsymbol{x}} \tag{5.4}$$

into (5.3) gives the characteristic equation

$$\lambda(\boldsymbol{k}) = (D_1 + D_3)|\boldsymbol{k}|^2 - D_2|\boldsymbol{k}|^4 + \frac{\Omega K d}{RT}\hat{G}_{ik}(\boldsymbol{k})[\![\sigma^*_{i\beta}]\!]k_\beta[\![\sigma^*_{k\delta}]\!]k_\delta, \tag{5.5}$$

where $\boldsymbol{k}$ is the wavenumber vector of the perturbation, $\hat{G}_{ik}(\boldsymbol{k})$ is the Fourier transform of the surface Green's function (c.f., section 2.6 for a derivation),

$$D_3 = \frac{\Omega K d}{RT}\gamma \tag{5.6}$$

and $\lambda > 0$ (respectively $\lambda < 0$) corresponds to decay (respectively growth) of the perturbation.

We note that the elastic prestress contributes a positive number to the characteristic equation (5.5) and, therefore, it has a stabilizing effect on the electrode-electrolyte interface, i.e., it tends to keep it planar. We also note that the term contributed by the elastic prestress to the characteristic equation (5.5) is quadratic in the prestress.

Therefore, the electrode-electrolyte interface can be stabilized over an arbitrary range of wavenumbers by choosing the prestress large enough.

5.2 Parametric Study

In the previous section 5.1, it has been shown that the elastic prestress tends to increase the stability region of the interface by increasing the critical wavenumber for instability. In addition, some other parameters are also involved in the calculation of the critical wavenumber, such as the surface diffusivities D_1, D_2, the interfacial surface energy γ, and the kinetic rate coefficient K through the D_3 coefficient. We wish to estimate the effect of such parameters and leverage them in a way that will contribute to a planar evolution of the interface. As an avenue, a parametric study is performed in an actual material system consisting of lithium-LIPON as the electrode-electrolyte material.

In the absence of elastic prestress, i.e., $\sigma_{ij}^{*} = 0$, the planar interface is stable for a sufficiently small wavenumber, $|\boldsymbol{k}|$, but loses stability when

$$(D_1 + D_3)|\boldsymbol{k}|^2 - D_2|\boldsymbol{k}|^4 = 0. \tag{5.7}$$

The contribution of the elastic prestress will be considered later on.

We start by defining the D_3 coefficient for the actual lithium-LIPON material

system. Firstly, the kinetic rate coefficient is calculated through the equation

$$K = \frac{i_0 \Omega}{dF}, \tag{5.8}$$

where the value for the exchange current density, i_0, was taken from the work of [70]. The value for the partial molar volume of ion dissolved in the solid electrolyte, Ω, was suggested by the Bosch team (Robert Bosch GmbH, Stuttgart Germany) and the interfacial surface energy, γ, was calculated by atomistic calculations (William A. Goddard research group). Finally, the D_3 coefficient is calculated from equation (5.6). All the values involved in the calculation can be found in Table 5.1.

Parameter, [unit]	**Value**
Interfacial surface energy, $[J/m^2]$	$\gamma = 0.536$
Partial molar volume, $[m^3/mol]$	$\Omega = \frac{1}{1500}$
Exchange current density, $[A/m^2]$	$i_0 = 30$
Atomic interplanar distance, $[m]$	$d = 3.49 \cdot 10^{-10}$
Ideal gas constant, $[J/(molK)]$	$R = 8.3143$
Temperature, $[K]$	$T = 358.15$
Faraday's constant, $[C/mol]$	$F = 96487$
Kinetic rate coefficient, $[1/sec]$	$K = 593.93$ (Calculated)
D_3 coefficient, $[m^2/sec]$	$D_3 = 2.4874 \cdot 10^{-14}$ (Calculated)

Table 5.1: Numerical values of the parameters used in the calculation of the D_3 coefficient.

For simplicity, we consider the diffusion coefficient D_1 to be small compared to D_3 and since both are factors of the wavenumber raised in the square power, D_1, gets absorbed in D_3. Therefore, we define a new coefficient c_3, given as

$$c_3 = (D_1 + D_3) \approx D_3. \tag{5.9}$$

Regarding the D_2 diffusion coefficient, that models capillarity-driven surface diffusion and expresses the surface curvature, it can be either positive or negative and it gets determined through the D_3 coefficient, i.e., $D_2 = aD_3$, where $a = const$. We consider both cases and perform a parametric study based on the sign and the value of the D_2 coefficient. Moreover, we define another coefficient c_2 as follows:

$$c_2 = |D_2|, \tag{5.10}$$

where c_2 is always positive and its definition is based on the sign of D_2. For negative curvature, i.e., $D_2 < 0$, we have $c_2 = -D_2 > 0$ and we consider two different subcases based on the value of c_2 compared to the one of c_3, i.e., $c_2 \lessgtr c_3$. In other words, we examine which phenomenon has the most influence on the stability analysis. In particular, in the case that $c_2 > c_3$, the curvature driven interfacial diffusion dominates, whereas if $c_2 < c_3$, the surface energetic driven interfacial deposition prevails. The same strategy is followed for the case of positive curvature, i.e., $c_2 = D_2 > 0$. Finally, for the cases that we find stable regions we add and examine also the contribution of the elastic prestress field.

5.2.1 Interfacial Diffusion with Negative Curvature

We consider a negative diffusion coefficient D_2 and we define $c_2 = -D_2$. With the above modifications and in the absence of elastic prestress, the characteristic equation (5.5) becomes

$$\lambda(\boldsymbol{k}) = c_3|\boldsymbol{k}|^2 + c_2|\boldsymbol{k}|^4, \tag{5.11}$$

or, for the same wavenumber in the two in-plane directions (i.e., $k_1 = k_2 = k$),

$$\lambda(k) = 2c_3k^2 + 4c_2k^4. \tag{5.12}$$

Such a case corresponds always to decay of the perturbation ($\lambda > 0$ since both $c_2, c_3 > 0$) and unconditionally stable growth of the interface. No matter what the value c_2 is, with respect to c_3, the perturbation eventually fades away, c.f., Fig. 5.2.

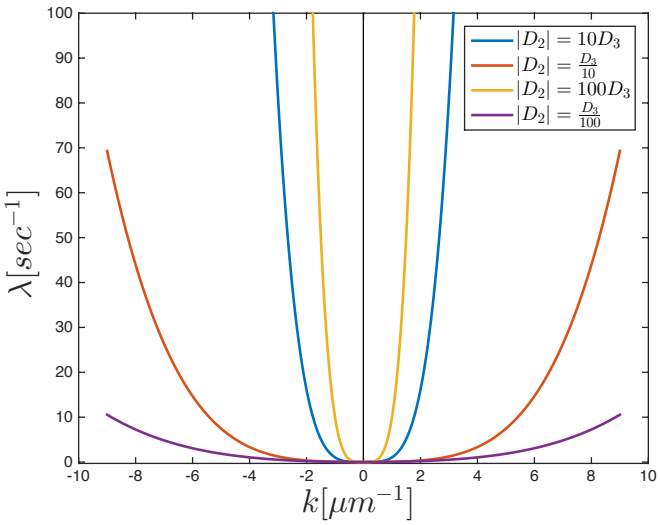

Figure 5.2: Effect of the D_2 and D_3 coefficients on the wavenumber, k. Unconditionally stable perturbation for different values of negative coefficient, D_2: blue ($|D_2| = 10D_3$), red ($|D_2| = \frac{D_3}{10}$), yellow ($|D_2| = 100D_3$), purple ($|D_2| = \frac{D_3}{100}$).

5.2.2 Interfacial Diffusion with Positive Curvature

In this case, we consider a positive diffusion coefficient D_2 and thus $c_2 = D_2$. The characteristic equation (5.5) for equal wavenumbers ($k_1 = k_2 = k$) becomes

$$\lambda(k) = 2c_3k^2 - 4c_2k^4. \tag{5.13}$$

In addition, the critical wavenumber is then defined as follows:

$$|k_c| = \sqrt{\frac{c_3}{2c_2}}. \tag{5.14}$$

In this respect, we have to determine the dominant effect between the curvature driven interfacial diffusion expressed by coefficient c_2 and surface energetic driven interfacial deposition expressed by coefficient c_3.

Considering the case that interfacial diffusion dominates, i.e., $c_2 > c_3$, the perturbation is mostly unstable and the interface evolves in a non-planar way. The stability region is limited to really small wavenumbers of the perturbation, c.f., Fig. 5.3.

On the other hand, when interfacial deposition dominates, i.e., $c_2 < c_3$, the perturbation tends to decay for small wavenumber (k^2 term dominates), while it grows for larger wavenumber (k^4 term dominates). The stability region gets enlarged by decreasing the D_2 coefficient, c.f., Fig. 5.4. In such cases, the effect of the elastic prestress on the critical wavenumber is also considered. As mentioned earlier, the elastic prestress tends to keep the evolution of the interface planar and contributes a positive number to the characteristic equation (5.5).

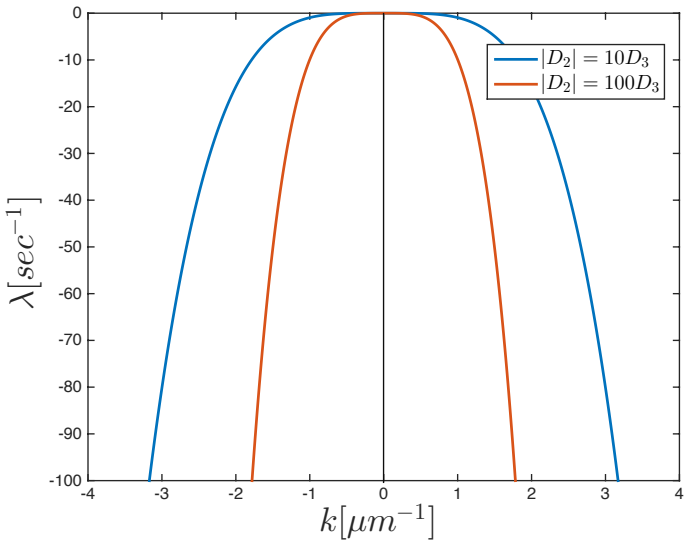

Figure 5.3: Effect of the D_2 and D_3 coefficients on the critical wavenumber, k_c. Mostly unstable perturbation for different values of positive coefficient, D_2: blue ($|D_2| = 10D_3$) with $k_c = 2.24 \cdot 10^{-1}$ $[\mu m^{-1}]$, red ($|D_2| = 100D_3$) with $k_c = 7.07 \cdot 10^{-2}$ $[\mu m^{-1}]$.

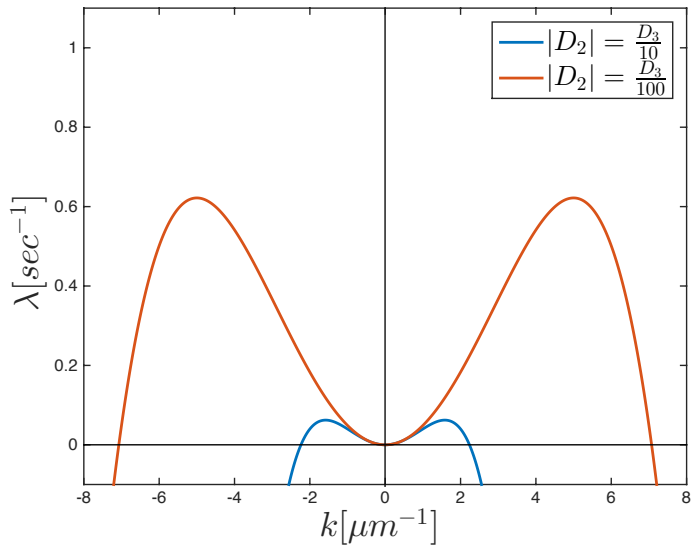

Figure 5.4: Effect of the D_2 and D_3 coefficients on the critical wavenumber, k_c. Stable perturbation for small wavenumber and unstable for larger values of wavenumber. Different values of positive coefficient, D_2: blue ($|D_2| = \frac{D_3}{10}$) with $k_c = 2.24$ $[\mu m^{-1}]$, red ($|D_2| = \frac{D_3}{100}$) with $k_c = 7.07$ $[\mu m^{-1}]$.

In the presence of elastic prestress, i.e., $\sigma^*_{ij} \neq 0$, and in the case that the wavenumbers are the same ($k_1 = k_2 = k$) in the two planar directions and for positive D_2 coefficient, the critical wavenumber, k_c, follows from (5.5) as

$$k_c = \sqrt{\frac{2c_3 + c_4}{4c_2}}, \tag{5.15}$$

where c_4 $[m^2/s]$ is the coefficient that carries along the effect of the elastic prestress and is given by

$$c_4 k^2 = \frac{\Omega K d}{RT} \hat{G}_{ik} [\![\sigma^*_{i\beta}]\!] k_\beta [\![\sigma^*_{k\delta}]\!] k_\delta. \tag{5.16}$$

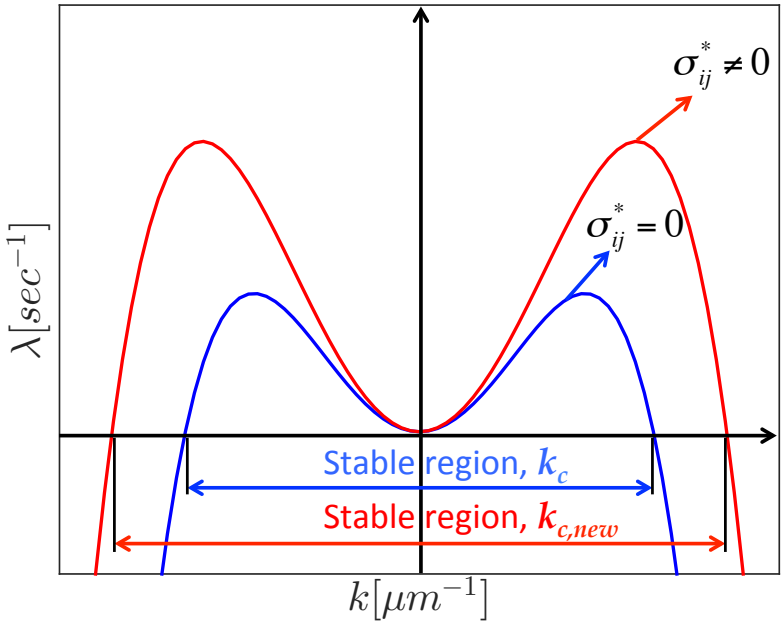

Figure 5.5: Effect of elastic prestress on the critical wavenumber, k_c. Stable region in the absence (blue line) and in the presence (red line) of elastic prestress.

In a general sense, elastic prestress enlarges the stable region by increasing the

critical wavenumber for instability, c.f., Fig. 5.5. In order to quantify that effect we perform parametric analysis in a specific, lithium-LIPON, material system by varying the value of elastic prestress. More specifically, we study two different loading cases, i) uniaxial ($[\![\sigma^*_{11}]\!]$) and ii) biaxial ($[\![\sigma^*_{11}]\!] = [\![\sigma^*_{22}]\!]$), each for three different values of prestress 100, 250, and 500 $[MPa]$ and for the case that the diffusion coefficient, D_2, is positive and has value of $D_2 = \frac{D_3}{100}$, where the stable region is more evident. Note here that the surface Green's function in the transformed domain, $\hat{G}_{ik}$, has been numerically evaluated for this specific material system in section 2.6.

5.2.2.1 Elastic Prestress Contribution - Uniaxial Case

We consider uniaxial loading in the x_1-direction, i.e., $[\![\sigma^*_{11}]\!]$, and the coefficient c_4 is simplified from equation (5.16) to

$$c_4 = \frac{\Omega K d}{RT} \hat{G}_{11} [\![\sigma^*_{11}]\!]^2. \tag{5.17}$$

We demonstrate the effect of the elastic prestress on the critical wavenumber in such case, for three different values of $[\![\sigma^*_{11}]\!]$, c.f., Fig. 5.6. The stability region increases with the application of larger prestress and the value of the initial critical wavenumber in the absence of prestress $k_c = 7.07$ $[\mu m^{-1}]$ increases by 30% to the value of $k_c = 9.10$ $[\mu m^{-1}]$ in the case of the maximum considered value of prestress ($[\![\sigma^*_{11}]\!] = 500$ $[MPa]$).

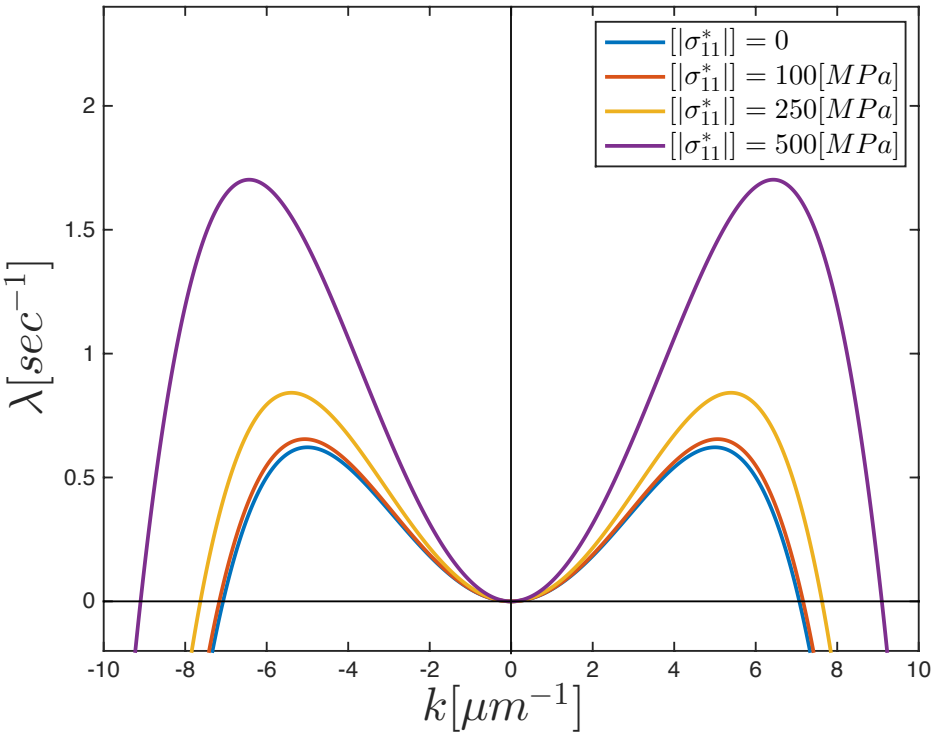

Figure 5.6: Effect of elastic prestress on the critical wavenumber, k_c. Different values of elastic prestress in the case of uniaxial loading with positive coefficient, $D_2 = \frac{D_3}{100}$: blue ($[\![\sigma_{11}^*]\!] = 0$) with $k_c = 7.07$ $[\mu m^{-1}]$, red ($[\![\sigma_{11}^*]\!] = 100$ $[MPa]$) with $k_c = 7.16$ $[\mu m^{-1}]$, yellow ($[\![\sigma_{11}^*]\!] = 250$ $[MPa]$) with $k_c = 7.63$ $[\mu m^{-1}]$, purple ($[\![\sigma_{11}^*]\!] = 500$ $[MPa]$) with $k_c = 9.10$ $[\mu m^{-1}]$.

5.2.2.2 Elastic Prestress Contribution - Biaxial Case

In the case of biaxial loading in the in-plane directions, i.e., $[\![\sigma_{11}^*]\!]$ and $[\![\sigma_{22}^*]\!]$, the coefficient c_4 is determined by (5.16) as

$$c_4 = \frac{\Omega K d}{RT}\Big(\hat{G}_{11}[\![\sigma_{11}^*]\!]^2 + \hat{G}_{12}[\![\sigma_{11}^*]\!][\![\sigma_{22}^*]\!] + \hat{G}_{21}[\![\sigma_{22}^*]\!][\![\sigma_{11}^*]\!] + \hat{G}_{22}[\![\sigma_{22}^*]\!]^2\Big). \tag{5.18}$$

The effect of the elastic prestress on the critical wavenumber in such case is more

evident. The value of the initial critical wavenumber in the absence of prestress $k_c = 7.07\ [\mu m^{-1}]$ increases by 40% to the value of $k_c = 10.02\ [\mu m^{-1}]$ for the maximum considered value of prestress ($[\![\sigma^*_{11}]\!] = 500\ [MPa]$), c.f., Fig. 5.7.

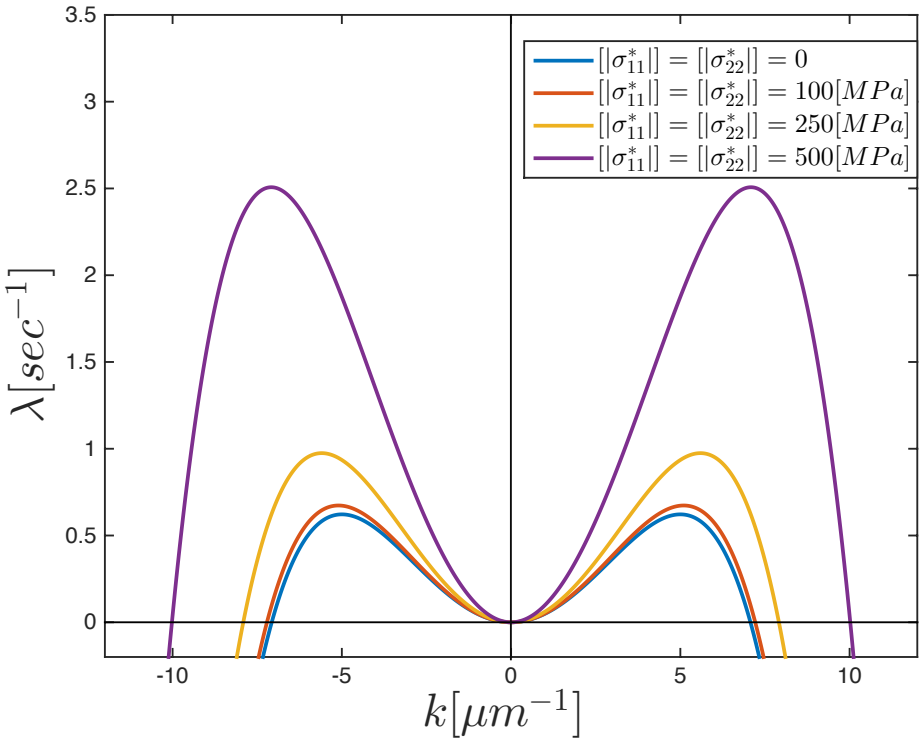

Figure 5.7: Effect of elastic prestress on the critical wavenumber, k_c. Different values of elastic prestress in the case of biaxial loading with positive coefficient, $D_2 = \frac{D_3}{100}$: blue ($[\![\sigma^*_{11}]\!] = [\![\sigma^*_{22}]\!] = 0$) with $k_c = 7.07\ [\mu m^{-1}]$, red ($[\![\sigma^*_{11}]\!] = [\![\sigma^*_{22}]\!] = 100\ [MPa]$) with $k_c = 7.21\ [\mu m^{-1}]$, yellow ($[\![\sigma^*_{11}]\!] = [\![\sigma^*_{22}]\!] = 250\ [MPa]$) with $k_c = 7.91\ [\mu m^{-1}]$, purple ($[\![\sigma^*_{11}]\!] = [\![\sigma^*_{22}]\!] = 500\ [MPa]$) with $k_c = 10.02\ [\mu m^{-1}]$.

Based on the results presented, we can safely conclude that elastic prestress results in maximizing the stable region of the perturbation and tends to keep the interface planar. However, as can be seen from the previous analysis, only larger values of prestress happen to have significant change in the critical wavenumber. Therefore, possible avenues of applying the desirable stress field to the battery cell are yet to be

explored.

5.3 Summary

In this chapter, a stability analysis was performed in order to understand the formation of dendrites (loss of stability). Neglecting the coupling to the electrostatic field, swelling of the electrolyte, pressure-assisted diffusion, and the Maxwell stress, we assumed that the planar interface moves with a constant velocity and we added a small perturbation (wavy interface). It was found that fundamental parameters such as surface diffusivities, surface energy, deposition kinetics, elastic moduli, and the state of prestress are affecting the decay (stability) or the growth (instability) of the initial perturbation. In addition, a parametric study was performed where we leveraged such parameters as an avenue to promote planar evolution of the interface. For a given material system, the effect of elastic prestress was quantified in a manner that can potentially be used in the design of safer, eliminating dendrite formation, Li-air batteries.

Chapter 6

Concluding Remarks and Future Work

6.1 Summary

In this thesis, we put forth a study of a Li electrode-electrolyte interface growth in the presence of an elastic prestress. We find that the stability of a planar interface depends not only on interfacial diffusion properties and interfacial energy but most importantly on the elastic prestress field, whose effect is always to stabilize planar interfacial growth by increasing the critical wavenumber for instability. Numerical simulations that were performed in order to support the theoretical work are in complete agreement with the theoretical predictions. Finally, we quantify the extent of the prestress stabilization in a manner that can potentially be used in the design of Li-air batteries.

In Chapter 1, we presented a general overview on lithium battery technology and more specifically on Li-air batteries. Previous work on them was revised and the motivations and objectives of this work were clearly specified and stated.

In Chapter 2, we formulated the mathematical model of lithium transport through

a solid electrolyte made of an amorphous material, LIPON. This analysis resulted in obtaining the concentration and electrostatic fields in the electrolyte region. In addition, an asymptotic analysis on the nearly flat electrode-electrolyte interface was performed, in order to find the dependence of the elastic energy on the surface profile, a finding that completed the derivation of the equation that describes the evolution of the surface profile. Moreover, the surface Green's function was numerically obtained and lastly, the displacement and stress fields in the bimaterial domain were derived and verified with another theoretical work found in the literature.

In Chapter 3, we presented results on the visualization of surface evolution by time. In particular, using the theory of finite differences and transforming the equation of surface evolution from a partial differential equation into a system of linear algebraic equations, we examined the behavior of the surface as a function of time, with zero and non-zero elastic prestress. The results verify that the elastic prestress stabilizes the interface in a manner that tends to keep it planar.

In Chapter 4, numerical simulations using a commercial finite element software validated the simplified theoretical form of the elastic energy change. Based on the properties of Fourier series and taking advantage of the periodicity of the domain, it was found that the change of the elastic energy with respect to the planar interface depends on the amplitude and wavenumber of the perturbation, the surface Green's function, and the interfacial stress jump. A static linear-elastic 2D problem was modeled in Abaqus FEA under plane strain conditions to support the theoretical predictions. Numerical and theoretical results were found to be in perfect agreement.

In Chapter 5, a linear stability analysis was performed on the surface evolution equation, which was derived in Chapter 2, as an avenue to understand dendrite formation on the interface. It was found that the critical wavenumber for instability depends on various parameters, such as surface diffusivities, interfacial energy, and the state of prestress. A parametric study helped in elucidating and quantifying the effect of such parameters.

6.2 Future Work

In this simplified study of the interfacial growth we neglected pressure-assisted diffusion, electrolyte swelling due to the intercalating lithium ions, and the coupling between the elastic and electrostatic field through the Maxwell stress. Therefore, developing a theory that takes into account these effects would greatly complement this work. Additionally, another future direction would be the consideration of another type of electrolyte besides LIPON. Note here that in Chapter 2, the governing equations were solved for the case of a solid electrolyte, LIPON, where the concentration gradients are negligible. However, it would be an interesting challenge to obtain the concentration and electrostatic fields in an electrolyte where concentration gradients are present and considerable. Also, performing atomistic simulations based on the lithium-LIPON material system would be helpful to provide numerical values for the diffusion coefficients constants D_1 and D_2, which were approximately computed in this work.

Furthermore, other challenges are immediately apparent, such as extending the

current model of a sharp interface in order to take into account phenomena away from the interface as well, using similar techniques to the ones employed in the work of Hou et al. 1999 [50]. Moreover, it has already been found [46, 95] that block copolymers combine favorable electrical and mechanical properties of the electrolyte material since the conducting pathways provide high ionic conducting, while the non conducting ones provide mechanical stability. Therefore, adapting and modifying the current theory so as to apply for the case of block copolymer electrolytes would be another possible solution strategy to resolve the issue of dendrite formation.

Finally, the current theoretical formulation and its predictions were validated with numerical simulations. Results show perfect agreement between theory and computational work. However, it would be a great addition to this work if a series of experiments would be conducted in order to support the theoretical model. A first attempt of experimental validation, along the lines of this theory, in which external pressure concurrent with electric current was applied to a battery cell, has already been conducted at Robert Bosch GmbH, Applied Research (CR/ARM1), in Stuttgart, Germany. The experimental setup and the principle sketch of the battery cell can be seen in Figure 6.1 and 6.2. However, due to short-circuiting, reproducibility could not be achieved in the series of experiments and the experimental results are still in progress.

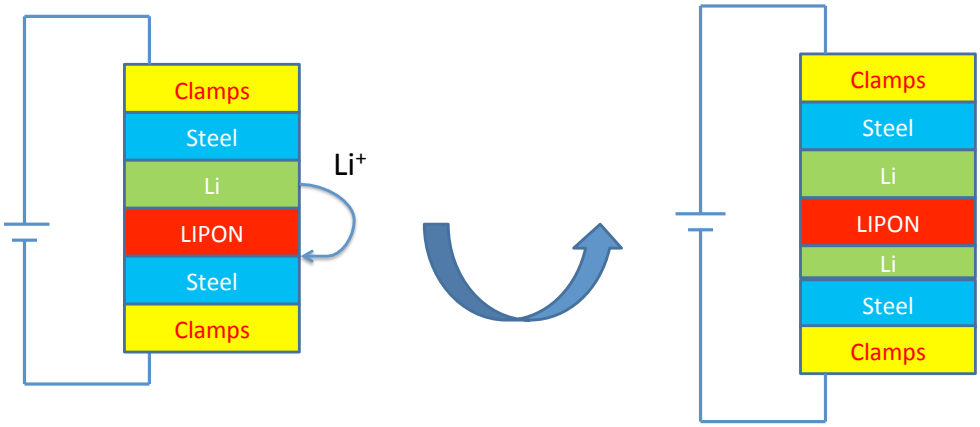

Figure 6.1: Experimental battery cell. Different material layers before (left) and after (right) lithium deposition (Courtesy of Bosch Stuttgart).

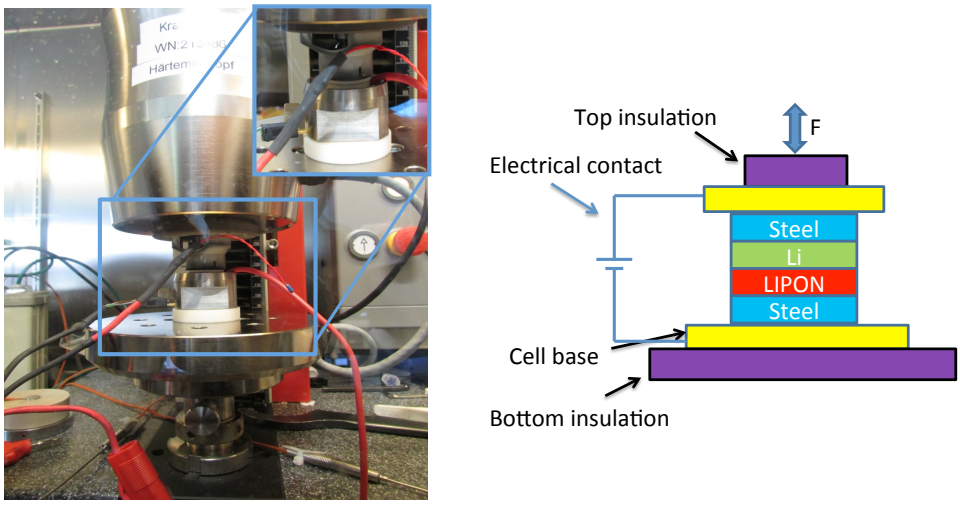

Figure 6.2: Experimental setup and principle sketch (Courtesy of Bosch Stuttgart).

Appendix A

Nondimensionalization

A.1 Nondimensional Parameters

- partial molar volume, Ω : $\tilde{\Omega} = \Omega \cdot c_0 = \left[\frac{m^3}{mol}\right] \cdot \left[\frac{mol}{m^3}\right] = [-]$
- salt concentration, c : $\tilde{c} = \frac{c}{c_0} = \frac{\left[\frac{mol}{m^3}\right]}{\left[\frac{mol}{m^3}\right]} = [-]$
- displacement, u : $\tilde{u} = \frac{u}{r_0} = \frac{[m]}{[m]} = [-]$
- elastic moduli, c_{ijkl} : $\tilde{c}_{ijkl} = \frac{c_{ijkl}}{\frac{RT}{\Omega}} = \frac{\left[\frac{N}{m^2}\right]}{\left[\frac{J}{mol \cdot K}\right] \cdot [K] \cdot \left[\frac{mol}{m^3}\right]} = \frac{\left[\frac{N}{m^2}\right]}{\left[N \cdot m\right] \cdot \left[\frac{1}{m^3}\right]} = [-]$
- effective chemical potential, μ^E : $\tilde{\mu}^E = \frac{\mu^E}{RT} = \frac{\left[\frac{J}{mol}\right]}{\left[\frac{J}{mol \cdot K}\right] \cdot [K]} = [-]$
- hydrostatic stress, p : $\tilde{p} = \frac{p}{\frac{RT}{\Omega}} = \frac{\left[\frac{N}{m^2}\right]}{\left[\frac{J}{mol \cdot K}\right] \cdot [K] \cdot \left[\frac{mol}{m^3}\right]} = \frac{\left[\frac{N}{m^2}\right]}{\left[N \cdot m\right] \cdot \left[\frac{1}{m^3}\right]} = [-]$
- displacement gradient, ∇_x : $\nabla_{\tilde{x}} = \frac{\partial x}{\partial \tilde{x}} \nabla_x = r_0 \nabla_x = [m] \cdot [\frac{1}{m}] = [-]$
- local electrostatic potential, φ : $\tilde{\varphi} = \frac{zF}{RT} \cdot \varphi = \frac{\left[\frac{C}{mol}\right]}{\left[\frac{J}{mol \cdot K}\right] \cdot [K]} \cdot [V] = \frac{[F \cdot V]}{[J]} \cdot [V] = \frac{\left[\frac{J}{V^2}\right]}{\left[J\right]} \cdot [V^2] = [-]$
- time, t : $\tilde{\tau} = t \cdot \frac{D_1}{r_0^2} = [sec] \cdot \frac{\left[\frac{m^2}{sec}\right]}{\left[m^2\right]} = [-]$

- time derivative, ∂_t : $\partial_{\tilde{\tau}} = \frac{\partial}{\partial_t}\frac{\partial_t}{\partial_{\tilde{\tau}}} = \frac{r_0^2}{D_1}\partial_t = \frac{\left[m^2\right]}{\left[\frac{m^2}{sec}\right]} \cdot \left[\frac{1}{sec}\right] = [-]$

- vector flux, J : $\tilde{J} = J \cdot \frac{r_0}{D_1 \cdot c_0} = \left[\frac{mol}{m^2 \cdot sec}\right] \cdot \frac{[m]}{\left[\frac{m^2}{sec}\right] \cdot \left[\frac{mol}{m^3}\right]} = [-]$

- interfacial mass flux, $\boldsymbol{j}_p$: $\tilde{\boldsymbol{j}}_p = \frac{\boldsymbol{j}_p}{K d r_0} = \frac{\left[\frac{m^2}{sec}\right]}{\left[\frac{1}{sec}\right] \cdot [m] \cdot [m]} = [-]$

- electrochemical mass flux, j_m $\tilde{j}_m = \frac{j_m}{K d c_0} = \frac{\left[\frac{mol}{m^2 \cdot sec}\right]}{\left[\frac{1}{sec}\right] \cdot [m] \cdot \left[\frac{mol}{m^3}\right]} = [-]$

- mass deposition rate, j_h : $\tilde{j}_h = \frac{j_h}{K d c_0} = \frac{\left[\frac{mol}{m^2 \cdot sec}\right]}{\left[\frac{1}{sec}\right] \cdot [m] \cdot \left[\frac{mol}{m^3}\right]} = [-]$

- chemical potential density, μ_h : $\tilde{\mu}_h = \frac{\mu_h}{\frac{RT}{\Omega}} = \frac{\left[\frac{J}{m3}\right] \cdot \left[\frac{m^3}{mol}\right]}{\left[\frac{J}{mol \cdot K}\right] \cdot [K]} = [-]$

- diffusion coefficient, D_1 : $\tilde{D}_1 = \frac{D_1}{K r_0^2} = \frac{\left[\frac{m^2}{sec}\right]}{\left[\frac{1}{sec}\right] \cdot [m^2]} = [-]$

- diffusion coefficient, D_2 : $\tilde{D}_2 = \frac{D_2}{K r_0^4} = \frac{\left[\frac{m^4}{sec}\right]}{\left[\frac{1}{sec}\right] \cdot [m^4]} = [-]$

- surface parameter, D_3: $\tilde{D}_3 = \frac{D_3}{K r_0^2} = \frac{\left[\frac{m^2}{sec}\right]}{\left[\frac{1}{sec}\right] \cdot [m^2]} = [-]$

- profile function, h: $\tilde{h} = \frac{h}{d} = \frac{[m]}{[m]} = [-]$

- electric permittivity, ε : $\tilde{\varepsilon} = \frac{\varepsilon RT}{z^2 F^2 r_0^2 c_0} = \frac{\left[\frac{F}{m}\right]\left[\frac{J}{molK}\right][K]}{\left[\frac{C^2}{mol^2}\right][m^2]\left[\frac{mol}{m^3}\right]} = \left[\frac{FJ}{C^2}\right] = [-]$

Note: r_0 is the particle size

A.2 Nondimensional Equations

- The effective chemical potential of the electrolyte, equation (2.5):

$$\begin{aligned} \mu^E &= \mu_0^E + \nu RT log(f_\pm \frac{c}{c_0}) - \Omega p \\ \Rightarrow \frac{\mu^E}{RT} &= \frac{\mu_0^E}{RT} + \nu log(f_\pm \frac{c}{c_0}) - \frac{\Omega p}{RT} \\ \rightarrow \tilde{\mu}^E &= \tilde{\mu}_0^E + \nu log(f_\pm \tilde{c}) - \tilde{p} \end{aligned}$$

- Equation of surface evolution

  The interfacial mass flux equation (2.19):

$$\begin{aligned} \boldsymbol{j}_p &= -\nabla(D_1 h + D_2 \nabla^2 h) \\ \Rightarrow \frac{\boldsymbol{j}_p}{K d r_0} &= -\frac{1}{r_0}\nabla_{\tilde{x}} \frac{1}{K d r_0}(D_1 h + D_2 \frac{1}{r_0^2}\nabla_{\tilde{x}}^2 h) \\ \Rightarrow \tilde{\boldsymbol{j}}_p &= -\nabla_{\tilde{x}}(\tilde{D}_1 \tilde{h} + \tilde{D}_2 \nabla_{\tilde{x}}^2 \tilde{h}) \end{aligned}$$

  The electrochemical mass flux equation (2.20):

$$\begin{aligned} j_m &= \frac{Kd}{\Omega}\frac{\mu^E - \mu_0^S}{RT} \\ \Rightarrow \frac{j_m}{K d c_0} &= \frac{1}{\Omega c_0}\frac{\mu^E - \mu_0^S}{RT} \\ \Rightarrow \tilde{j}_m &= \frac{\tilde{\mu}^E - \tilde{\mu}_0^S}{\tilde{\Omega}} \end{aligned}$$

The mass deposition rate equation (2.25):

$$
\begin{aligned}
j_h &= -\frac{Kd}{RT}\mu_h \\
\Rightarrow \frac{j_h}{Kdc_0} &= -\frac{1}{\Omega c_0}\frac{\mu_h \Omega}{RT} \\
\Rightarrow \tilde{j}_h &= -\frac{\tilde{\mu}_h}{\tilde{\Omega}}
\end{aligned}
$$

Finally, conservation of mass equation (2.27):

$$
\begin{aligned}
\frac{\partial h}{\partial t} + \nabla \cdot \boldsymbol{j}_p &= \Omega(j_m + j_h) \\
\Rightarrow \frac{dD_1}{r_0^2}\frac{\partial \tilde{h}}{\partial \tilde{\tau}} + \frac{1}{r_0}\nabla_{\tilde{x}} \cdot \tilde{\boldsymbol{j}}_p Kdr_0 &= \frac{\tilde{\Omega}}{c_0}(\tilde{j}_m Kdc_0 + \tilde{j}_h Kdc_0) \\
\Rightarrow \frac{dD_1}{r_0^2}\frac{\partial \tilde{h}}{\partial \tilde{\tau}} + \nabla_{\tilde{x}} \cdot \tilde{\boldsymbol{j}}_{\boldsymbol{p}} Kd &= Kd\tilde{\Omega}(\tilde{j}_m + \tilde{j}_h) \\
\Rightarrow \tilde{D}_1\frac{\partial \tilde{h}}{\partial \tilde{\tau}} + \nabla_{\tilde{x}} \cdot \tilde{\boldsymbol{j}}_{\boldsymbol{p}} &= \tilde{\Omega}(\tilde{j}_m + \tilde{j}_h)
\end{aligned}
$$

or,

$$
\begin{aligned}
\frac{\partial h}{\partial t} &= \nabla^2(D_1 h + D_2\nabla^2 h) + \frac{Kd}{RT}(\mu^E - \mu_0^S) - \frac{\Omega K d}{RT}\mu_h \\
\Rightarrow \frac{dD_1}{r_0^2}\frac{\partial \tilde{h}}{\partial \tilde{\tau}} &= \frac{1}{r_0^2}\nabla_{\tilde{x}}^2(D_1 d\tilde{h} + D_2 d\frac{1}{r_0^2}\nabla_{\tilde{x}}^2\tilde{h}) + Kd(\tilde{\mu}^E - \tilde{\mu}_0^S) - Kd\tilde{\mu}_h \\
\Rightarrow \frac{D_1}{Kr_0^2}\frac{\partial \tilde{h}}{\partial \tilde{\tau}} &= \nabla_{\tilde{x}}^2(\frac{D_1}{Kr_0^2}\tilde{h} + \frac{D_2}{Kr_0^4}\nabla_{\tilde{x}}^2\tilde{h}) + (\tilde{\mu}^E - \tilde{\mu}_0^s) - \tilde{\mu}_h \\
\Rightarrow \tilde{D}_1\frac{\partial \tilde{h}}{\partial \tilde{\tau}} &= \nabla_{\tilde{x}}^2(\tilde{D}_1\tilde{h} + \tilde{D}_2\nabla_{\tilde{x}}^2\tilde{h}) + (\tilde{\mu}^E - \tilde{\mu}_0^S) - \tilde{\mu}_h
\end{aligned}
$$

- Stability equation (5.3):

$$
\begin{aligned}
\frac{\partial u}{\partial t} &= \nabla^2(D_1 u + D_2\nabla^2 u) + \frac{\Omega K d}{RT}\left(\gamma\nabla^2 u + \int_{\mathbb{R}^2} G_{ik,\beta}(\boldsymbol{x}-\boldsymbol{x}')[\![\sigma_{i\beta}^*]\!][\![\sigma_{k\delta}^*]\!]u_{,\delta}(\boldsymbol{x}')\,d\boldsymbol{x}'\right) \\
\Rightarrow \frac{D_1}{r_0^2}r_0\frac{\partial \tilde{u}}{\partial \tilde{\tau}} &= \frac{1}{r_0^2}\nabla_{\tilde{x}}^2(D_1 r_0\tilde{u} + D_2 r_0\frac{1}{r_0^2}\nabla_{\tilde{x}}^2\tilde{u}) + D_3 r_0\frac{1}{r_0^2}\nabla_{\tilde{x}}^2\tilde{u} \\
&\quad + \frac{\Omega K d}{RT}\int_{\mathbb{R}^2} G_{ik,\beta}(\boldsymbol{x}-\boldsymbol{x}')[\![\sigma_{i\beta}^*]\!][\![\sigma_{k\delta}^*]\!]u_{,\delta}(\boldsymbol{x}')\,d\boldsymbol{x}' \\
\Rightarrow \frac{D_1}{Kr_0^2}\frac{\partial \tilde{u}}{\partial \tilde{\tau}} &= \nabla_{\tilde{x}}^2(\frac{D_1}{Kr_0^2}\tilde{u} + \frac{D_2}{Kr_0^4}\nabla_{\tilde{x}}^2\tilde{u}) + \frac{D_3}{Kr_0^2}\nabla_{\tilde{x}}^2\tilde{u} \\
&\quad + \frac{\Omega K d}{RT}\int_{\mathbb{R}^2} G_{ik,\beta}(\boldsymbol{x}-\boldsymbol{x}')[\![\sigma_{i\beta}^*]\!][\![\sigma_{k\delta}^*]\!]u_{,\delta}(\boldsymbol{x}')\,d\boldsymbol{x}' \\
\Rightarrow \tilde{D}_1\frac{\partial \tilde{u}}{\partial \tilde{\tau}} &= \nabla_{\tilde{x}}^2(\tilde{D}_1\tilde{u} + \tilde{D}_2\nabla_{\tilde{x}}^2\tilde{u}) + \tilde{D}_3\nabla_{\tilde{x}}^2\tilde{u} + \frac{\Omega K d}{RT}\int_{\mathbb{R}^2} G_{ik,\beta}(\boldsymbol{x}-\boldsymbol{x}')[\![\sigma_{i\beta}^*]\!][\![\sigma_{k\delta}^*]\!]u_{,\delta}(\boldsymbol{x}')\,d\boldsymbol{x}'
\end{aligned}
$$

Appendix B

MATLAB Code - Green's Funtion

Contents

```
% input data: wavenumbers k_1, k_2 and stiffness matrices c^+, c- for the
% two materials (lithium-LIPON)
% fill-in the matrices A, B and C
% solve the quadratic eigenvalue problem
% create a base, apply BC's to find the constants Vp and then find displacements
% find G_hat matrix, displacements at the interface x3=0
clear all
close all
clc
```

Stiffness matrix c_{ijkl} for x_3>0

```
nu_p=0.3;           % Poisson's ratio of LIPON
E_p=77*10^(-3);     % Young's modulus of LIPON [N/um2]
lambda_lame_p=nu_p*E_p/((1+nu_p)*(1-2*nu_p));   % lambda
```

```
mu_p=E_p/(2*(1+nu_p));                              % mu


kappa_p=zeros(2,1);
kappa_p(1)=2*pi;     % wavenumbers
kappa_p(2)=2*pi;


Stiff_C_p=zeros(3,3,3,3);   % initialize the Stiffness matrix c
% Stiffness matrix c, for isotropic material LIPON
for i=1:3
    for j=1:3
        for k=1:3
            for l=1:3
                Stiff_C_p(i,j,k,l)=lambda_lame_p*(i==j)*(k==l)+ ...
                mu_p*((i==k)*(j==l)+(i==l)*(j==k));
            end
        end
    end
end
```

Matrices A,B and C for x_3>0

```
% matriz A
A_p=zeros(3,3);
```

```
for i=1:3
    for k=1:3
        A_p(i,k)=Stiff_C_p(i,3,k,3);
    end
end
% matrix B
B_p=zeros(3,3);
for i=1:3
    for k=1:3
    B_p(i,k)=Stiff_C_p(i,1,k,3)*kappa_p(1)+Stiff_C_p(i,2,k,3)*kappa_p(2)...
    +Stiff_C_p(i,3,k,1)*kappa_p(1)+Stiff_C_p(i,3,k,2)*kappa_p(2);
    end
end
% matrix C
C_p=zeros(3,3);
for i=1:3
    for k=1:3
       C_p(i,k)=-Stiff_C_p(i,1,k,1)*kappa_p(1)*kappa_p(1) ...
       -Stiff_C_p(i,2,k,1)*kappa_p(2)*kappa_p(1)-Stiff_C_p(i,1,k,2) ...
       *kappa_p(1)*kappa_p(2)-Stiff_C_p(i,2,k,2)*kappa_p(2)*kappa_p(2);
    end
end
```

Quadratic eigenvalue problem for x_3>0

```
[X_p,e_p]=polyeig(C_p,1i*B_p,A_p);  % X_p eigenvectors and e_p eigenvalues
```

Stiffness matrix c_{ijkl} for x_3<0

```
kappa_m=zeros(2,1);

kappa_m(1)=2*pi;     % wavenumbers

kappa_m(2)=2*pi;


Stiff_C_m=zeros(3,3,3,3);   % initialize the Stiffness matrix c

% Stiffness matrix c, for cubic lithium material in [N/um2]

Stiff_C_m(1,1,1,1)=13.5*10^(-3);

Stiff_C_m(2,2,2,2)=Stiff_C_m(1,1,1,1);

Stiff_C_m(3,3,3,3)=Stiff_C_m(1,1,1,1);

Stiff_C_m(1,1,2,2)=11.44*10^(-3);

Stiff_C_m(1,1,3,3)=Stiff_C_m(1,1,2,2);

Stiff_C_m(2,2,3,3)=Stiff_C_m(1,1,2,2);

Stiff_C_m(2,2,1,1)=Stiff_C_m(1,1,2,2);

Stiff_C_m(3,3,1,1)=Stiff_C_m(1,1,3,3);

Stiff_C_m(3,3,2,2)=Stiff_C_m(2,2,3,3);

Stiff_C_m(1,2,1,2)=8.78*10^(-3);

Stiff_C_m(2,1,1,2)=Stiff_C_m(1,2,1,2);

Stiff_C_m(1,2,2,1)=Stiff_C_m(1,2,1,2);
```

```
Stiff_C_m(2,1,2,1)=Stiff_C_m(1,2,1,2);

Stiff_C_m(1,3,1,3)=Stiff_C_m(1,2,1,2);

Stiff_C_m(3,1,1,3)=Stiff_C_m(1,2,1,2);

Stiff_C_m(1,3,3,1)=Stiff_C_m(1,2,1,2);

Stiff_C_m(3,1,3,1)=Stiff_C_m(1,2,1,2);

Stiff_C_m(2,3,2,3)=Stiff_C_m(1,2,1,2);

Stiff_C_m(3,2,2,3)=Stiff_C_m(1,2,1,2);

Stiff_C_m(2,3,3,2)=Stiff_C_m(1,2,1,2);

Stiff_C_m(3,2,3,2)=Stiff_C_m(1,2,1,2);
```

Matrices A,B and C for x_3<0

```
% matrix A

A_m=zeros(3,3);

for i=1:3

    for k=1:3

        A_m(i,k)=Stiff_C_m(i,3,k,3);

    end

end

% matrix B

B_m=zeros(3,3);

for i=1:3

    for k=1:3
```

```
    B_m(i,k)=Stiff_C_m(i,1,k,3)*kappa_m(1)+Stiff_C_m(i,2,k,3)*kappa_m(2)...
    +Stiff_C_m(i,3,k,1)*kappa_m(1)+Stiff_C_m(i,3,k,2)*kappa_m(2);
    end
end
% matrix C
C_m=zeros(3,3);
for i=1:3
    for k=1:3
    C_m(i,k)=-Stiff_C_m(i,1,k,1)*kappa_m(1)*kappa_m(1) ...
    -Stiff_C_m(i,2,k,1)*kappa_m(2)*kappa_m(1)-Stiff_C_m(i,1,k,2) ...
    *kappa_m(1)*kappa_m(2)-Stiff_C_m(i,2,k,2)*kappa_m(2)*kappa_m(2);
    end
end
```

Quadratic eigenvalue problem for x_3<0

```
[X_m,e_m]=polyeig(C_m,1i*B_m,A_m);   % X_m eigenvectors and e_m eigenvalues
```

Create a base by choosing the preferred eigenvectors

```
index_p=find( real(e_p) < 0);     % check positive and negative real part
index_m=find( real(e_m) > 0);
U1_p=X_p(:,index_p(1));  % eigenvectors for positive region, x3>0
U2_p=X_p(:,index_p(2));
```

```
U3_p=X_p(:,index_p(3));

U1_m=X_m(:,index_m(1));  % eigenvectors for negative region, x3<0

U2_m=X_m(:,index_m(2));

U3_m=X_m(:,index_m(3));

lambda1_p=e_p(index_p(1));  % eigenvalues for positive region, x3>0

lambda2_p=e_p(index_p(2));

lambda3_p=e_p(index_p(3));

lambda1_m=e_m(index_m(1));  % eigenvalues for negative region, x3<0

lambda2_m=e_m(index_m(2));

lambda3_m=e_m(index_m(3));

U=[U1_p U2_p U3_p U1_m U2_m U3_m];  % gather all the preferred eigenvectors

% gather all the preferred eigenvalues

lambda=[lambda1_p lambda2_p lambda3_p lambda1_m lambda2_m lambda3_m];
```

Apply BC's, find constants Vp by solving the linear system Ax=b

```
t=[1 0 0; 0 1 0; 0 0 1];

b=[0 0 0; 0 0 0; 0 0 0; -t];   % b loading matrix 6x3

% A matrix corresponds to the BC

A_up=zeros(3,6);      % displacement bc

A_down=zeros(3,6);    % stresses bc

A_up = [U(1,1:3) -U(1,4:6);
```

```
      U(2,1:3) -U(2,4:6);
      U(3,1:3) -U(3,4:6)];
for i=1:3
  for p=1:3,
    for l=1:3,
      A_down(i,p) = A_down(i,p) + Stiff_C_p(i,3,l,1)*1i*kappa_p(1)*U(l,p) ...
                        + Stiff_C_p(i,3,l,2)*1i*kappa_p(2)*U(l,p) ...
                        + Stiff_C_p(i,3,l,3)*lambda(p)*U(l,p);
      q=p+3;
      A_down(i,q) = A_down(i,q) - Stiff_C_m(i,3,l,1)*1i*kappa_m(1)*U(l,q) ...
                        - Stiff_C_m(i,3,l,2)*1i*kappa_m(2)*U(l,q) ...
                        - Stiff_C_m(i,3,l,3)*lambda(q)*U(l,q);
    end;
  end;
end;
A=[A_up;A_down];
% solve Ax=b to find Vp matrix 6x3  x=V=[V_p1;V_p2;V_p3;V_m1;V_m2;V_m3]
V=A\b;
```

find $\hat{G} = u_i(0)$ displacements at the interface $x_3 = 0$

```
u_zero=zeros(3,3);   % Initialize displacements at the interface x_3=0
for i=1:3
```

```
    for j=1:3
        u_zero(i,j)=V(1,j)*U1_p(i)+V(2,j)*U2_p(i)+V(3,j)*U3_p(i);
    end
end
G_hat=t\u_zero   % 3x3 G_hat matrix [um3/N]


G_hat =

  Columns 1 through 2

   2.8050e+00 + 7.0716e-10i  -6.4476e-01 + 5.5349e-09i

  -6.4476e-01 - 3.7598e-10i   2.8050e+00 + 4.4518e-09i

  -1.4595e-08 - 3.2652e-01i  -2.8774e-08 - 3.2652e-01i

  Column 3

   5.5045e-09 + 3.2652e-01i

   7.0772e-09 + 3.2652e-01i

   2.2303e+00 - 3.2032e-08i
```

Bibliography

[1] Argonne National Laboratory (Transportation Technology R&D Center U.S. Department of Energy). *http://www.transportation.anl.gov/features/2009_Li-air_batteries.html*.

[2] F. Abaqus. Simulia website. dassault systemes, 2010.

[3] K. Abraham and Z. Jiang. A polymer electrolytebased rechargeable lithium/oxygen battery. *Journal of The Electrochemical Society*, 143(1):1–5, 1996.

[4] R. Akolkar. Mathematical model of the dendritic growth during lithium electrodeposition. *Journal of Power Sources*, 232:23–28, 2013.

[5] P. Albertus, G. Girishkumar, B. McCloskey, R. S. Snchez-Carrera, B. Kozinsky, J. Christensen, and A. Luntz. Identifying capacity limitations in the li/oxygen battery using experiments and modeling. *Journal of The Electrochemical Society*, 158(3):A343–A351, 2011.

[6] C. P. Andersen, H. Hu, G. Qiu, V. Kalra, and Y. Sun. Pore-scale transport resolved model incorporating cathode microstructure and peroxide growth in lithium-air batteries. *Journal of The Electrochemical Society*, 162(7):A1135–A1145, 2015.

[7] G. Antczak and G. Ehrlich. *Surface diffusion: metals, metal atoms, and clusters*. Cambridge University Press, 2010.

[8] M. Armand. Polymer solid electrolytes-an overview. *Solid State Ionics*, 9:745–754, 1983.

[9] A. Aryanfar, T. Cheng, A. J. Colussi, B. V. Merinov, W. A. Goddard III, and M. R. Hoffmann. Annealing kinetics of electrodeposited lithium dendrites. *The Journal of Chemical Physics*, 143(13):134701, 2015.

[10] D. M. Barnett and J. Lothe. Line force loadings on anisotropic half-spaces and wedges. *Physica Norvegica*, 8(1):13–22, 1975. Ad196 Times Cited:91 Cited References Count:11.

[11] J. L. Barton and J. Bockris. The electrolytic growth of dendrites from ionic solutions. *Proceedings of the Royal Society of London. Series A. Mathematical and Physical Sciences*, 268(1335):485–505, 1962.

[12] J. B. Bates, N. J. Dudney, G. R. Gruzalski, R. A. Zuhr, A. Choudhury, C. F. Luck, and J. D. Robertson. Electrical properties of amorphous lithium electrolyte thin films. *Solid State Ionics*, 53:647–654, 1992.

[13] J. B. Bates, N. J. Dudney, G. R. Gruzalski, R. A. Zuhr, A. Choudhury, C. F. Luck, and J. D. Robertson. Fabrication and characterization of amorphous lithium electrolyte thin films and rechargeable thin-film batteries. *Journal of power sources*, 43(1):103–110, 1993.

[14] M. Z. Bazant. Theory of chemical kinetics and charge transfer based on nonequilibrium thermodynamics. *Accounts of chemical research*, 46(5):1144–1160, 2013.

[15] K. F. Blurton and A. F. Sammells. Metal/air batteries: their status and potential-a review. *Journal of Power Sources*, 4(4):263–279, 1979.

[16] E. Bohn, T. Eckl, M. Kamlah, and R. McMeeking. A model for lithium diffusion and stress generation in an intercalation storage particle with phase change. *Journal of The Electrochemical Society*, 160(10):A1638–A1652, 2013.

[17] J. Boussinesq. *Application des potentiels l'tude de l'quilibre et du mouvement des solides lastiques: principalement au calcul des dformations et des pressions que produisent, dans ces solides, des efforts quelconques exercs sur une petite partie de leur surface ou de leur intrieur: mmoire suivi de notes tendues sur divers points de physique, mathematique et d'analyse*, volume 4. Gauthier-Villars, 1885.

[18] A. F. Bower. *Applied mechanics of solids*. CRC press, 2009.

[19] R. Bracewell. The fourier transform and its applications. *New York*, 1965.

[20] J. N. Chazalviel. Electrochemical aspects of the generation of ramified metallic electrodeposits. *Physical review A*, 42(12):7355, 1990.

[21] J. Christensen, P. Albertus, R. S. Sanchez-Carrera, T. Lohmann, B. Kozinsky, R. Liedtke, J. Ahmed, and A. Kojic. A critical review of li/air batteries. *Journal of the Electrochemical Society*, 159(2):R1–R30, 2011.

[22] J. W. Cooley, P. A. Lewis, and P. D. Welch. Application of the fast fourier transform to computation of fourier integrals, fourier series, and convolution integrals. *Audio and Electroacoustics, IEEE Transactions on*, 15(2):79–84, 1967.

[23] A. Despic and K. I. Popov. *Transport-controlled deposition and dissolution of metals*, pages 199–313. Springer, 1972.

[24] R. Deutscher and S. Fletcher. Nucleation on active sites: Part i. probabilistic formulae for the numbers of crystals. *Journal of electroanalytical chemistry and interfacial electrochemistry*, 164(1):1–9, 1984.

[25] R. Deutscher and S. Fletcher. The deconvolution of nucleation and growth rates from electrochemical currenttime transients. *Journal of the Chemical Society, Faraday Transactions*, 94(24):3527–3536, 1998.

[26] R. L. Deutscher and S. Fletcher. Nucleation on active sites: Part iv. invention of an electronic method of counting the number of crystals as a function of time; and the discovery of nucleation rate dispersion. *Journal of electroanalytical chemistry and interfacial electrochemistry*, 239(1):17–54, 1988.

[27] J. W. Diggle, A. R. Despic, and J. Bockris. The mechanism of the dendritic electrocrystallization of zinc. *Journal of The Electrochemical Society*, 116(11):1503–1514, 1969.

[28] M. Dolle, L. Sannier, B. Beaudoin, M. Trentin, and J.-M. Tarascon. Live scanning electron microscope observations of dendritic growth in lithium/polymer cells. *Electrochemical and solid-state letters*, 5(12):A286–A289, 2002.

[29] C. M. Doyle. Design and simulation of lithium rechargeable batteries. *Lawrence Berkeley National Laboratory*, 2010.

[30] M. Doyle, T. F. Fuller, and J. Newman. Modeling of galvanostatic charge and discharge of the lithium/polymer/insertion cell. *Journal of the Electrochemical Society*, 140(6):1526–1533, 1993.

[31] M. Doyle and J. Newman. The use of mathematical modeling in the design of lithium/polymer battery systems. *Electrochimica Acta*, 40(13):2191–2196, 1995.

[32] N. J. Dudney, J. B. Bates, R. A. Zuhr, C. F. Luck, and J. D. Robertson. Sputtering of lithium compounds for preparation of electrolyte thin films. *solid state ionics*, 53:655–661, 1992.

[33] J. Dundurs and M. Hetenyi. Transmission of force between two semi-infinite solids. *Journal of Applied Mechanics*, 32(3):671–674, 1965.

[34] D. R. Ely and R. E. Garca. Heterogeneous nucleation and growth of lithium electrodeposits on negative electrodes. *Journal of the Electrochemical Society*, 160(4):A662–A668, 2013.

[35] I. Epelboin, M. Froment, M. Garreau, J. Thevenin, and D. Warin. Behavior of secondary lithium and aluminumlithium electrodes in propylene carbonate. *Journal of The Electrochemical Society*, 127(10):2100–2104, 1980.

[36] E. Eweka, J. Owen, and A. Ritchie. Electrolytes and additives for high efficiency lithium cycling. *Journal of power sources*, 65(1):247–251, 1997.

[37] N. Fares and V. C. Li. General image method in a plane-layered elastostatic medium. *ASME, Transactions, Journal of Applied Mechanics*, 55:781–785, 1988.

[38] J. Fish and T. Belytschko. *A first course in finite elements*. John Wiley and Sons, 2007.

[39] S. A. Freunberger, Y. Chen, Z. Peng, J. M. Griffin, L. J. Hardwick, F. Bard, P. Novk, and P. G. Bruce. Reactions in the rechargeable lithium-o_2 battery with alkyl carbonate electrolytes. *Journal of the American Chemical Society*, 133(20):8040–8047, 2011.

[40] H. Gao. Stress concentration at slightly undulating surfaces. *Journal of the Mechanics and Physics of Solids*, 39(4):443–458, 1991.

[41] H. Gao. Some general properties of stress-driven surface evolution in a heteroepitaxial thin film structure. *Journal of the Mechanics and Physics of Solids*, 42(5):741–772, 1994.

[42] G. Girishkumar, B. McCloskey, A. C. Luntz, S. Swanson, and W. Wilcke. Lithium air battery: promise and challenges. *The Journal of Physical Chemistry Letters*, 1(14):2193–2203, 2010.

[43] D. P. Gregory. *Metal-air batteries*, volume 6. Mills and Boon, 1972.

[44] M. U. Guide. The mathworks. *Inc., Natick, MA*, 5:333, 1998.

[45] R. Haberman. Elementary applied partial differential equations: with fourier series and boundary value problems. *The American Mathematical Monthly*, 1985.

[46] D. T. Hallinan, S. A. Mullin, G. M. Stone, and N. P. Balsara. Lithium metal stability in batteries with block copolymer electrolytes. *Journal of The Electrochemical Society*, 160(3):A464–A470, 2013.

[47] E. G. Herbert, W. E. Tenhaeff, N. J. Dudney, and G. M. Pharr. Mechanical characterization of lipon films using nanoindentation. *Thin Solid Films*, 520(1):413–418, 2011.

[48] C. Herring. Surface tension as a motivation for sintering. In w. E. Kingston, editor, *The Physics of Powder Metallurgy*. McGraw-Hill, New York, 1951.

[49] T. Hirai, I. Yoshimatsu, and J. Yamaki. Influence of electrolyte on lithium cycling efficiency with pressurized electrode stack. *Journal of The Electrochemical Society*, 141(3):611–614, 1994.

[50] T. Y. Hou, P. Rosakis, and P. LeFloch. A level-set approach to the computation of twinning and phase-transition dynamics. *Journal of Computational Physics*, 150(2):302–331, 1999.

[51] T. J. Hughes. The finite element methodprentice-hall. *Englewood cliffs, NJ*, 1987.

[52] J. S. Hummelshoj, J. Blomqvist, S. Datta, T. Vegge, J. Rossmeisl, K. S. Thygesen, A. Luntz, K. W. Jacobsen, and J. K. Norskov. Communications: Elementary oxygen electrode reactions in the aprotic li-air battery. *The Journal of chemical physics*, 132(7):071101, 2010.

[53] K. Kanamura, S. Shiraishi, and Z. Takehara. Electrochemical deposition of very smooth lithium using nonaqueous electrolytes containing hf. *Journal of The Electrochemical Society*, 143(7):2187–2197, 1996.

[54] L. Kelvin. Note on the integration of the equations of equilibrium of an elastic solid. *Cambridge and Dublin Mathematical Journal*, 3:87–89, 1848.

[55] M. D. Korzec. Continuum modeling, analysis and simulation of the self-assembly of thin crystalline films. 2010.

[56] A. Kraytsberg and Y. Ein-Eli. Review on li-air batteries-opportunities, limitations and perspective. *Journal of Power Sources*, 196(3):886–893, 2011.

[57] B. Kumar, J. Kumar, R. Leese, J. P. Fellner, S. J. Rodrigues, and K. Abraham. A solid-state, rechargeable, long cycle life lithiumair battery. *Journal of The Electrochemical Society*, 157(1):A50–A54, 2010.

[58] Z.-W. Lai and S. D. Sarma. Kinetic growth with surface relaxation: Continuum versus atomistic models. *Physical review letters*, 66(18):2348, 1991.

[59] M. Landstorfer, S. Funken, and T. Jacob. An advanced model framework for solid electrolyte intercalation batteries. *Physical Chemistry Chemical Physics*, 13(28):12817–12825, 2011.

[60] A. Latz and J. Zausch. Thermodynamic consistent transport theory of li–ion batteries. *Journal of Power Sources*, 196(6):3296–3302, 2011.

[61] A. Latz, J. Zausch, and O. Iliev. *Modeling of species and charge transport in li-ion batteries based on non-equilibrium thermodynamics*. Springer, 2011.

[62] L. Le Van-Jodin, F. Ducroquet, F. Sabary, and I. Chevalier. Dielectric properties, conductivity and $li+$ ion motion in lipon thin films. *Solid State Ionics*, 253:151–156, 2013.

[63] J. Lee, S. Tai Kim, R. Cao, N. Choi, M. Liu, K. T. Lee, and J. Cho. Metal-air batteries with high energy density: Li-air versus zn-air. *Advanced Energy Materials*, 1(1):34–50, 2011.

[64] R. J. LeVeque. *Finite difference methods for ordinary and partial differential equations: steady-state and time-dependent problems*, volume 98. Siam, 2007.

[65] Z. Li, J. Huang, B. Yann Liaw, V. Metzler, and J. Zhang. A review of lithium deposition in lithium-ion and lithium metal secondary batteries. *Journal of Power Sources*, 254:168–182, 2014.

[66] Y.-C. Lu, H. A. Gasteiger, M. C. Parent, V. Chiloyan, and Y. Shao-Horn. The influence of catalysts on discharge and charge voltages of rechargeable li-oxygen batteries. *Electrochemical and Solid-State Letters*, 13(6):A69–A72, 2010.

[67] Y. V. Mikhaylik, I. Kovalev, R. Schock, K. Kumaresan, J. Xu, and J. Affinito. High energy rechargeable li-s cells for ev application: status, remaining problems and solutions. *ECS Transactions*, 25(35):23–34, 2010.

[68] R. D. Mindlin. Force at a point in the interior of a semi-infinite solid. *Journal of Applied Physics*, 7(5):195–202, 1936.

[69] A. R. Mitchell and D. F. Griffiths. *The finite difference method in partial differential equations*. John Wiley, 1980.

[70] C. Monroe and J. Newman. Dendrite growth in lithium/polymer systems a propagation model for liquid electrolytes under galvanostatic conditions. *Journal of The Electrochemical Society*, 150(10):A1377–A1384, 2003.

[71] C. Monroe and J. Newman. The effect of interfacial deformation on electrodeposition kinetics. *Journal of The Electrochemical Society*, 151(6):A880–A886, 2004.

[72] C. Monroe and J. Newman. The impact of elastic deformation on deposition kinetics at lithium/polymer interfaces. *Journal of the Electrochemical Society*, 152(2):A396–A404, 2005.

[73] W. W. Mullins. Theory of thermal grooving. *Journal of Applied Physics*, 28(3):333–339, 1957.

[74] T. Mura. *Micromechanics of defects in solids*, volume 3. Springer Science and Business Media, 1987.

[75] J. Newman and K. E. Thomas-Alyea. *Electrochemical systems*. John Wiley and Sons, 2012.

[76] T. Nishida, K. Nishikawa, M. Rosso, and Y. Fukunaka. Optical observation of li dendrite growth in ionic liquid. *Electrochimica Acta*, 100:333–341, 2013.

[77] T. Ogasawara, A. Dbart, M. Holzapfel, P. Novk, and P. G. Bruce. Rechargeable li2o2 electrode for lithium batteries. *Journal of the American Chemical Society*, 128(4):1390–1393, 2006.

[78] W. C. Oliver and G. M. Pharr. An improved technique for determining hardness and elastic modulus using load and displacement sensing indentation experiments. *Journal of materials research*, 7(06):1564–1583, 1992.

[79] W. C. Oliver and G. M. Pharr. Measurement of hardness and elastic modulus by instrumented indentation: Advances in understanding and refinements to methodology. *Journal of materials research*, 19(01):3–20, 2004.

[80] M. Ortiz, E. A. Repetto, and H. Si. A continuum model of kinetic roughening and coarsening in thin films. *Journal of the Mechanics and Physics of Solids*, 47(4):697–730, 1999.

[81] E. Pan and B. Yang. Three-dimensional interfacial greens functions in anisotropic bimaterials. *Applied Mathematical Modelling*, 27(4):307–326, 2003.

[82] E. Pan and F. G. Yuan. Three-dimensional greens functions in anisotropic bimaterials. *International Journal of Solids and Structures*, 37(38):5329–5351, 2000.

[83] E. Peled. The electrochemical behavior of alkali and alkaline earth metals in non-aqueous battery systems-the solid electrolyte interphase model. *Journal of The Electrochemical Society*, 126(12):2047–2051, 1979.

[84] M. A. Pinsky. *Partial differential equations and boundary-value problems with applications*, volume 15. American Mathematical Soc., 2011.

[85] R. Pollard and J. Newman. Mathematical modeling of the lithium-aluminum, iron sulfide battery i. galvanostatic discharge behavior. *Journal of The Electrochemical Society*, 128(3):491–502, 1981.

[86] R. T. Purkayastha. Micromechanical modeling of storage particles in lithium ion batteries. 2013.

[87] R. T. Purkayastha and R. M. McMeeking. An integrated 2-d model of a lithium ion battery: the effect of material parameters and morphology on storage particle stress. *Computational Mechanics*, 50(2):209–227, 2012.

[88] M. A. Rahman, X. Wang, and C. Wen. High energy density metal-air batteries: A review. *Journal of The Electrochemical Society*, 160(10):A1759–A1771, 2013.

[89] J. Read. Characterization of the lithium/oxygen organic electrolyte battery. *Journal of the Electrochemical Society*, 149(9):A1190–A1195, 2002.

[90] J. Read, K. Mutolo, M. Ervin, W. Behl, J. Wolfenstine, A. Driedger, and D. Foster. Oxygen transport properties of organic electrolytes and performance of

lithium/oxygen battery. *Journal of The Electrochemical Society*, 150(10):A1351–A1356, 2003.

[91] J. N. Reddy. *An introduction to the finite element method*, volume 2. McGraw-Hill New York, 1993.

[92] T. J. Richardson and G. Chen. Solid solution lithium alloy cermet anodes. *Journal of Power Sources*, 174(2):810–812, 2007.

[93] D. Rosato. On the formulation and numerical implementation of dissipative electro-mechanics at large strains. 2010.

[94] K. Saito, Y. Nemoto, S. Tobishima, and J. Yamaki. Improvement in lithium cycling efficiency by using additives in lithium metal. *Journal of power sources*, 68(2):476–479, 1997.

[95] M. Singh, O. Odusanya, G. M. Wilmes, H. B. Eitouni, E. D. Gomez, A. J. Patel, V. L. Chen, M. J. Park, P. Fragouli, and H. Iatrou. Effect of molecular weight on the mechanical and electrical properties of block copolymer electrolytes. *Macromolecules*, 40(13):4578–4585, 2007.

[96] D. J. Srolovitz. On the stability of surfaces of stressed solids. *Acta Metallurgica*, 37(2):621–625, 1989.

[97] G. Strang and K. Aarikka. *Introduction to applied mathematics*, volume 16. Wellesley-Cambridge Press Wellesley, MA, 1986.

[98] J. C. Strikwerda. *Finite difference schemes and partial differential equations*. Siam, 2004.

[99] L.-G. Sundstrm and F. H. Bark. On morphological instability during electrodeposition with a stagnant binary electrolyte. *Electrochimica acta*, 40(5):599–614, 1995.

[100] D. Systmes. Abaqus users and theory manualsrelease 6.13-1. *Providence, RI, USA*, 2013.

[101] P. Thoutireddy and M. Ortiz. A variational r-adaption and shape-optimization method for finite-deformation elasticity. *Int. J. Numer. Meth. Engng*, 61:1–21, 2004.

[102] T. C. T. Ting. *Anisotropic elasticity : theory and applications*. Oxford science publications. Oxford University Press, New York, 1996. 94047372 (Thomas Chi-tsai), T.C.T. Ting. ill. ; 24 cm. Includes bibliographical references (p. [537]-562) and indexes.

[103] T. C. T. Ting and V.-G. Lee. The three-dimensional elastostatic green's function for general anisotropic linear elastic solids. *The Quarterly Journal of Mechanics and Applied Mathematics*, 50(3):407–426, 1997.

[104] F. Tonon, E. Pan, and B. Amadei. Greens functions and boundary element method formulation for 3d anisotropic media. *Computers and Structures*, 79(5):469–482, 2001.

[105] G. M. Veith, N. J. Dudney, J. Howe, and J. Nanda. Spectroscopic characterization of solid discharge products in li-air cells with aprotic carbonate electrolytes. *The Journal of Physical Chemistry C*, 115(29):14325–14333, 2011.

[106] W. C. West, J. F. Whitacre, and J. R. Lim. Chemical stability enhancement of lithium conducting solid electrolyte plates using sputtered lipon thin films. *Journal of power sources*, 126(1):134–138, 2004.

[107] M. Winter, W. K. Appel, B. Evers, T. Hodal, K.-C. Mller, I. Schneider, M. Wachtler, M. R. Wagner, G. H. Wrodnigg, and J. O. Besenhard. Studies on the an-

ode/electrolyte interface in lithium ion batteries. *Monatshefte fr Chemie/Chemical Monthly*, 132(4):473–486, 2001.

[108] W. Xu, V. V. Viswanathan, D. Wang, S. A. Towne, J. Xiao, Z. Nie, D. Hu, and J.-G. Zhang. Investigation on the charging process of li_2o_2–based air electrodes in $li - o_2$ batteries with organic carbonate electrolytes. *Journal of Power Sources*, 196(8):3894–3899, 2011.

[109] J.-i. Yamaki, S.-i. Tobishima, K. Hayashi, K. Saito, Y. Nemoto, and M. Arakawa. A consideration of the morphology of electrochemically deposited lithium in an organic electrolyte. *Journal of Power Sources*, 74(2):219–227, 1998.

[110] I. Yoshimatsu, T. Hirai, and J. Yamaki. Lithium electrode morphology during cycling in lithium cells. *Journal of the Electrochemical Society*, 135(10):2422–2427, 1988.

[111] X. H. Yu, J. B. Bates, G. E. Jellison, and F. X. Hart. A stable thin-film lithium electrolyte: Lithium phosphorus oxynitride. *Journal of the Electrochemical Society*, 144(2):524–532, 1997. Wl647 Times Cited:225 Cited References Count:26.

[112] J. Zhang, W. Xu, and W. Liu. Oxygen-selective immobilized liquid membranes for operation of lithium-air batteries in ambient air. *Journal of Power Sources*, 195(21):7438–7444, 2010.

[113] J.-G. Zhang, D. Wang, W. Xu, J. Xiao, and R. E. Williford. Ambient operation of li/air batteries. *Journal of Power Sources*, 195(13):4332–4337, 2010.